Pergamon

0967-0637(95)00034-8

*Deep-Sea Research I*, Vol. 42, No. 8, pp. 1313–1357, 1995

0967-0637/95 $9.50 + 0.00

# Coupled physical and biological modeling of the spring bloom in the North Atlantic (I): model formulation and one dimensional bloom processes

D. J. McGILLICUDDY Jr.* J. J. McCARTHY*
and A. R. ROBINSON*

(*Received* 31 *March* 1994; *in revised form* 9 *September* 1994; *accepted* 12 *January* 1995)

**Abstract**—This is the first of two papers that introduce a mesoscale eddy resolving coupled physical and biological model system. The physical model consists of a quasigeostrophic interior with a fully coupled surface boundary layer. The nitrogen based biological model includes nitrate, phytoplankton, heterotroph and ammonium fields. This interdisciplinary model system is used to examine aspects of the 1989 JGOFS North Atlantic Bloom Experiment data set. This paper deals mainly with one dimensional processes and a companion paper addresses three dimensional phenomena. The data set consists of two time series of observations taken from different water masses in the mesoscale environment. The general features of the two time series are well represented by a one dimensional model when the mesoscale *spatial* variability in the initial condition is treated explicitly within the one dimensional framework. However, a significant bias is evident in the first time series as the sampling pattern began in a warm feature and moved toward colder ones. Mistaking spatial for temporal variability in this case results in an apparent sink of heat and source of nitrate in the data. Removing this bias with the one dimensional model results in an *f*-ratio that is almost a factor of two higher (0.64) than computed by other authors based on nutrient inventories and primary productivity measurements (0.37). The second time series was conducted in the interior of a mesoscale feature and spatial biasing is minimal. The model forms a seasonal thermocline and nitracline that compare quite well with the data in both magnitude and vertical extent. A subsurface ammonium maximum is generated by the model from an initially homogeneous profile that also agrees well with the data. Simulated primary productivity profiles match $^{14}C$ incubations except on the final day of the simulation when surface nutrients appear in to have been exhausted slightly prematurely. Computed *f*-ratios are consistent with independent estimates based on uptake measurements. A systematic parameter dependence and sensitivity analysis is carried out on these results. The most sensitive parameters are the phytoplankton and heterotroph maximum growth rates. Detailed analysis of the behavior of the system indicates tight coupling between phytoplankton production and heterotrophic consumption even in the early stages of the bloom.

## 1. INTRODUCTION

This is the first of two papers in which a mesoscale eddy resolving coupled physical and biological model system is introduced and applied in the context of the 1989 JGOFS North

*Department of Earth and Planetary Sciences, Harvard University, Cambridge, MA 02138, U.S.A.; present address: Woods Hole Oceanographic Institution, Woods Hole, MA 02543, U.S.A.

Atlantic Bloom Experiment (NABE). In Part I the model system is formulated and a one dimensional implementation is used to examine aspects of the bloom that are primarily controlled by local forcing. The model then having been tuned to the NABE data in one dimension, the influence of mesoscale dynamical processes is investigated in Part II (McGillicuddy *et al.*, 1995) (hereafter MRM95).

The annual spring bloom in the Northeast Atlantic Ocean is an important event in terms of high trophic level dynamics and the carbon cycle. During the winter a combination of strong wind forcing and heat loss through the surface results in very deep mixed layers with high nutrient concentrations. Rates of primary productivity are generally low because the integrated light exposure of the phytoplankton is reduced when they are mixed over a large depth interval. When springtime stratification of the upper ocean shoals the mixed layer, integrated production exceeds losses due to respiration, sinking and grazing thereby causing a phytoplankton bloom (Riley, 1942; Sverdrup, 1953). This is a purely one dimensional process in which the relationship between the depth of mixing and the e-folding scale of the ambient light field determines the rate of primary production.

This classical one dimensional paradigm is quite useful in explaining the "early bloom" condition when phytoplankton populations are exclusively light limited. However, nutrient limitation plays an important role in the "late bloom" as surface nutrient concentrations become depleted. Under these circumstances three dimensional effects can be of primary importance. For example, the perturbation of the density field by mesoscale eddies produces significant spatial structure in the nutrient concentrations of the upper thermocline. This structure is projected to the surface by the deep mixing that sets the initial conditions for the bloom. That is, the late winter distribution of nutrients in the surface ocean contains a strong mesoscale signal. This mesoscale signal is superimposed on the large scale meridional gradient in wintertime surface nutrient concentrations that results from the north south variation in mixed layer depth (Glover and Brewer, 1988). As "early bloom" light limitation gives way to "late bloom" nutrient limitation, the spatial structure of the initial nutrient distribution results in corresponding biomass patterns. In this regard, mesoscale perturbations of the initial nutrient field allow the bloom to proceed farther in areas of enhancement, while reducing the magnitude of the biomass maximum in areas of depression.

Another fundamental three dimensional effect arises from the dynamics of mesoscale flows. The evolution of these features can cause intense vertical motions that transport nutrients toward the surface (Woods, 1988). Such transports can in fact further modify the initial nutrient distribution in the "early bloom" situation. However, their most important ramifications unfold in the later bloom stages. Mesoscale upwellings can serve to resupply phytoplankton growth in the "late bloom" period, and could represent the most important source of new nutrients in the oligotrophic "post-bloom" situation (MRM95).

Horizontal advection can also significantly influence biological and chemical distributions. Mesoscale flows can transport material over considerable distances, creating complex and convoluted structures. In contrast to the above dynamical processes which affect the *in situ* growth rate, advective processes generate variability simply by rearranging the fluid.

In addition to these three dimensional effects, there are a variety of essentially local processes that influence the evolution of the upper ocean. Surface fluxes of heat, fresh water and momentum cause variations in the mixed layer depth with corresponding entrainment and detrainment of nutrients and other important biological material.

Excursions of the mixed layer can create complicated remnant layer structures that are further modified by diffusion.

Physical, biological and chemical variability results from a combination of these effects and their interaction. Here a general interdisciplinary model system is introduced to examine these processes in detail. It is used in the context of the 1989 JGOFS NABE at 47°N, for which physical, biological and chemical data are concurrently available (see Ducklow and Harris, 1993, and references therein). The approach will be to first focus on one dimensional processes. Marra and Ho (1993) have modeled some aspects of the one dimensional bloom processes during the first of the two main observational periods during the experiment. Because a different water mass was sampled during the second observational period the two data sets cannot be reconciled in a single simulation with a one dimensional model. Here an attempt will be made to model the combined data sets with two parallel simulations using a one dimensional model in the absence of any eddy effects except for the spatially varying initial nutrient distribution.

## 2. EXPERIMENTAL DESIGN

In 1989 the JGOFS program staged a coordinated multinational effort to investigate the spring phytoplankton bloom in the North Atlantic along longitude 20°W from 15 to 60°N. One of the most intensively sampled locations was the 47°N site, which was occupied from late April to mid June with additional stations in July and August. During this time, altimetric data from Geosat and some *in situ* hydrographic measurements were used to define the mesoscale flow field in the vicinity of the experiment (Robinson *et al.*, 1993). Three cyclonic eddies ("Big," "Standard," and "Small") were observed to evolve and interact over the 10 weeks of observations (Fig. 1). Significant submesoscale variability was also documented.

Interpretation of the time series of biological observations is made difficult by the presence of mesoscale heterogeneity for a number of reasons. The issue of nutrient supply through mesoscale dynamical processes is a complex one and will be dealt with in MRM95. Here the effects of the mesoscale variability in the initial nutrient distribution will be addressed. These effects would not pose a problem to the interpretation of the time series if a single water mass were followed and sampled throughout the experiment. Unfortunately, such was not the case.

The time series of measurements can be conveniently split into two periods. Early in the time series (days 115–128) an area to the west of the Small eddy was sampled (Fig. 2a). The time series begins in the northern section of the submesoscale anticyclone to the west of the Small eddy and proceeds southward. On two occasions (days 117–118 and day 119) during this southward progression the stations are located far enough east that the frontal region between the anticyclone and the Small eddy is sampled. The ship then moved westward into a submesoscale cyclonic feature to the west of the anticyclone. After a cluster of measurements were made in this feature between days 122 and 125, the ship moved approximately 85 km eastward back to the frontal region between the anticyclone and the Small eddy. From this it can be argued that the time series is biased toward colder, more nutrient rich water masses. That is, the time series begins in the western anticyclone and then moves into colder features (the western cyclone and subsequently the Small eddy). This bias must be accounted for in interpretation of the data. Late in the time series (days 142–151) a group of stations were occupied in the interior of the Small eddy (Fig. 2b).

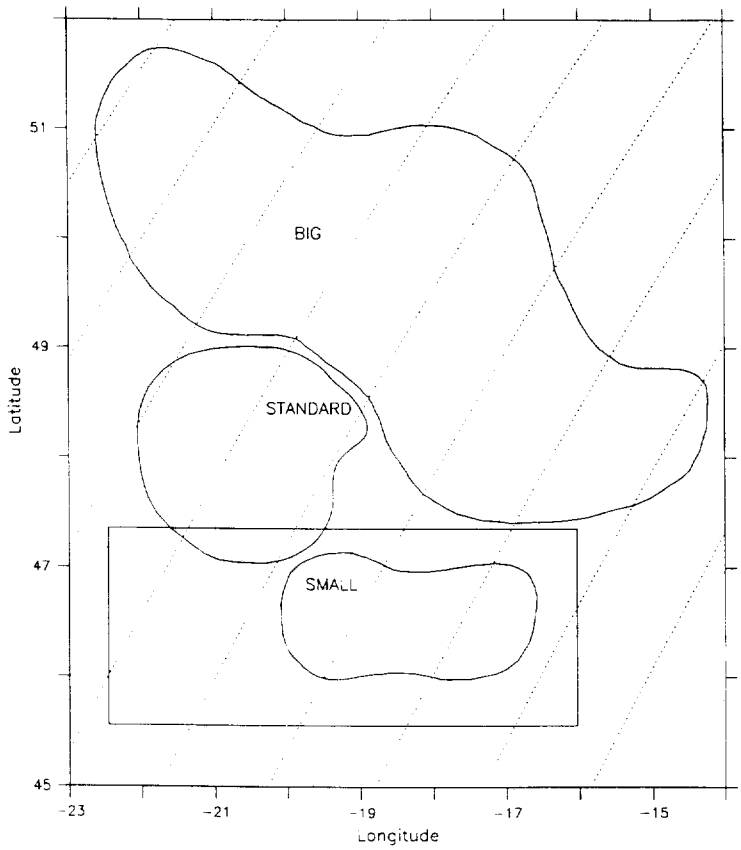


Fig. 1. Mesoscale eddy analysis for the period 8–24 May 1989 from Robinson *et al.* (1993). The three eddy features "Big", "Standard" and "Small" were identified from a combination of Geosat altimetric data (ground tracks shown as dotted lines) and hydrographic measurements. The rectangular box indicates the domain of the objective analysis shown in Fig. 2.

These observations were made in a small area of weak spatial gradients in the hydrographic field, so little bias in these measurements is expected.

These two time series (Early/Outside and Late/Inside) will be examined with a one dimensional coupled physical–biological model of the upper ocean. Because the two data sets come from different water masses, a single one dimensional simulation clearly cannot represent them both. Therefore two separate simulations ("Inside" and "Outside") are

Fig. 2. Objectively analyzed dynamic height at 25 m relative to 490 m for the first (a) and second (b) data periods in the rectangular domain shown in Fig. 1. The fields have been masked where expected error exceeds 50%. The letters indicate locations of the western flank of the Small eddy (A), the interior of the Small eddy (B), the western anticyclone (C) and the western cyclone (D). Physical and biological time series measurements are shown as open circles connected by a solid line. Locations of additional hydrographic observations are indicated by plus signs. The ship's location from year day 115 to 128 is indicated in (a). In (b) the time series spans days 142 through 151 as the ship moves first southward and then northeastward. Year days are indicated at the endpoints of the sampling period.

(a)

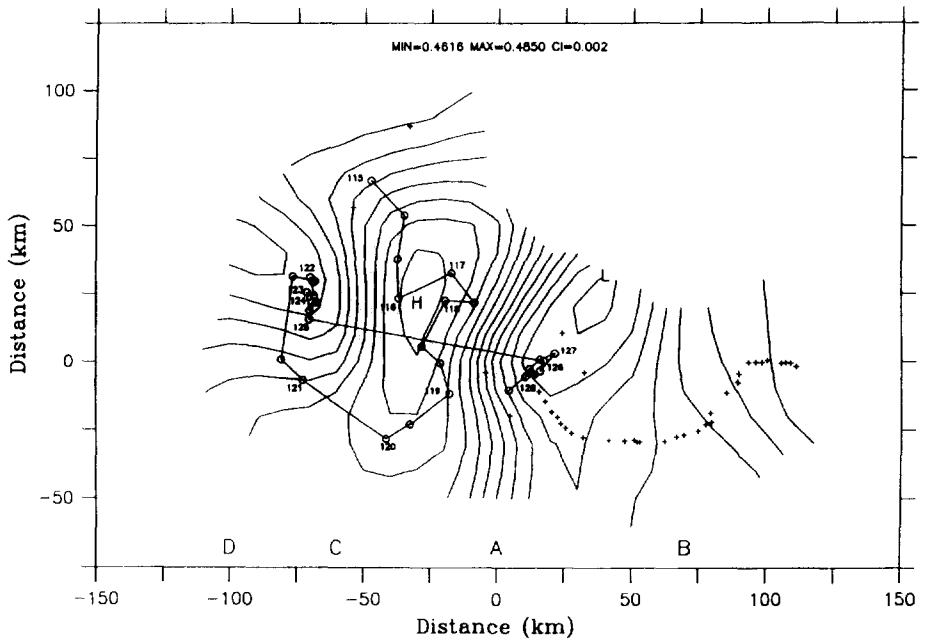


Dynamic Height at 25m: Early Period

(b)

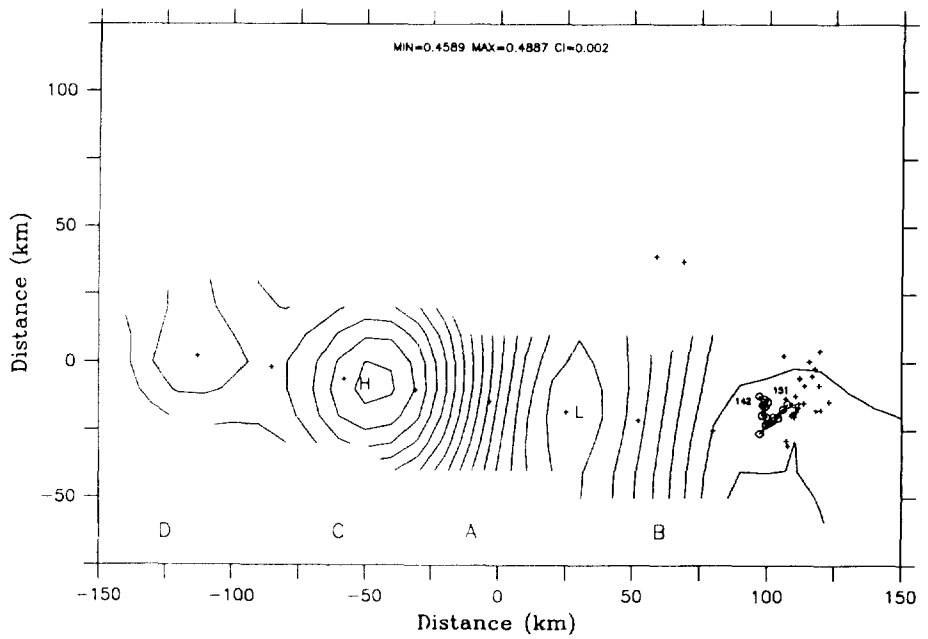


Dynamic Height at 25m: Late Period

carried out independently to reflect the different environments. Anticipating the initialization requirements of three dimensional modeling (MRM95 initialize on day 115 with full three dimensional fields), both simulations are initialized at the beginning of the experiment on day 115. It can be argued that this is not appropriate for modeling the Late/Inside data set because no data exist inside the eddy early in the experiment. However, a reasonable method for estimating the mesoscale perturbation in the pre-bloom nitrate distribution will be used to initialize the Late/Inside simulation on day 115. Concentrations of phytoplankton, heterotrophs and ammonium are assumed to be uniform and low in the late winter condition. Regardless of the initialization technique used in the Late/Inside simulation, the relevant point is that the model should run through the data where the data are available. The following simulations will show that two one dimensional simulations that differ only in their initial nitrate distribution can capture the main features of the observations.

## 3. METHODS

The various data sets used in this work were provided through the U.S. JGOFS database (Slagle and Heimerdinger, 1991). Hydrographic and nutrient data were collected by the Oceanographic Data Facility of the Scripps Institution of Oceanography. A Neil Brown CTD was used to collect conductivity and temperature profiles. A rosette of Niskin bottles was used to collect water samples for which nitrate, silicate and phosphate were measured with an autoanalyzer. High resolution nitrate and ammonium data were provided with pump profiles (Garside and Garside, 1993). Bio-optical measurements of chlorophyll fluorescence were made with a Sea Tech fluorometer by Rhea and Davis (1990). Chlorophyll *a* was estimated by fluorescent techniques calibrated by high pressure liquid chromatography (Slagle and Heimerdinger, 1991). Primary productivity was measured by the $^{14}C$ incubation technique (Knudson *et al.*, 1989; Martin *et al.*, 1993). Nitrate uptake was measured by incubations (McCarthy and Nevins, 1986). Incident PAR (400–700 nm) irradiance was provided by Broenkow *et al.* (1990). Values for the diffuse attenuation coefficient for PAR were reported by Knudson *et al.* (1989) and C. Trees. Records of wind speed and direction, air temperature and relative humidity were extracted from shipboard recording systems on both *Atlantis II* and *Meteor*.

## 4. THE MODELS

### 4.1. *The physical model*

The present study and MRM95 utilize a coupled physical and biological model. The physical model is a coupled quasigeostrophic and surface boundary layer (QG–SBL) described by Walstad and Robinson (1993) with algorithmic improvements discussed in McGillicuddy (1993). This model has been used extensively for simulation of the oceanographic environment in many regions of the ocean (Robinson, 1993) including the 1989 JGOFS Bloom Experiment (Robinson *et al.*, 1993). Although the present study deals with a one dimensional representation of this model, the full three dimensional model will be described here. In the following description, the equations for the quasigeostrophic interior are nondimensional while those for the surface boundary layer are presented in dimensional form.

The prognostic equation for the vorticity of the interior fluid is

$$\frac{\partial \zeta}{\partial t} + \alpha J(\psi,\zeta) + \beta \psi_x = F_{pqr} \tag{1}$$

where $\psi$ is the streamfunction and $\zeta$ is the dynamic vorticity given by

$$\zeta = \nabla_H^2 \psi + \Gamma^2 (\sigma \psi_z)_z \tag{2}$$

The Jacobian $J$ is defined as $J(\psi,\zeta) = \psi_x \zeta_y - \psi_y \zeta_x$, the horizontal Laplacian operator is $\nabla_H^2 = \partial^2/\partial x^2 + \partial^2/\partial y^2$ and $F_{pqr}$ represents a Shapiro filter that is used to parameterize subgridscale dissipation. The nondimensional parameters are

$$\alpha = \frac{V_0 t_0}{D} \quad \beta = \beta_0 D t_0 \quad \Gamma^2 = \frac{f_0^2 D^2}{N_0^2 H^2}$$

where the Coriolis frequency and its meridional gradient are defined as

$$f_0 = 2\Omega \sin\Theta_0 \quad \beta_0 = \frac{\partial f}{\partial y}$$

and $D$, $H$, $t_0$ and $V_0$ are characteristic length, depth, time and velocity scales. The stratification is given by

$$\sigma(z) = \frac{N_0^2}{N^2} \text{ where } N^2 = -\frac{g}{\rho}\frac{\partial \rho}{\partial z}$$

The surface and bottom boundary conditions provide prognostic equations for the top and bottom density:

$$\frac{\partial \Gamma^2 \sigma \psi_z}{\partial t} + \alpha J(\psi, \Gamma^2 \sigma \psi_z) = \begin{cases} w^1 & \text{at } z = 0 \\ -\kappa \nabla_H^2 \psi - J(\psi,b) & \text{at } z = -Z \end{cases} \tag{3}$$

where $\kappa$ is the bottom friction applied over the topography $b$. It is through the upper boundary condition that the interior and surface boundary layer models are coupled. The dimensional quasigeostrophic vertical velocity $w^{QG} = V_0 H / f_0 t_0 D \, w^1$ is balanced by the surface boundary layer vertical velocity $\omega$ to maintain the rigid lid approximation at the sea surface:

$$w^{QG} + \omega = 0 \text{ at } z = 0 \tag{4}$$

The horizontal Ekman velocities are given by

$$\mu = \frac{\partial}{\partial z}\left(\frac{\hat{j} \cdot \vec{\tau}}{\rho}\right) \quad \nu = -\frac{\partial}{\partial z}\left(\frac{\hat{i} \cdot \vec{\tau}}{\rho}\right)$$

with transports

$$\mu_T = \frac{\hat{j} \cdot \tau}{\rho_0 f_0} \quad \nu_T = -\frac{\hat{i} \cdot \tau}{\rho_0 f_0}$$

The quasigeostrophic contribution to the total vertical velocity at the surface is

$$w^{QG}(z=0) = \frac{\partial \mu_T}{\partial x} + \frac{\partial \nu_T}{\partial y} - \frac{1}{f_0}(\mu_T R_x + \nu_T R_y) - \frac{\beta_0}{f_0}\nu_T \tag{5}$$

where $R$ is the relative vorticity at the surface

$$R = \frac{V_0}{D} \nabla_H^2 \psi|_{z=0}$$

Vertical velocities are assumed to vary linearly with depth in this model. As the boundary

condition sets the surface value, the vertical derivative of the vertical velocity is used to interpolate to the interior component

$$\frac{\partial w^{QG}}{\partial z} = -\frac{V_0\Gamma^2}{f_0 t_0 D}\frac{D}{Dt}(\sigma\psi_z)_z.$$

In this model the bottom of the Ekman layer is taken to be at the base of the mixed layer so $\omega$ vanishes there. Thus $\omega$ is assumed to vary linearly between $-w^{QG}$ and 0 between $z = 0$ and $z = -h$. Equations for the boundary layer buoyancy, temperature and passive tracer evolution are

$$\rho_t + \alpha(J(\psi^*,\rho) + \mu(\delta^*_x + \rho_x) + \nu(\delta^*_y + \rho_y) + (w^{QG} + \omega)\rho_z) - \frac{\omega}{\Gamma^2\sigma} = (M_\rho)_z + \frac{\alpha_T}{c_p}I_x \tag{6}$$

$$\vartheta_t + \alpha(J(\psi^*,\vartheta) + \mu(\theta_x + \vartheta_x) + \nu(\theta_y + \vartheta_y) + (w^{QG} + \omega)\vartheta_z) - \omega\Theta_z = (M_\vartheta)_z + \frac{1}{c_p}I_z \tag{7}$$

$$\phi_t + \alpha(J(\psi^*,\phi) + \mu(\Phi_x + \phi_x) + \nu(\Phi_y + \phi_y) + (w^{QG} + \omega)\phi_z) - \omega\Phi_z + w_\phi(\phi_z + \phi_z) = (M_\phi)_z + S_\phi \tag{8}$$

with the quasigeostrophic streamfunction dimensionalized according to

$$\psi^* = V_0 D\psi.$$

The density, temperature and tracer perturbations to the mean profile due to interior motions are

$$\delta^* = \frac{\rho_0 f_0 V_0 D}{gH\sigma}(\sigma\psi_z)|_{z=0} \quad \theta = \frac{V_0 H\Gamma^2}{f_0 D}\Theta_z(\sigma\psi_z)|_{z=0} \quad \phi = \frac{V_0 H\Gamma^2}{f_0 D}\Phi_z(\sigma\psi_z)|_{z=0},$$

where $\Theta$ and $\Phi$ represent the mean temperature and tracer profiles, respectively. Passive tracers can have arbitrary sinking velocities $w_\phi$ and source terms $S_\phi$. The mixing layer depth equation is

$$h_t + uh_x + vh_y + w = e \tag{9}$$

which must be satisfied at $z = -h$ in the limit approaching from above and below. The entrainment rate $e$ is the flux across the base of the mixing layer. This quantity is derived from the turbulent kinetic energy budget in Garwood's (1977) bulk mixed layer model.

For the present purposes a one dimensional version of the model described above is used. Time dependent mesoscale effects are absent in the one dimensional case, therefore reducing the coupled quasigeostrophic and surface boundary layer physics to the surface boundary layer model with a stationary quasigeostrophic component. In the simulations that follow, the upper 150 m of the water column is discretized into 25 levels of uniform 6 m resolution in the surface boundary layer. The interior contains 12 levels that span the depth interval from the mean depth of 4300 m up to the surface where the QG and SBL grids are nested. The time step is 1.5 hours.

### 4.2. *The biological model*

A variety of models have been used to simulate the dynamics of upper ocean plankton ecosystems, ranging from the most basic nutrient–phytoplankton–zooplankton models (e.g. Steele, 1974) to much more complex formulations that include dissolved organic material, detritus, bacteria and multiple size classes of organisms (e.g. Fasham *et al.*,

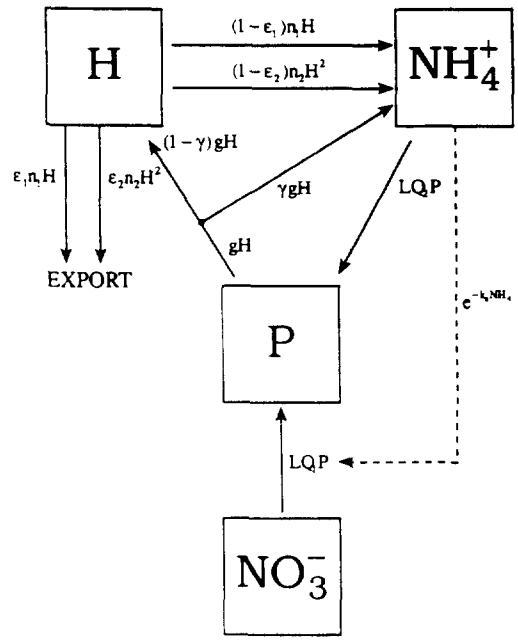


$$L = P_{max}\left(1 - e^{\frac{-\alpha I}{P_{max}}}\right)e^{\frac{-\beta I}{P_{max}}}$$

$$Q = Q_1 + Q_2 = \frac{NO_3 e^{-\psi_e NH_4}}{k_1 + NO_3} + \frac{NH_4}{k_2 + NH_4}$$

$$g = R_m(1 - e^{\lambda P})$$

Fig. 3. A schematic diagram of the biological model used in this study.

1990). The approach used here is to keep the model as simple as possible yet to retain enough structure that the basic functioning of the ecosystem is well represented in a framework that is capable of exposing the processes of interest—namely the effects of mesoscale and upper ocean dynamics on biological productivity. A nitrogen based nutrient–phytoplankton–heterotroph model is introduced that is intermediate in complexity with respect to the two models cited above. For the purposes of investigating how physical transports supply nutrients to the euphotic zone it is particularly useful to treat new and regenerated forms of nitrogen separately. This facilitates explicit distinction between primary production that results from the injection of nitrate from below and that which is sustained on recycled ammonium.

A schematic diagram of the biological model is shown in Fig. 3. The model equations for phytoplankton ($P$), heterotrophs ($H$), nitrate ($NO_3^-$), ammonium ($NH_4^+$) and exported nitrogen ($N_E$) are

*Table 1. Biological model parameters and definitions*

| Parameter | Description |
|---|---|
| $k_w$ | light attenuation due to water |
| $k_c$ | phytoplankton self shading parameter |
| $p_{max}$ | maximum photosynthetic rate |
| $p_1$ | initial slope of photosynthesis response to light |
| $p_2$ | photoinhibition parameter |
| $k_1$ | half saturation constant for nitrate uptake |
| $k_2$ | half saturation constant for ammonium uptake |
| $k_n$ | strength of ammonium inhibition of nitrate uptake |
| $R_m$ | maximum grazing rate |
| $\Lambda$ | Ivlev constant |
| $\gamma$ | grazing efficiency |
| $n_1$ | linear heterotrophic loss rate |
| $n_2$ | quadratic heterotrophic loss rate |
| $\varepsilon_1$ | exported fraction of linear heterotrophic loss rate |
| $\varepsilon_2$ | exported fraction of quadratic heterotrophic loss rate |
| $w_{sink}$ | phytoplankton sinking rate |
| $f_w$ | f-ratio dependence of phytoplankton sinking rate |

$$\frac{\partial P}{\partial t} = LQP - gH \tag{10}$$

$$\frac{\partial H}{\partial t} = (1 - \gamma)gH - n_1H - n_2H^2 \tag{11}$$

$$\frac{\partial \mathrm{NO_3}}{\partial t} = -LQ_1P \tag{12}$$

$$\frac{\partial \mathrm{NH_4}}{\partial t} = -LQ_2P + \gamma gH + (1 - \varepsilon_1)n_1H + (1 - \varepsilon_2)n_2H^2 \tag{13}$$

$$\frac{\mathrm{dN_E}}{\mathrm{d}t} = \varepsilon_1 n_1 H + \varepsilon_2 n_2 H^2 \tag{14}$$

The model parameters are listed in Table 1. The first four equations describe the local tendencies of the various nitrogen constituents that result from biological processes. Because these species of nitrogen are to be incorporated as passive tracers in a four dimensional physical model of the ocean, these partial derivatives represent only part of the overall local tendency which is affected by physical processes as well. The local tendencies are used as forcing functions $S_\phi$ in the tracer evolution equations of the coupled quasigeostrophic and surface boundary layer model. The complex nonlinearity of the biological equations requires that they be solved numerically. A fourth order Runge–Kutta technique with adaptive stepsize control (Press *et al.*, 1986) is used in the present work to solve equations (10–13). The transport of exported nitrogen by ocean currents is not treated. This material is assumed to sink instantaneously to the deep ocean and is accumulated in a two dimensional $(x,y)$ model sediment trap whose time evolution is given by equation (14).

Phytoplankton growth is both light and nutrient limited. The photosynthetic response to irradiance is

$$L = P_{max}\,(1 - e^{-p_1 I/P_{max}})\,e^{-p_2 I/P_{max}}$$

following the formulation of Platt *et al.* (1980). The light field is affected by phytoplankton pigments through self shading. Their effect on the inherent optical properties of the water column is given by

$$I(x,y,z,t) = I_0(t)e^{k_w z + k_c \int_0^z P(x,y,z,t)\mathrm{d}z}$$

The maximum specific rate of growth $L$ for a given light intensity is modulated by a nutrient limitation factor $Q$ similar to the one used by Fasham *et al.* (1990):

$$\begin{aligned} Q &= Q_1 + Q_2 \\ &= \frac{NO_3\, e^{-k_w NH_4}}{k_1 + NO_3} + \frac{NH_4}{k_2 + NH_4} \end{aligned}$$

It is composed by both nitrate and ammonium components which are cast in the familiar Michaelis–Menten form commonly used to represent nutrient uptake. This formulation first proposed by Wroblewski (1977) allows for the commonly observed ammonium inhibition of nitrate uptake that results from the phytoplankton preference for the reduced form of nitrogen. The total phytoplankton sinking rate $w_P$ is the sum of a constant rate and a term that depends linearly on the $f$-ratio

$$w_P = w_{sink} + f \cdot f_w$$

where the $f$ ratio is defined as

$$f = \frac{Q_1}{Q_1 + Q_2}$$

The $f$-ratio dependence can in some cases be used to parameterize the effect of a shift in species composition. For example, early in a spring bloom a phytoplankton assemblage dominated by large diatoms that sink rapidly once the nutrients are depleted would give rise to a high $f$-ratio. Later in the bloom, when the large diatoms have been replaced by smaller flagellated species that sink much more slowly, the $f$-ratio would decline. Numerical experiments will show that this process is not crucial to the evolution of the biological and chemical properties of the water column in these bloom simulations. However this effect will be retained in the model for consistency in the presentation of results. Note that the sinking rate does not appear in the biological equations because it is a transport that is dealt with in the physical model (equation 8).

Heterotrophic consumption of phytoplankton biomass is represented by Ivley's (1955) grazing function:

$$g = R_m(1 - e^{-\lambda P})$$

which has been studied and used extensively in modeling applications (Parsons *et al.*, 1984; Mullin *et al.*, 1975; Steele and Mullin, 1977). The parameter $\gamma$ determines the efficiency with which the grazed material is assimilated into heterotrophic biomass. The heterotrophic loss rate has both linear and quadratic terms. The quadratic form first suggested by Steele and Henderson (1981) is an effective way to parameterize the predation of herbivores by carnivores. Loss via this mechanism is quite small at low herbivore concentrations but dominates heterotrophic loss at higher abundance. This behavior

proves to be critical in maintaining stability in the balance between phytoplankton and heterotrophs in cases when the rate of grazing approaches the rate of phytoplankton growth. Heterotrophic losses are partitioned into recycled and exported components by the two parameters $\varepsilon_1$ and $\varepsilon_2$.

Detritus is not treated explicitly in this model. Regeneration of the nitrogen content of this material is assumed to occur instantaneously. Alternatively, this assumption can be interpreted that the detrital nitrogen pool is in steady state, so inputs and outputs balance each other. Care must be taken in applying this model to situations where significant changes in detrital nitrogen occur. For example, while ignoring detrital accumulation early in a spring bloom simulation is probably justifiable, it may be less appropriate in the late-bloom and post-bloom context. However, for the present purposes of investigating the basic processes of physical–biological interactions, this is not likely to be a critical omission. Furthermore, because the relevant fluxes into and out of the detrital reservoir are not well known nor quantified by experimental measurements, the interpretive power gained by additional complexity is of questionable value in this case.

## 5. MODEL INITIALIZATION

The model is initialized with profiles of buoyancy and temperature that are homogeneous in the mixed layer and linearly stratified below. There is no discontinuity at the base of the mixed layer. These profiles are fitted to the available data as described below. The nitrate profile is defined through a linear relationship with $\sigma_T$. Distributions of phytoplankton, heterotrophs and ammonium are assumed to be homogeneous and low in the initial condition (0.5, 0.04 and 0.02 $\mu M$ nitrogen units, respectively).

Care must be taken to ensure that a single linear nitrate–$\sigma_T$ relationship is appropriate. Figure 4 shows the ensemble of all upper ocean nitrate measurements plotted as a function of $\sigma_T$. This distribution of points appears to represent two linear portions that intersect at $\sigma_T = 27.0$. This intersection lies at the surface $\sigma_T$ value measured at the beginning of the experiment. Hence the change in slope for $\sigma_T < 27.0$ is representative of a perturbation to the mean linear profile by heating and phytoplankton uptake near the surface. Because the nitrate–$\sigma_T$ relationship is roughly linear for $\sigma_T > 27.0$ over the range of observed water masses, it is assumed that this single linear relationship is appropriate for initialization purposes. This relationship yields a surface nitrate concentration of 5.8 $\mu M$ outside the eddy on day 115, which is consistent with the data. It predicts a surface nitrate concentration of 8.4 $\mu M$ inside the eddy on day 115, where no data are available.

The top row of Fig. 5 shows the initial model buoyancy, temperature and nitrate profiles and data from the first three days of observations outside the Small eddy (days 115–117). These data are chosen to be representative of the background state with no eddy perturbation. It can be argued that these observations do not necessarily reflect the true background state because the observations lie in the submesoscale anticyclone (Fig. 2a). However, the strength of this feature is known to be weak relative to the magnitude of the Small eddy perturbation. Therefore, this ensemble of measurements can be reasonably expected to reflect the background state.

Data are available inside the Small eddy only for the latter part of the experiment, so initial upper ocean profiles must be inferred for this region. Here mesoscale perturbations are represented by vertical displacements of the mean stratification, which is linear. If the mixed layer depth is assumed to be spatially uniform on the mesoscale, then eddy

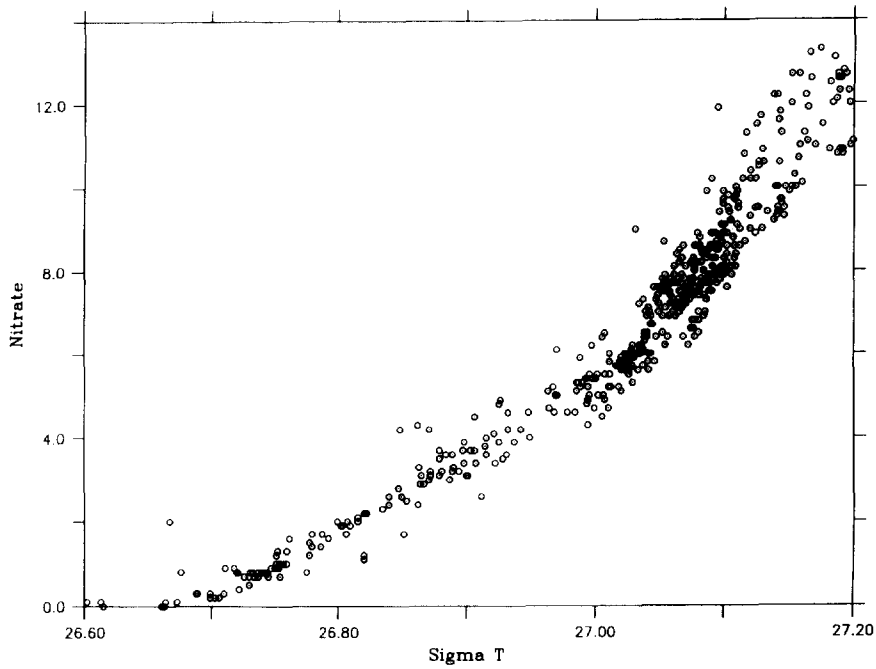


Fig. 4. Upper ocean nitrate concentrations ($\mu M$) plotted as a function of $\sigma_t$.

perturbations simply shift profiles along the abscissa. A number of authors have shown that mesoscale eddies can induce spatial variability in the depth of the mixed layer (Klein and Hua, 1988; Stevenson, 1983; Walstad and Robinson, 1993). However, the root mean square variation is generally less than 10%, so mesoscale variability in the initial mixed layer depth will not be included in this analysis.

The initial conditions used inside the Small eddy are shown in Fig. 5 (bottom row). Exactly the same initialization parameters have been used. The only difference is that the profiles have been shifted by an amount consistent with the perturbation of the Small eddy. The vertical gradient below the mixed layer appears to be less than in the top row because the profiles are plotted on different scales. The data were collected much later in the experiment (days 142–151) so it is expected that the model initial condition should be quite different from these observations near the surface where significant heating and nutrient uptake have occurred. However, it is important to note that the profiles do agree at depth, where modification due to surface processes are negligible. This suggests that the initial condition is in fact satisfactorily tuned to the data.

## 6. ESTIMATION OF THE BIOLOGICAL MODEL PARAMETERS

### 6.1. *The light environment*

The equation for the total light extinction coefficient for photosynthetically active radiation $k_{par}$ is

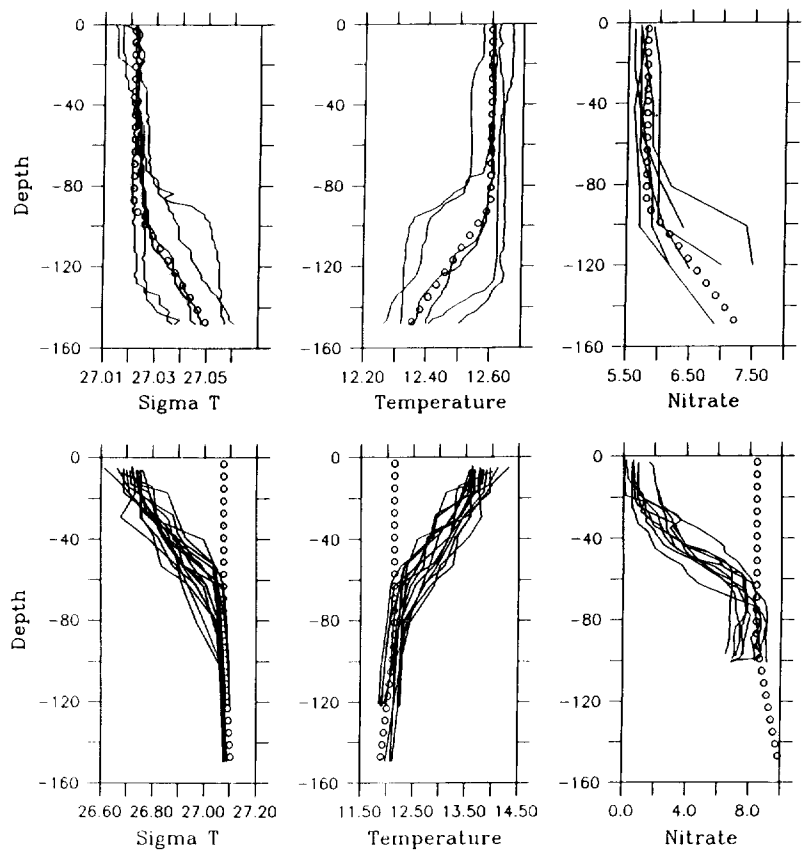


Fig. 5. Initial profiles of $\sigma_t$, temperature and nitrate for outside the Small eddy (top row) and inside the Small eddy (bottom row). Values used to initialize the model are indicated as open circles. Data collected on days 115–117 outside the Small eddy are shown as solid lines in the top row. Data collected on days 142–151 inside the Small eddy are shown as solid lines in the bottom row. Note that the abscissa scales of the top row are much narrower than those of the bottom row.

$$k_{par} = k_w + k_c P$$

where $k_w$ is the coefficient for pure seawater and $k_c$ is a phytoplankton self shading parameter. Observed changes in phytoplankton abundance and the light field from days 115–128 were used to estimate the light environment parameters. Bio-optical measurements indicate phytoplankton biomass approximately tripled over this time period. In nitrogen units, this corresponds to $P$ varying from its initial value 0.5–1.5. Meanwhile, the average $k_{par}$ increased from 0.07 to 0.11. The best estimates for $k_w$ and $k_c$ are thus the solutions to the matrix equation

$$\begin{bmatrix} 1.0 & 0.5 \\ 1.0 & 1.5 \end{bmatrix} \begin{bmatrix} k_w \\ k_c \end{bmatrix} = \begin{bmatrix} 0.07 \\ 0.11 \end{bmatrix}$$

which is simply

$$\begin{bmatrix} k_w \\ k_c \end{bmatrix} = \begin{bmatrix} 0.05 \\ 0.04 \end{bmatrix}$$

This value of $k_w$ is slightly higher than the estimate of 0.04 made by Lorenzen (1972) and used by Fasham *et al.* (1990). The value of $k_c$ is also slightly higher than some published values (Fasham *et al.*, 1983; Kirk, 1983) and that used by Fasham *et al.* (1990), but well within reasonable bounds due to the uncertainty in phytoplankton nitrogen biomass determination. Although these coefficients are somewhat different from what has been used by previous authors, they do yield a simulated underwater light field that is consistent with observations (see Figs 16b, 24b and discussion below).

### 6.2. *Phytoplankton parameters*

The most important aspect of the phytoplankton growth rate expression is the photosynthesis versus irradiance relationship. The primary production measurements are useful in determining two of the three relevant parameters of this function. The $^{14}C$ incubations are a measure of the total carbon uptake over the dawn to dusk incubation period. The total amount of carbon assimilation depends not only on the photosynthesis versus irradiance function, but also the phytoplankton biomass inside the experimental container. Because the actual phytoplankton biomass inside the container is not known with sufficient certainty, it is impossible to determine specific rates of photosynthesis accurately. However, normalizing each primary production profile to its maximum value allows the estimation of the light dependent photosynthesis parameters $p_1$ and $p_2$. Figure 6 shows the normalized profiles and the chosen model fit to the data. Care must be taken in the interpretation of the normalized profiles because on those days in which there was not enough light to saturate the photosynthetic apparatus of the upper samples, the profiles will be normalized to something less than $P_{max}$ and therefore the initial slope will be overestimated. Therefore the model representation was subjectively chosen to fit those profiles which show distinguishable saturation at higher light intensities. Although two data points indicate some photoinhibition, this is not thought to be a critical process in the context of the present study and $p_2$ was set to zero.

Because no measurements of the maximum specific growth rate are available for this data set, this parameter was set to a value that produced nutrient removal, phytoplankton biomass and primary productivity that are consistent with the data. The chosen value (0.66 $day^{-1}$) falls within the range of estimates derived from field and laboratory measurements (Parsons *et al.*, 1984) although it may be slightly low for a bloom situation.

There are relatively few published half saturation values for ammonium and nitrate uptake characteristic of natural assemblages of oceanic versus coastal or estuarine phytoplankton (see review by Goldman and Glibert, 1983). For ammonium these range from undetectable to 0.6 $\mu M$ and from 1.1 to 1.3 $\mu M$ in low and high nutrient oceanic regions, respectively. For nitrate they range from undetectable to 0.9 $\mu M$ and from 1 to 4.2 $\mu M$ in low and high nutrient oceanic regions, respectively. The assessment of half saturation constants for nutrient uptake during this experiment was particularly difficult because nitrate and ammonium uptake rates were saturated at the ambient concentrations observed throughout most of the period of observation. Approximations of ammonium half saturation constants were very low (less than 0.02 $\mu M$) with large uncertainties because of the common condition of near saturating levels of substrate. Due to these

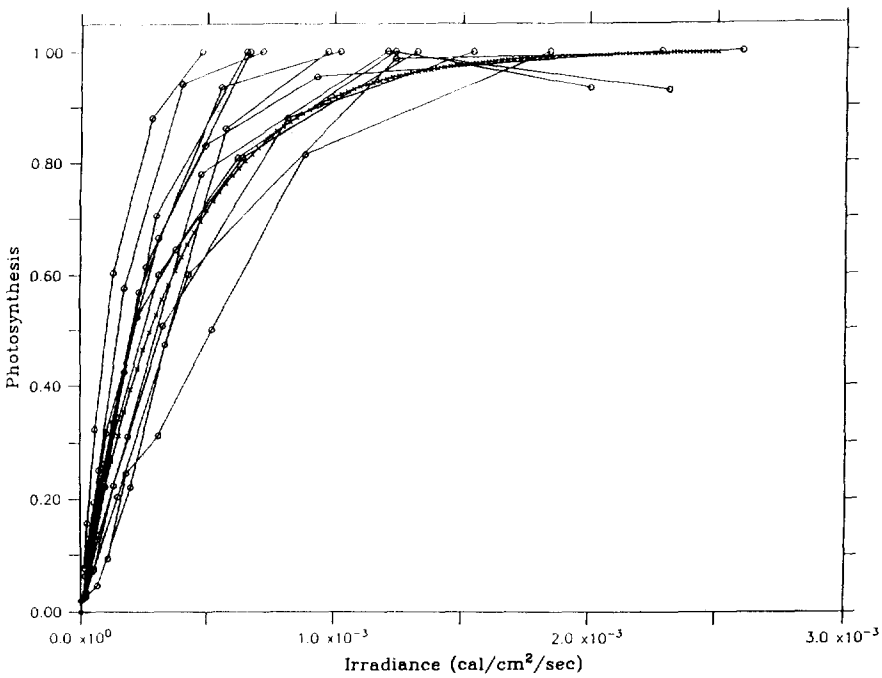


Fig. 6. The model representation of the light dependence of the photosynthesis versus irradiance data (see text). Normalized photosynthesis versus irradiance curves from the Leg 2 primary production measurements are shown as open circles connected with solid lines. The cross-hatched line is the model curve.

considerations and in the absence of other data from this specific study region, we believe that relatively low half saturation constants, 0.05 and 0.2 $\mu M$ for ammonium and nitrate uptake, respectively, are justified for modeling purposes.

While many laboratory, coastal and estuarine, as well as some oceanic data sets indicate nearly complete suppression of phytoplankton nitrate uptake when ammonium concentrations exceed about 1 $\mu M$ (see, for example, Syrett, 1981; McCarthy, 1981), the experiments conducted during this study indicate much greater sensitivity of nitrate uptake to ammonium presence. Another region that has revealed a similar pattern is the subarctic Pacific (Wheeler and Kokkinas, 1990). These investigators found that concentrations as low as 0.1 $\mu M$ could completely suppress nitrate uptake. Similar results in the present study are shown in Fig. 7, where very little nitrate uptake occurs for concentrations of ammonium in excess of 0.1 $\mu M$ even though nitrate availability is in excess of saturating concentrations. Based upon these data an e-folding concentration of ammonium for nitrate uptake was set at 0.1 $\mu M$ in the model.

There are no measurements of the phytoplankton sinking rate available for this experiment. Values for $w_{sink}$ and $f_u$ were chosen that produced phytoplankton biomass distributions that are consistent with the data. As discussed in the model formulation, the dependence of the sinking rate on the *f*-ratio is an attempt to parameterize the effect of changing species composition. Early in the bloom when the *f*-ratio is high, sinking rates can approach 5.5 m/day, which is a conservative yet reasonable rate for fast sinking diatoms

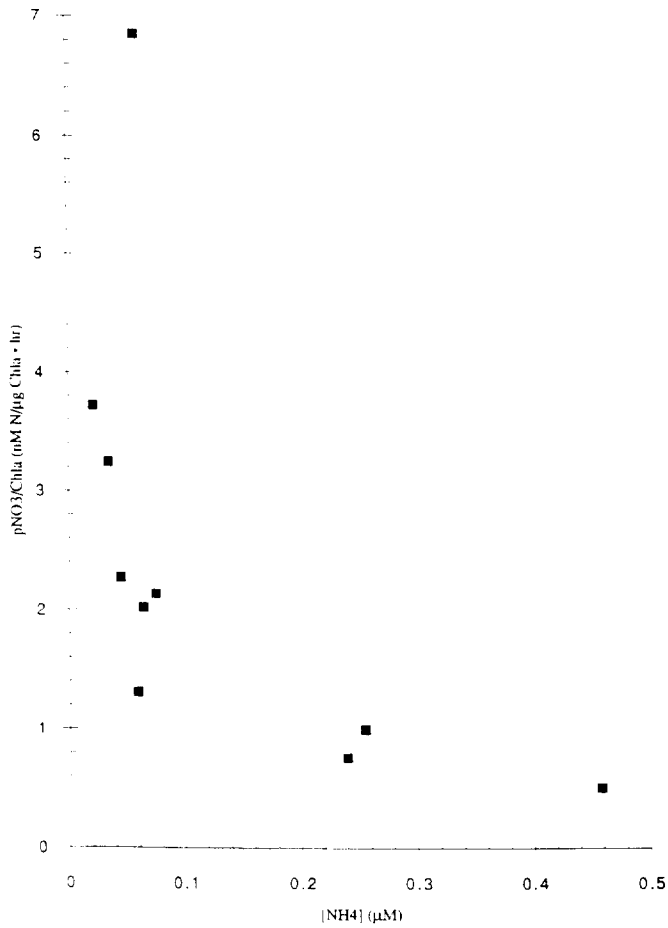


Fig. 7. Nitrate uptake plotted as a function of ammonium concentration. Nitrate uptake values have been normalized to the chlorophyll *a* of the sample. The data show strong ammonium inhibition of nitrate uptake for concentrations greater than 0.1 $\mu M$.

known to predominate during that time. Sinking rates up to 100 m/day have been reported in the literature (Alldredge and Gotschalk, 1989). As the *f*-ratio falls later in the bloom, sinking rates can decrease to as little as 0.5 m/day which is more characteristic of sinking rates reported for non-bloom situations (Bienfang, 1981).

### 6.3. *Heterotroph parameters*

Recent evidence suggests that microzooplankton are the dominant grazers of phytoplankton populations in open ocean environments (e.g. Capriulo, 1990). In fact, observations during the NABE indicate that mesozooplankton exerted only slight grazing pressure on phytoplankton, consuming only a few percent of the total primary production (Dam *et al.*, 1993). Heterotrophic parameters were therefore chosen to represent herbivorous microzooplankton, with a maximum growth rate approaching that of phytoplankton. Unfortunately no direct grazing measurements are available for this ensemble

*Table 2. Biological model parameter values*

| Parameter | Units | Value |
|---|---|---|
| $k_w$ | $m^{-1}$ | 0.05 |
| $k_c$ | $m^{-1} \mu M^{-1}$ | 0.04 |
| $p_{max}$ | $day^{-1}$ | 0.66 |
| $p_1$ | $(cal^{-1} cm^2)^{-1}$ | 0.0019 |
| $p_2$ | $(cal^{-1} cm^2)^{-1}$ | 0.0 |
| $k_1$ | $\mu M$ | 0.2 |
| $k_2$ | $\mu M$ | 0.05 |
| $k_n$ | $\mu M$ | 27.2 |
| $R_m$ | $day^{-1}$ | 0.69 |
| $\Lambda$ | $(\mu M)^{-1}$ | 1.0 |
| $\gamma$ | nondimensional | 0.25 |
| $n_1$ | $day^{-1}$ | 0.11 |
| $n_2$ | $day^{-1}$ | 0.52 |
| $\varepsilon_1$ | nondimensional | 0.75 |
| $\varepsilon_2$ | nondimensional | 0.50 |
| $w_{sink}$ | $m\ day^{-1}$ | 0.5 |
| $f_w$ | $m\ day^{-1}$ | 5.0 |

of organisms during the experiment, so values of $R_m$, $\Lambda$ and $\gamma$ were chosen to be consistent with the range of previously reported values. Little is known about the loss rates of these organisms and how the loss is partitioned into recycled and exported material. Thus $n_1$, $n_2$, $\varepsilon_1$ and $\varepsilon_2$ were tuned to maximize agreement between the model and available data.

### 6.4. *Summary*

Of the 17 biological model parameters, only four ($k_c$, $p_1$, $p_2$ and $k_n$) are well constrained by measurements during the NABE and three ($k_w$, $k_1$ and $k_2$) by values reported in the literature. The literature provides some guidance for the remaining 10 parameters, but not all. With these caveats in mind, the unknown model parameters were tuned within reasonable ranges in order to best represent the data. Several hundred runs were carried out and the best fit to the data was chosen subjectively. The "best fit" parameter values used in the simulations that follow are listed in Table 2.

## 7. ONE DIMENSIONAL SIMULATIONS

In the following one dimensional simulations the physical model is forced by surface fluxes of heat and momentum estimated from shipboard meteorological observations and standard bulk formulae (Gill, 1982). Figure 8 shows the records of wind and insolation and the computed surface heat flux (comprising sensible, latent and longwave radiative fluxes). A comparison of the model simulated mixed layer depth with observations is shown in Fig. 9. A variety of criteria have been proposed for the determination of the mixed layer depth. In this case it has been subjectively chosen as the shallowest depth where significant stratification exists. The model captures the general features of the mixed

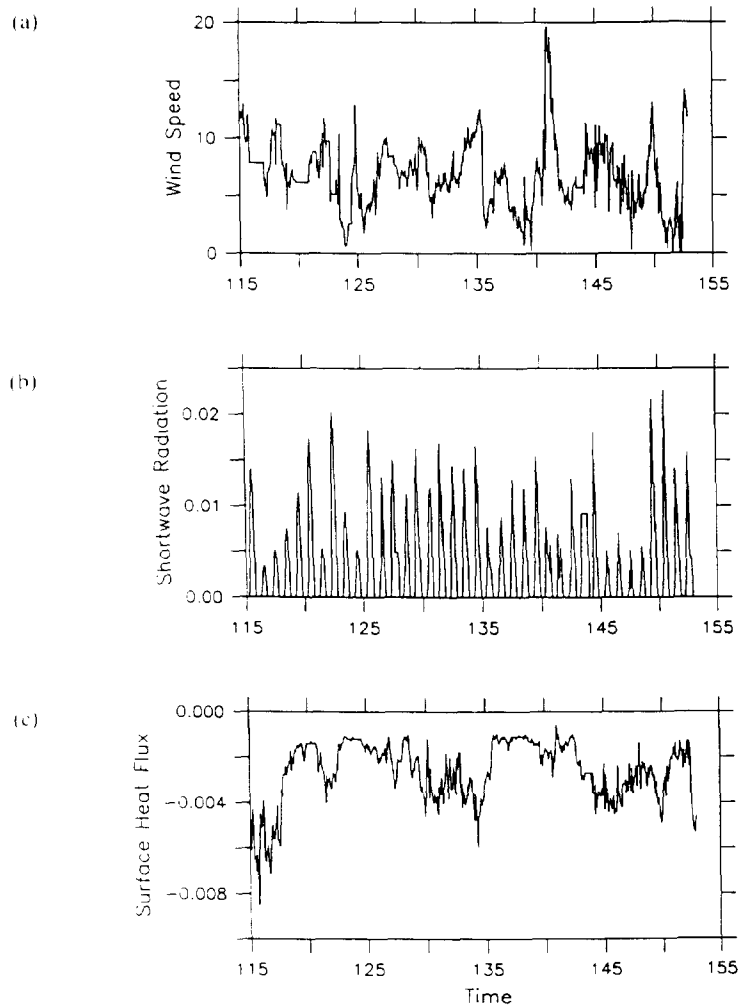


Fig. 8. Time series of quantities used to force the physical model: (a) wind speed (m $s^{-1}$), (b) shortwave radiation (cal $cm^{-2}$) and (c) surface heat flux (cal $cm^{-2}$).

layer depth time series, including the shoaling that occurs during the onset of stratification, high frequency (hours to days) fluctuations and the storm event on day 142. Clearly these features are not perfectly represented by the model. The initial stratification is more intermittent in the model than the data suggest. In general the model seems to convect to a greater depth at night than is indicated by the data. The mixed layer does not deepen enough during the storm. However, the model employed here is a simple bulk model that cannot represent all of the complex structure observed in the ocean. It does, however, capture the general features of the mixed layer and seasonal thermocline system (see below) relevant to the biological processes of interest. Sensitivity analyses indicate that the biological simulations are reasonably robust with respect to the detailed behavior of the mixed layer.

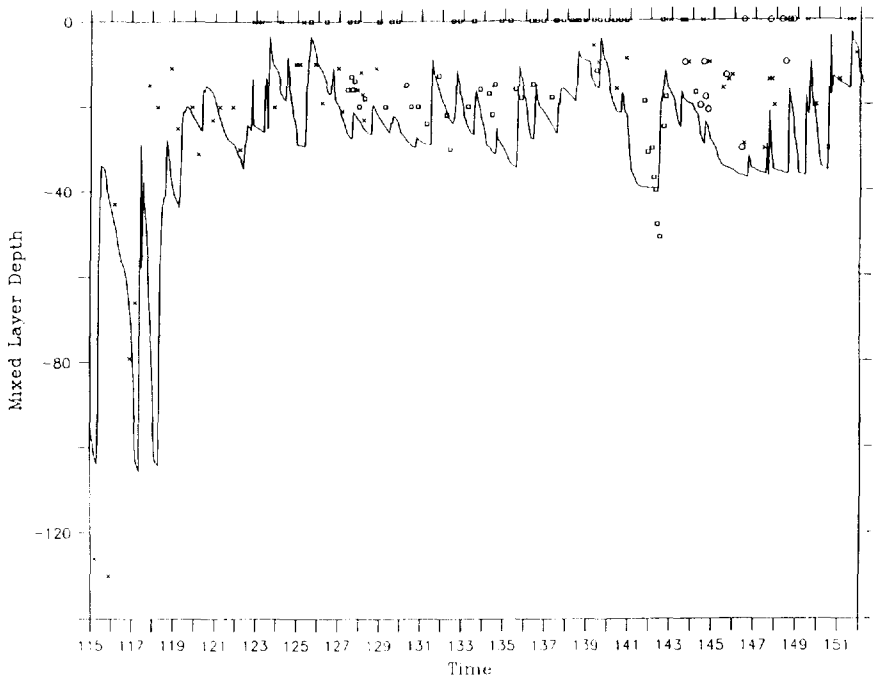


Fig. 9. Observations of mixed layer depth from CTD casts (crosses: *Atlantic II*; squares: *Meteor*; circles: *Discovery*) and simulated mixed layer depth (solid line). The mixed layer depth is reported to be zero when no clearly definable homogeneous layer exists in the temperature and salinity profiles.

### 7.1. *Early/Outside*

Time series of simulated and observed temperature profiles are shown in Fig. 10. The data reveal a water column initially well mixed to a depth of 100 m which quickly stratifies as heat is pumped into the near surface region. Surface temperatures rise from 12.4°C to approximately 13.0°C. However, there are significant temperature fluctuations below the upper 50 m or so that is directly forced by the surface heat flux. The fairly dramatic lifting of temperature surfaces toward the end of the observations suggests the presence of mesoscale and/or submesoscale variability. Analysis of the cruise track in relation to the mesoscale and submesoscale environment (Fig. 2c) suggests that the ship did in fact traverse physically distinct features. Observations for this leg commenced on day 115 in a submesoscale warm feature to the west of the Small eddy. Days 117–120 were spent in the frontal region between the warm feature and the western flank of the small eddy. The ship then moved to the cold feature to the west of the submesoscale anticyclone during days 121–125. Finally, days 126 through 128 were spent in the frontal region between the anticyclone and the Small eddy. In fact, these measurements were collected further to the east than the previous stations in the frontal region. Their proximity to the interior of the Small eddy accounts for the apparent cooling at depth shown in the data.

Figure 10a shows the model evolution of the temperature profile. Of course the mesoscale and submesoscale variability are not represented in the one dimensional model. However, the general features of the temperature evolution shown in the data are

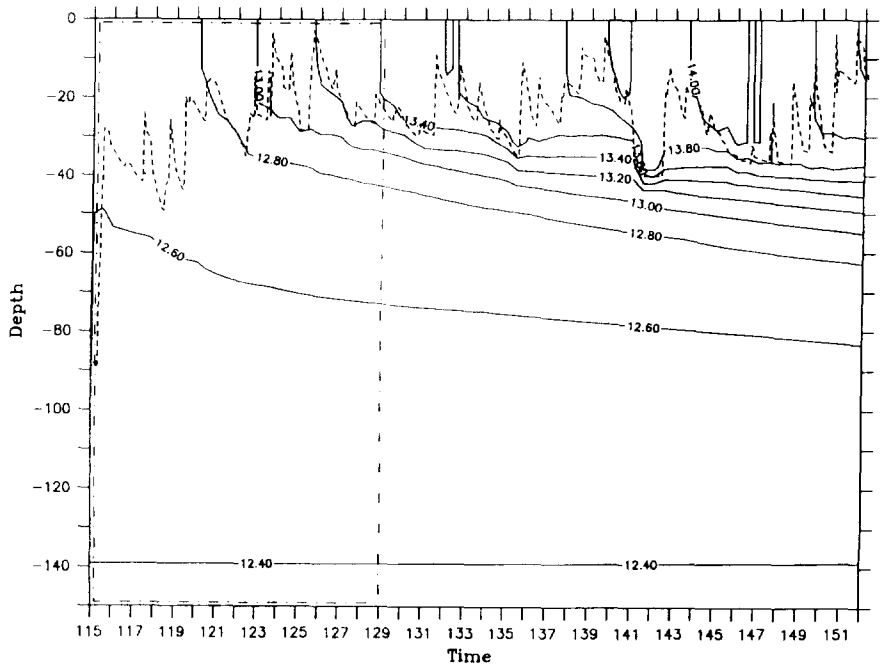


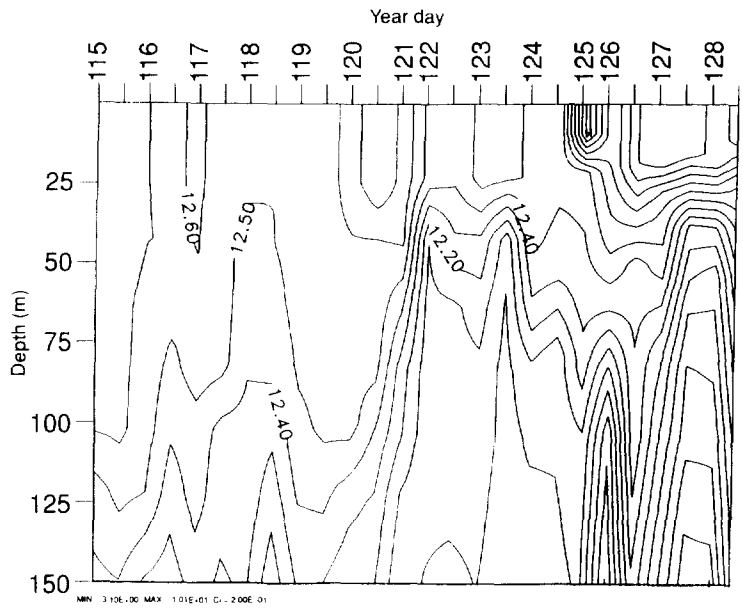


Fig. 10. (a) The evolution of the temperature profile for the Early/Outside simulation. The dashed line indicates the location of the mixed layer depth during time series. The dashed–dotted line denotes the extent of the data shown in (b). In (b) the spacing between days appears to vary because the contouring algorithm spaces the casts regularly and some days have multiple casts while others do not.

captured. The surface temperature rises to approximately 13.4°C, slightly higher than is observed. But, the fact that the ship moved toward a cold feature at the end of the observational period could account for this difference. By day 128 a seasonal thermocline has begun to form between 20 and 40 m, which is roughly consistent with the data.

Figure 11a shows the evolution of the model nitrate profile. Nitrate is removed from the surface layer more quickly than in the data (Fig. 11b). Surface values on day 128 are 2.2 $\mu M$ and 3.2 $\mu M$, respectively. This discrepancy is attributable to mesoscale variability according to the following argument. The difference in initial surface nitrate concentration between inside versus outside the Small eddy was estimated to be 3 $\mu M$ (Fig. 5). A bias in the observations toward sampling colder more nutrient rich features at the end of the time series could therefore account for the difference; moving from a warm feature into a colder one causes an apparent supply of nitrate. Given the fact that the difference is only one third of the expected variation between the exterior of the eddy and its inner core, this is certainly plausible. It is also possible that errors in the model nitrate uptake rate could account for some of the discrepancy near the surface. However, the observed increase in nitrate below the euphotic zone (Fig. 11b) is highly suggestive of mesoscale variability. MRM95 show that the discrepancy can be reconciled with a three dimensional model. By sampling the four dimensional model nitrate field in space and time along the cruise track, the model can be brought into near perfect agreement with the data.

Figure 12a shows the evolution of the model phytoplankton nitrogen profile. Phytoplankton begin to accumulate in the near surface region soon after the mixed layer shoals. The rate of accumulation appears to be somewhat higher than that indicated by bio-optical measurements of chlorophyll (Fig. 12b) assuming a chlorophyll to nitrogen ratio of 1 g Chl*a*:1 mol $NO_3$ (Marra and Ho, 1993). By day 128, the model surface value is approximately 2.5 $\mu M$, which is not statistically different from the observations given the potential variation in the chlorophyll to nitrogen ratio. It is possible that temporal changes in the chlorophyll to phytoplankton nitrogen ratio may be partially responsible for the apparent difference in biomass accumulation. However, no discernible trend is evident in this ratio when computed from the bulk particulate nitrogen data (not shown). Variations in the chlorophyll to phytoplankton nitrogen ratio with depth due to photoadaptation might account for some of the vertical structure in the data that are not captured by the model. But, again it is not possible to identify a trend from the samples of bulk particulate nitrogen.

A comparison of simulated primary productivity profiles with data from *in situ* $^{14}C$ incubations is shown in Fig. 13. A constant carbon to nitrogen ratio of 6.7 has been used to make this comparison. Early in the time series there is a systematic underestimation of primary production by the model in the near surface region. However, later in the time series (days 123–128) agreement is much better. We have been unable to formulate a satisfactory explanation for why the model is overpredicting phytoplankton biomass and underpredicting productivity early in the simulation. It is possible that the phytoplankton carbon to nitrogen ratio might have changed during this time period. Analysis of the time series of this ratio in particulate organic matter reveals a great deal of variability but no statistically significant trend (not shown). Alternatively, it may be that changes in species composition caused a shift in the photosynthetic rate parameters. The data do not indicate a consistent trend in either $p_1$ or $p_2$ but changes in $p_{max}$ cannot be ruled out.

The evolution of the model heterotrophic population is shown in Fig. 14. Unfortunately there are no microzooplankton measurements with which to compare this time series. The

(a)

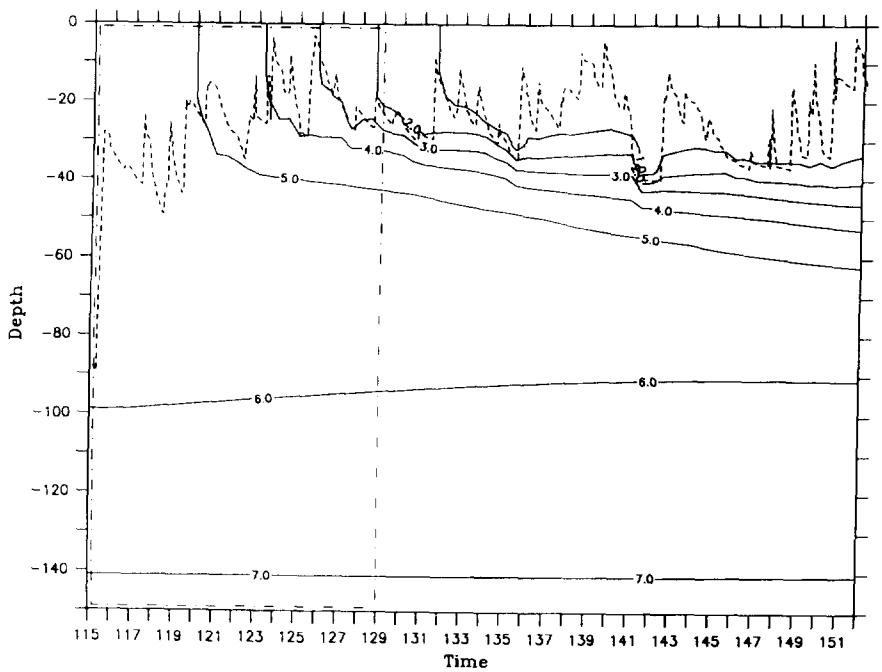


(b)

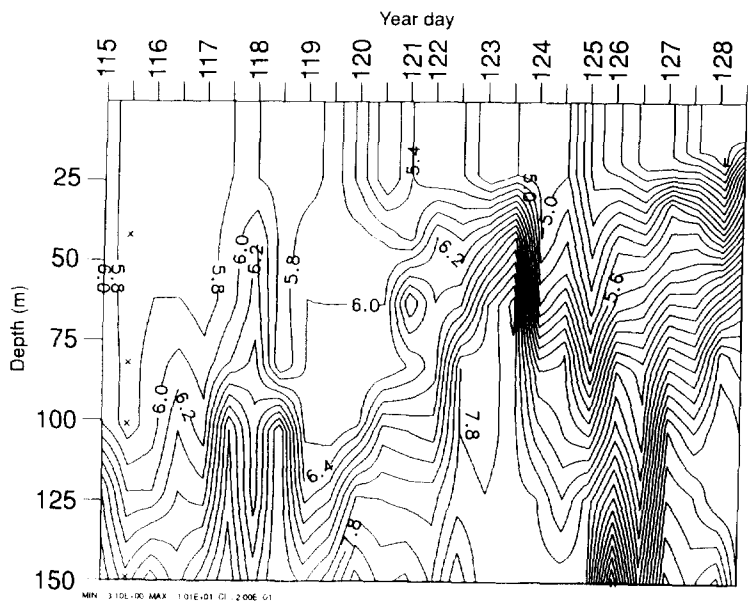


Fig. 11. (a) The evolution of the nitrate profile for the Early/Outside simulation. The dashed line indicates the location of the mixed layer depth during the time series. The dashed–dotted line denotes the extent of the data shown in (b). In (b) the spacing between days appears to vary because the contouring algorithm spaces the casts regularly and some days have multiple casts while other do not.

(a)

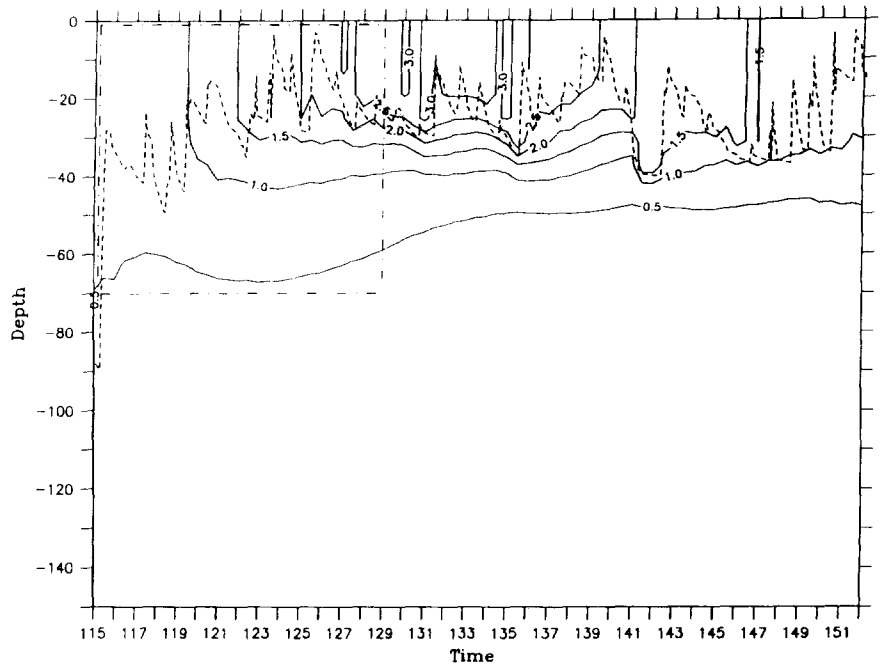
Depth
Time
0
-20
-40
-60
-80
-100
-120
-140
115 117 119 121 123 125 127 129 131 133 135 137 139 141 143 145 147 149 151
0.5
1.0
1.5
2.0
3.0

(b)

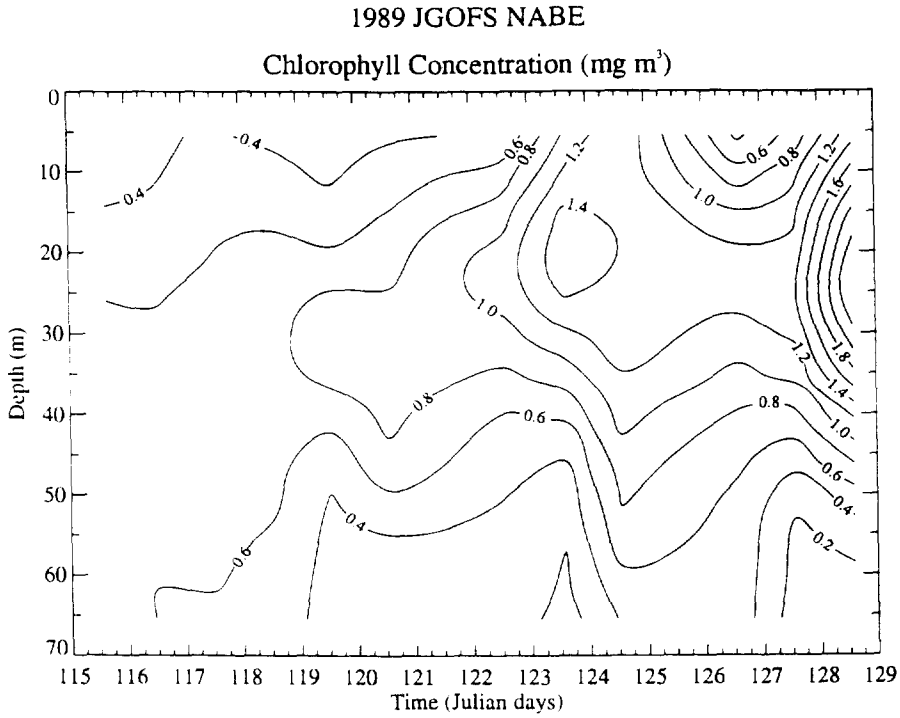
1989 JGOFS NABE
Chlorophyll Concentration (mg m$^3$)
Depth (m)
Time (Julian days)
0
10
20
30
40
50
60
70
115 116 117 118 119 120 121 122 123 124 125 126 127 128 129
0.2
0.4
0.6
0.8
1.0
1.2
1.4
1.6
1.8

model generates a bloom in the heterotrophic population that is closely coupled to the phytoplankton crop. Peak values occur at approximately the same time (day 135). The vertical distribution of heterotrophs is similar to the phytoplankton in that abundance is greatest in the mixed layer and decreases rapidly below the euphotic zone. Some decrease in heterotropic abundance with time is evident in the deepest layers due to mortality.

The evolution of the model ammonium profiles is shown in Fig. 15. No ammonium measurements were made during this time outside the eddy. However, the presence of a strong subsurface ammonium maximum is consistent with the observations made later inside the eddy (see below).

The integrated *f*-ratio for the upper 50 m is shown in Fig. 16a. Early in the simulation the *f*-ratio is quite high (0.8) as the predominant source of nitrogen for phytoplankton nutrition is nitrate, owing to a paucity of ammonium early in the bloom. As heterotrophs accumulate and produce ammonium, the *f*-ratio drops to approximately 0.4 by day 128. Although there are no direct measurements of the *f*-ratio for the first leg, Bender *et al.* (1992) used the rate of disappearance of nitrate computed from the observations and the rate of carbon incorporation measured in the $^{14}C$ incubations to compute an average *f*-ratio of 0.37. However, because of the previously mentioned bias in the observations of moving from a warm feature to a colder feature, the rate of nitrate disappearance was probably underestimated, resulting in underestimation of the *f*-ratio.

A comparison of the simulated optical properties with observations is shown in Fig. 16b. During the first leg the diffuse attenuation coefficient for photosynthetically available radiation increases by roughly 70% due to the accumulation of chlorophyll in the water column. The model agrees quite well with the data.

### 7.2. *Late/Inside*

The evolution of the model temperature profile is shown in Fig. 17a. It agrees quite well with the data taken inside the Small eddy on days 142 through 151 (Fig. 17b). The surface temperatures for the model and data are both about 13.6°C on day 142. A fairly sharp seasonal thermocline is centered at approximately 40 m. By day 151 the surface temperature has risen about 0.2°C and the seasonal thermocline has deepened and broadened slightly.

Figure 18a shows the model evolution of the nitrate profile. In general there is good agreement with the data (Fig. 18b). On day 142 the surface values are between 1$\mu M$ and 2 $\mu M$, and the nitracline is centered at 40 m. Nitrate is removed from the surface waters during the time series, and the transition to surface values below 1 $\mu M$ occurs on day 143 in both the model and the data. The nitracline deepens and broadens slightly from days 142 to 151. Although the location and magnitude of the nitracline are consistent with the observations, the gradient in the model is confined to a narrower depth interval. This is primarily a result of the fact that the model mixed layer is slightly deeper than the data indicate during this time. There is also some finer scale structure in the data (perhaps spatial) that is not represented in the model.

The evolution of the model phytoplankton profile is shown in Fig. 19a. The main

Fig. 12. (a) The evolution of the phytoplankton nitrogen profile for the Early/Outside simulation. The dashed line indicates the location of the mixed layer depth during the time series. The dashed–dotted line denotes the extent of the chlorophyll data shown in (b).

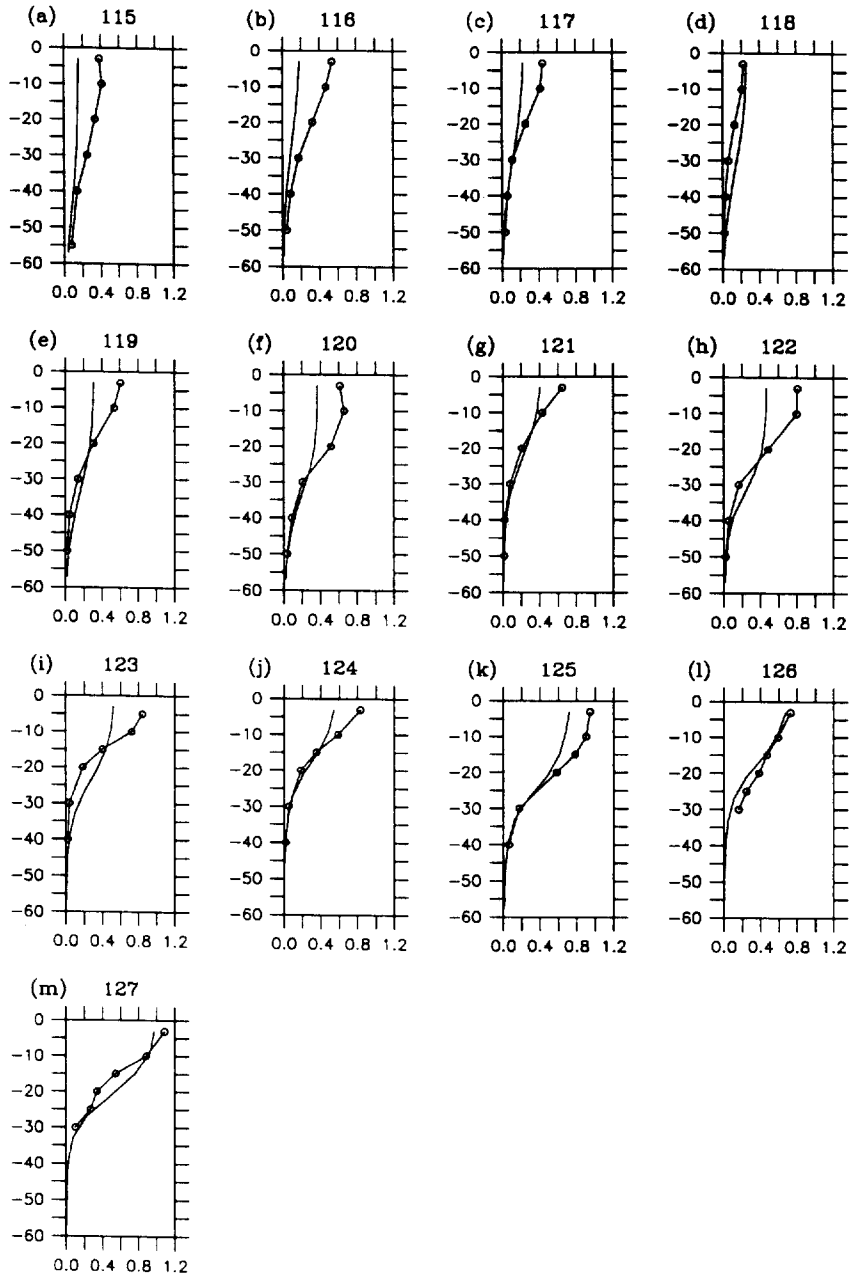


Fig. 13. Comparison of simulated primary productivity (solid lines) with $^{14}C$ incubations (open circles connected by solid lines) for days (a) 115, (b) 116, (c) 117, (d) 118, (e) 119, (f) 120, (g) 121, (h) 122, (i) 123, (j) 124, (k) 125, (l) 126, (m) 127.

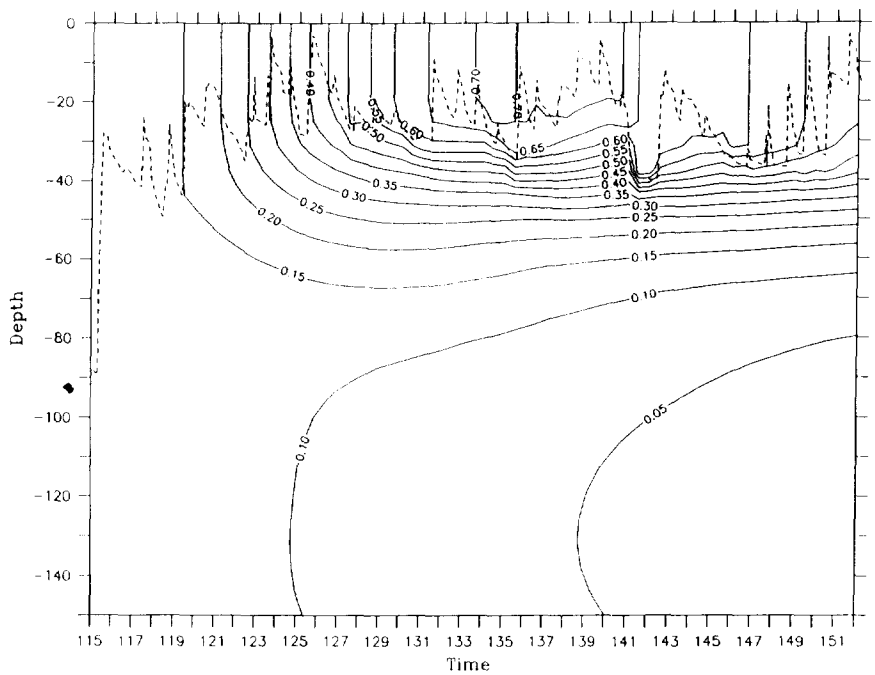


Fig. 14. The evolution of the heterotroph profile for the Early/Outside simulation. The dashed line indicates the location of the mixed layer depth during the time series.

features are in general agreement with the data (Fig. 19b). The surface phytoplankton first increases slightly and then begins to decrease. The magnitudes of the standing stocks and relative changes are not in exact agreement, but this difference is within the uncertainty in the chlorophyll to nitrogen ratio. It is interesting to note that there is more vertical structure in the chlorophyll data than there is in the model. One possible explanation for this could be photoadaptation by the cells in the real ocean that is not represented in the present model. That is, the observed subsurface chlorophyll maxima may be a result of an increase in the chlorophyll to nitrogen ratio, not an increase in phytoplankton biomass. There are many other potential explanations for the differences between the model and data, including changes in species composition, patchiness of the populations, etc. However, without more data it is impossible to assess these possibilities.

A comparison of simulated primary productivity profiles with data from *in situ* $^{14}C$ incubations is shown in Fig. 20. The agreement between the model and the data is quite good except for the last day (151) on which the model significantly underpredicts near surface productivity. Term by term analysis of the biological model equations facilitates diagnosis of the cause of this discrepancy. Figure 21 shows a time series of the nutrient limitation factor $Q$ in the phytoplankton growth equation (equation 10) for this simulation. Between days 142 and 149 phytoplankton growth is only weakly constrained by nutrient availability with $Q$ values of approximately 0.75 in the upper 20 m. After day 149 $Q$ falls precipitously to values below 0.55, indicating the onset of significant nutrient limitation. It therefore appears that the reduced rate of primary productivity in the model was a result of a slightly premature transition to oligotrophy.

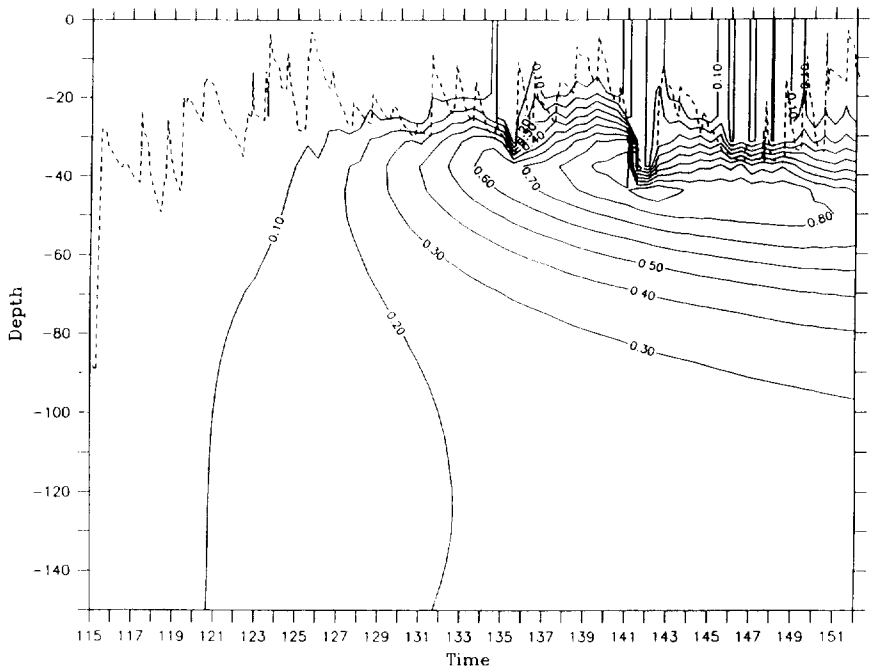


Fig. 15. The evolution of the ammonium profile for the Early/Outside simulation. The dashed line indicates the location of the mixed layer depth during the time series.

Time series of the heterotrophic population is shown in Fig. 22. Again the heterotrophic bloom is commensurate with that of the phytoplankton. Peak values of approximately 0.7 $\mu M$ N occur in the mixed layer on day 135 and persist throughout the rest of the simulation. Data are available for some zooplankton size classes during this time period. Dam *et al.* (1993) documented the biomass distribution of the mesozooplankton (200–2000 $\mu$m) and found that their grazing impact on phytoplankton was quite small (only a few percent of total primary production). Sieracki *et al.* (1993) showed that the mesozooplankton represent a small (10% or less) fraction of the total heterotrophic biomass. These data are consistent with the hypothesis that the microzooplankton are the dominant grazers of phytoplankton. Sieracki *et al.* (1993) also examined the 2–20 $\mu$m size fraction of the heterotrophic nanoplankton. Although their distribution is patchy and shows some vertical structure, the integrated biomass in the upper 30 m is relatively constant between days 141 and 151 (see Sieracki *et al.*, Table 3). This pattern is consistent with the model heterotrophic distribution in that abundance in the mixed layer changes little during this time period. However, the vertical structure within the mixed layer in the heterotrophic nanoplankton data is not represented in the model as the motility of these organisms is not included in the formulation. Exact quantitative biomass comparisons are made difficult by a variety of factors, including uncertainty in the carbon to nitrogen ratio of these organisms and the fact that some size classes were poorly sampled. However, the mean microzooplankton biomass for this period reported by Sieracki *et al.* is 2100 mgC/m$^2$ (Table 3, total heterotrophs minus bacteria minus mesozooplankton). Converted to

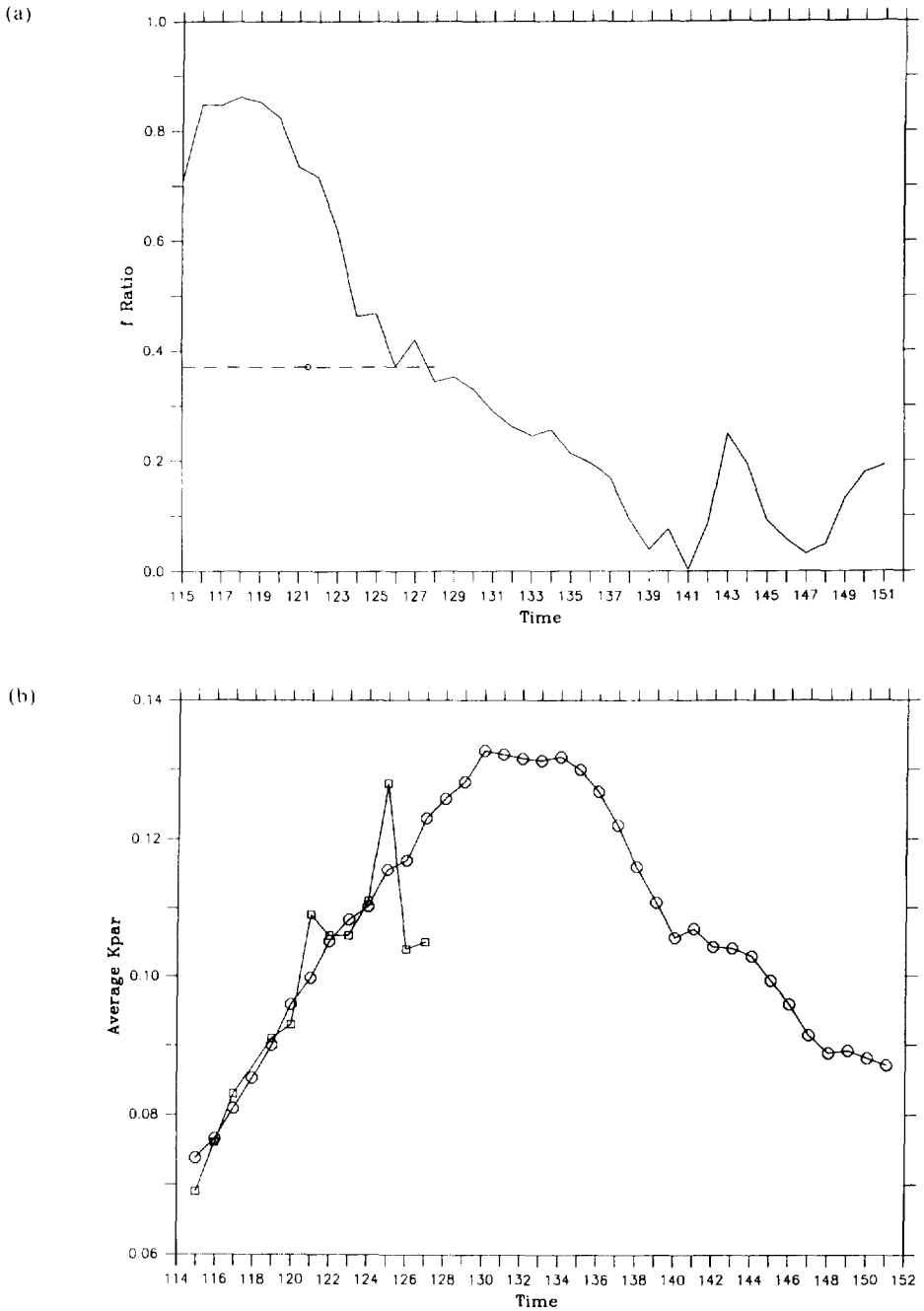


Fig. 16. (a) A time series of the depth integrated *f*-ratio for the Early/Outside simulation. The Bender *et al.* (1992) estimation of the Leg 1 *f*-ratio is denoted as an open circle with a dashed line to indicate the temporal extent of the data used to compute this average value (see text). (b) A time series of the simulated (circles) and measured (squares) diffuse attenuation coefficient for photosynthetically available radiation.

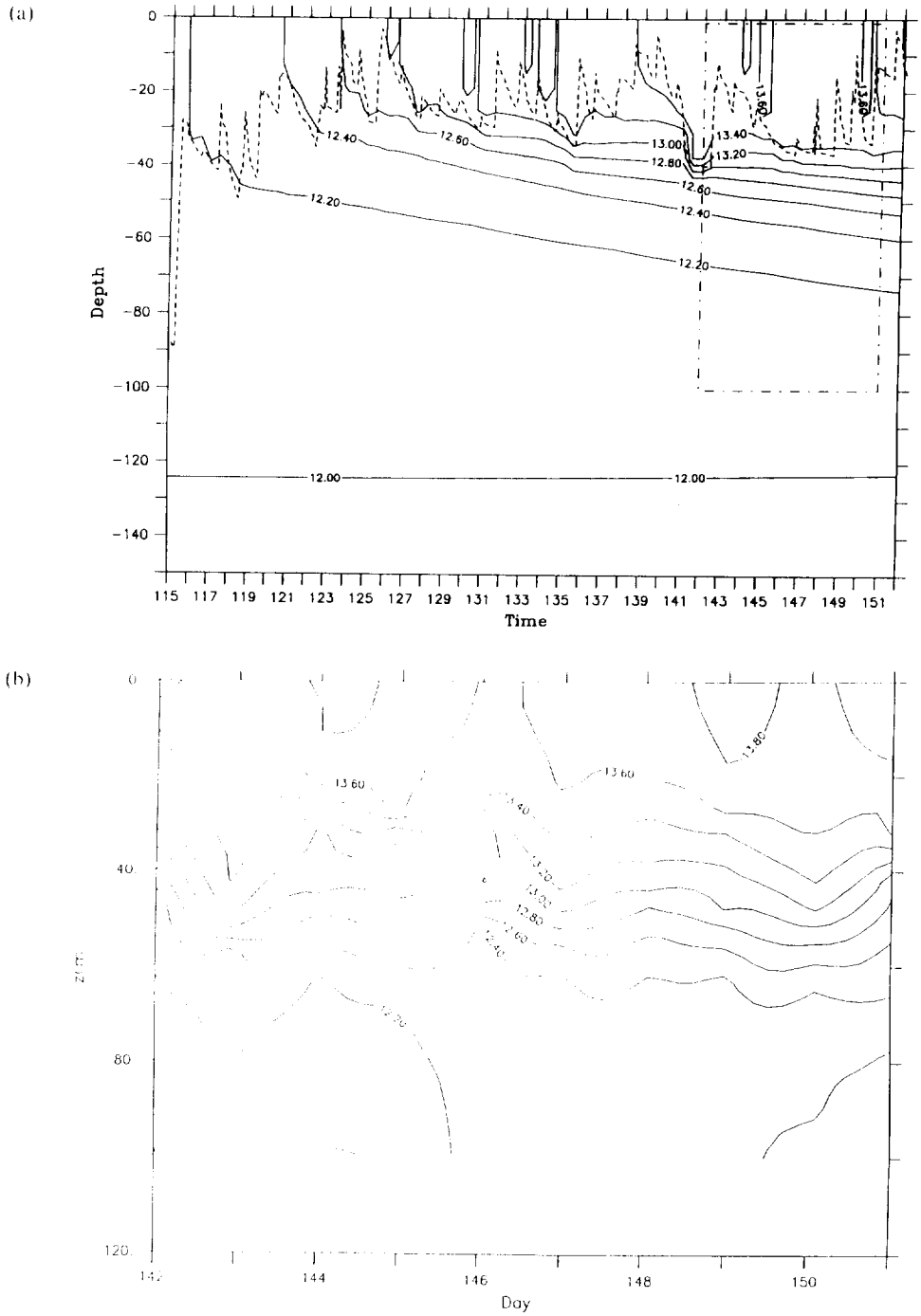


Fig. 17. (a) The evolution of the temperature profile for the Late/Inside simulation. The dashed line indicates the location of the mixed layer depth during the time series. The dashed–dotted line denotes the extent of the data shown in (b).

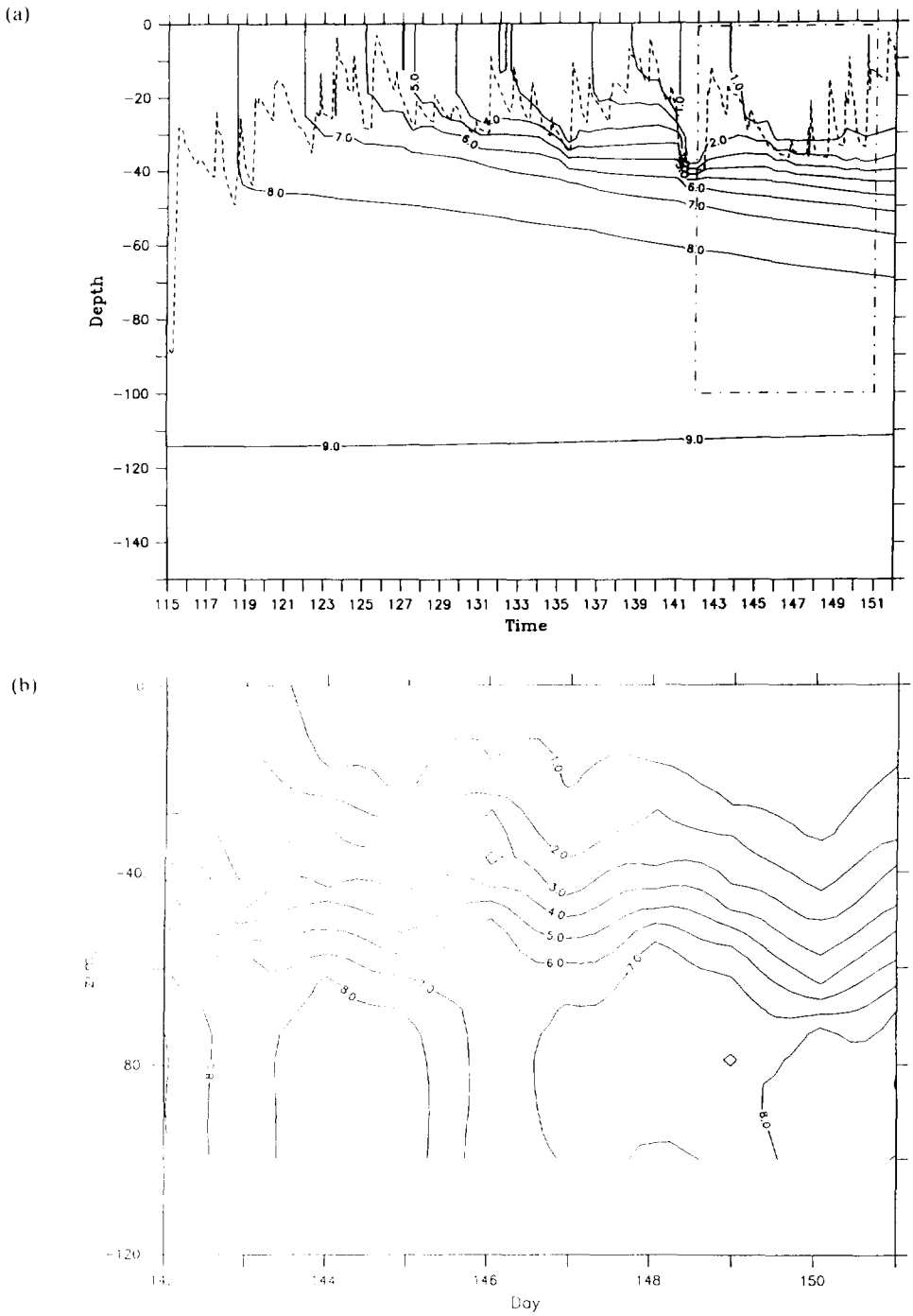


Fig. 18. (a) The evolution of the nitrate profile for the Late/Inside simulation. The dashed line indicates the location of the mixed layer depth during the times series. The dashed–dotted line denotes the extent of the data shown in (b).

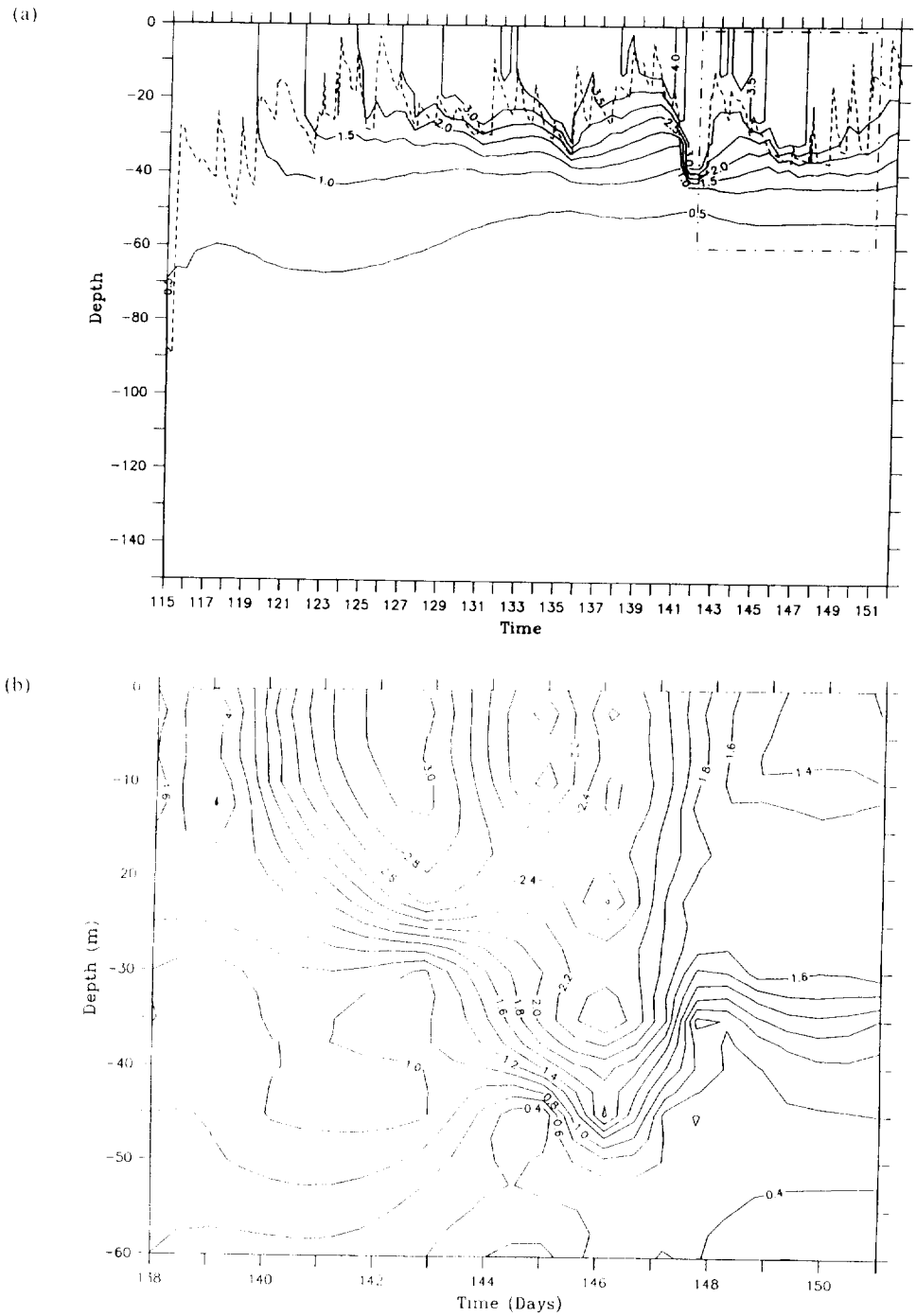


Fig. 19. (a) The evolution of the phytoplankton nitrogen profile for the Late/Inside simulation. The dashed line indicates the location of the mixed layer depth during the time series. The dashed–dotted line denotes the extent of the data shown in (b).

*Table 3. Normalized root mean square sensitivity of the seven diagnostic quantities to parameter variations of magnitude δ (relative units)*

| Parameter | | δ | $NO_3$ | | | | | $P$ | | | | $H$ | | | | $NH_4$ | | | | $PP$ | | | | $f$ | | | | $N_E$ | | | |
|---|---|---|---|---|---|---|---|---|---|---|---|---|---|---|---|---|---|---|---|---|---|---|---|---|---|---|---|---|---|---|---|
| 1 | $k_w$ | — | — | — | — | — | — | — | — | — | — | — | — | — | — | — | — | — | — | — | — | — | — | — | — | — | — | — | — | — | — |
| 2 | $k_c$ | 0.2 | 1.50 | 1.01 | 1.25 | 4.44 | 3.11 | 3.78 | 1.29 | 0.89 | 1.09 | 0.68 | 0.44 | 0.56 | 2.56 | 3.24 | 2.90 | 0.65 | 0.89 | 0.77 | 0.59 | 0.50 | 0.54 | | | | | | | | |
| 3 | $P_{max}$ | 0.2 | 2.35 | 5.11 | 3.73 | 7.33 | 12.04 | 9.68 | 1.51 | 5.27 | 3.39 | 1.85 | 3.55 | 2.70 | 6.16 | 8.10 | 7.13 | 1.58 | 1.05 | 1.31 | 1.08 | 2.56 | 1.82 | | | | | | | | |
| 4 | $p_1$ | 0.2 | 0.64 | 1.31 | 0.97 | 1.82 | 3.77 | 2.79 | 0.47 | 1.02 | 0.75 | 0.45 | 0.75 | 0.60 | 1.89 | 1.90 | 1.90 | 0.43 | 0.50 | 0.46 | 0.30 | 0.50 | 0.40 | | | | | | | | |
| 5 | $p_2$ | — | — | — | — | — | — | — | — | — | — | — | — | — | — | — | — | — | — | — | — | — | — | | | | | | | | |
| 6 | $k_1$ | — | — | — | — | — | — | — | — | — | — | — | — | — | — | — | — | — | — | — | — | — | — | | | | | | | | |
| 7 | $k_2$ | — | — | — | — | — | — | — | — | — | — | — | — | — | — | — | — | — | — | — | — | — | — | | | | | | | | |
| 8 | $k_n$ | 0.2 | 1.00 | 0.65 | 0.82 | 2.87 | 1.78 | 2.33 | 0.72 | 0.48 | 0.60 | 0.78 | 0.68 | 0.73 | 1.20 | 1.89 | 1.54 | 0.34 | 0.49 | 0.42 | 0.35 | 0.28 | 0.32 | | | | | | | | |
| 9 | $R_m$ | 0.2 | 5.65 | 1.89 | 3.77 | 16.16 | 15.50 | 15.83 | 6.85 | 2.81 | 4.83 | 4.24 | 0.97 | 2.61 | 8.85 | 7.28 | 8.07 | 2.61 | 2.27 | 2.44 | 2.21 | 2.08 | 2.15 | | | | | | | | |
| 10 | $\Lambda$ | 1.0 | 1.55 | 0.53 | 1.04 | 4.24 | 8.21 | 6.22 | 2.20 | 3.78 | 2.99 | 0.87 | 1.81 | 1.34 | 2.64 | 2.33 | 2.48 | 0.96 | 2.56 | 1.76 | 0.73 | 1.49 | 1.11 | | | | | | | | |
| 11 | $\gamma$ | 0.2 | 0.69 | 1.38 | 1.03 | 5.01 | 6.55 | 5.78 | 1.11 | 1.34 | 1.22 | 0.93 | 1.47 | 1.20 | 2.47 | 1.84 | 2.16 | 0.72 | 0.60 | 0.66 | 0.76 | 0.48 | 0.62 | | | | | | | | |
| 12 | $n_1$ | 0.4 | 0.59 | 1.50 | 1.04 | 3.38 | 5.25 | 4.32 | 1.21 | 1.30 | 1.25 | 0.20 | 0.68 | 0.44 | 1.88 | 1.85 | 1.87 | 0.60 | 0.63 | 0.62 | 0.08 | 0.49 | 0.29 | | | | | | | | |
| 13 | $n_2$ | 0.2 | 0.83 | 2.73 | 1.78 | 5.79 | 10.62 | 8.21 | 1.83 | 2.81 | 2.32 | 0.37 | 1.82 | 1.09 | 3.44 | 4.21 | 3.82 | 1.05 | 1.46 | 1.25 | 0.53 | 0.53 | 0.53 | | | | | | | | |
| 14 | $\varepsilon_1$ | 0.2 | 0.14 | 0.16 | 0.15 | 0.73 | 0.63 | 0.68 | 0.13 | 0.10 | 0.11 | 1.08 | 1.07 | 1.07 | 0.38 | 0.37 | 0.38 | 0.26 | 0.25 | 0.25 | 0.68 | 0.69 | 0.69 | | | | | | | | |
| 15 | $\varepsilon_2$ | 0.2 | 0.26 | 0.32 | 0.29 | 1.24 | 0.94 | 1.09 | 0.22 | 0.13 | 0.17 | 0.79 | 0.78 | 0.79 | 0.91 | 0.72 | 0.81 | 0.35 | 0.34 | 0.35 | 0.90 | 0.92 | 0.91 | | | | | | | | |
| 16 | $w_{sink}$ | 0.2 | 0.13 | 0.12 | 0.13 | 0.59 | 0.55 | 0.57 | 0.05 | 0.05 | 0.05 | 0.07 | 0.08 | 0.07 | 0.26 | 0.33 | 0.29 | 0.08 | 0.09 | 0.09 | 0.02 | 0.01 | 0.01 | | | | | | | | |
| 17 | $f_w$ | 0.2 | 0.19 | 0.17 | 0.18 | 0.74 | 0.68 | 0.71 | 0.07 | 0.06 | 0.07 | 0.06 | 0.07 | 0.06 | 0.35 | 0.46 | 0.41 | 0.09 | 0.10 | 0.10 | 0.05 | 0.04 | 0.04 | | | | | | | | |

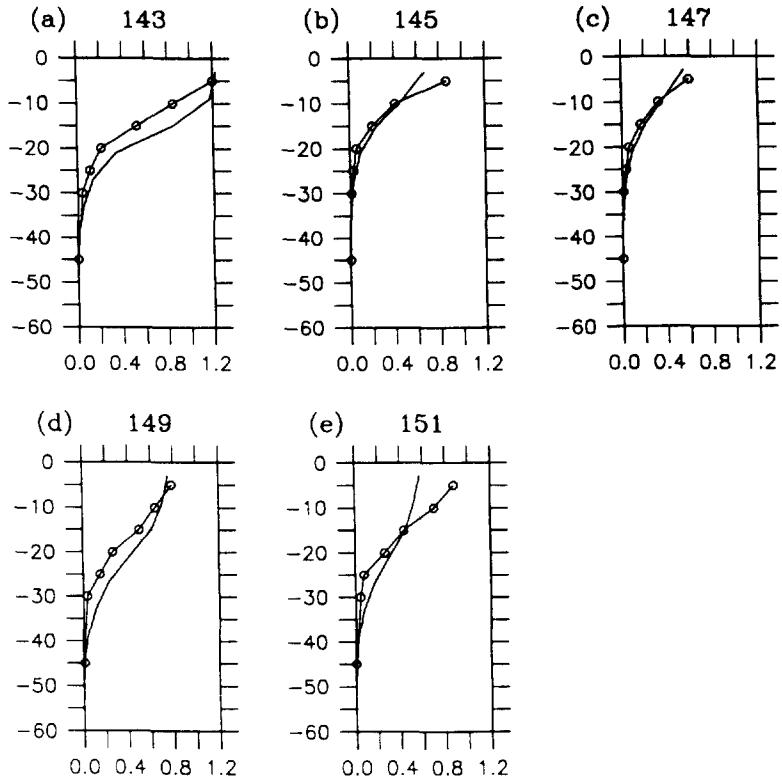


Fig. 20. Comparison of simulated primary productivity (solid lines) with $^{14}C$ incubations (open circles connected by solid lines) for days (a) 143, (b) 145, (c) 147, (d) 149, (e) 151.

nitrogen units according to the Redfield ratio, this corresponds to 0.87 $\mu M$ N which is quite similar to the model predicted value.

The evolution of the model ammonium concentration is shown in Fig. 23a. It agrees quite well with the data shown in Fig. 23b. A subsurface maximum has developed centered at about 45–50 m with maximum values that increase with time. The data indicate an increase in the subsurface maximum from around 0.7 $\mu M$ to approximately 1.4 $\mu M$, while the model increases from 1.1 $\mu M$ to about 1.3 $\mu M$. Measurable quantities of ammonium are present somewhat deeper in the model than indicated by the data. The lack of ammonium at depths below about 80 m in the data may be a result of uptake by autotrophs that live deep in the water column (such as cyanobacteria) that are not represented in the model. Alternatively the excess ammonium at depth in the model may be a result of the omission of nitrification processes in the model formulation. These processes are generally thought to occur only near the bottom of the euphotic zone (Wada and Hattori, 1971; Ward, 1987; Ward & Zafiriou, 1988) yet recent evidence suggests nitrification can occur in the nitracline at depths as shallow as 6% surface light intensity (Ward *et al.*, 1989).

The simulated integrated *f*-ratio agrees reasonably well with the *f*-ratio computed from the ratio of nitrate uptake to total uptake measured experimentally (Fig. 24a). Momentarily depressed by an injection of ammonium into the mixed layer due to mixing caused by the storm on day 141, the simulated *f*-ratio is approximately correct at the start of the

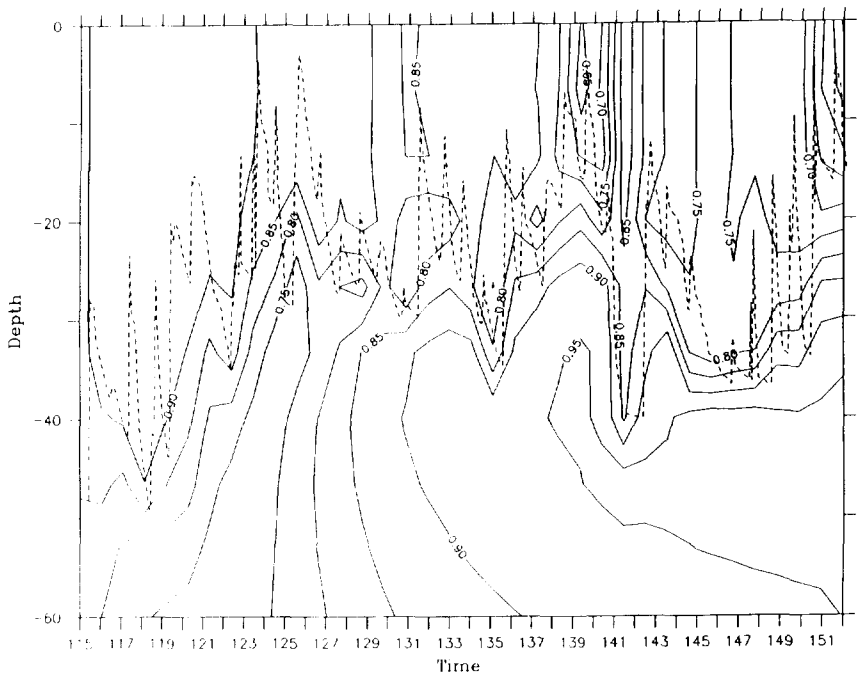


Fig. 21. The evolution of the nutrient limitation factor $Q$ for the Late/Inside simulation.

observations on day 143. From days 146 to 148, the model $f$-ratio is too low, but agrees well with the data on days 149 and 151.

A comparison of the simulated optical properties with observations is shown in Fig. 24b. The model agrees well with the data that are available for the latter part of the simulation. Note that this simulation also agrees well with the observations collected outside the eddy early in the time period. This results from the fact that early in the bloom phytoplankton growth is almost entirely light limited. Because the Early/Outside and Late/Inside simulations have exactly the same initial phytoplankton biomass and similar growth rates, the phytoplankton accumulation in the early bloom of the two runs is almost identical.

### 7.3. *Quasi-equilibrium solutions*

The preceding simulations demonstrate the efficacy of the one dimensional model in representing the general features of the spring bloom. However, in analyzing the behavior of these solutions to the biological model equations, it is important to differentiate between the response caused by external forcing and that which is a result of the model adjusting to initial conditions which may not necessarily be at equilibrium. In order to ascertain how much of the behavior in these simulations was simply a result of adjustment to the biological initial conditions, a simulation was conducted in which the mixed layer depth was held constant at its initial depth of 90 m. The overall character of these quasi-equilibrium solutions is quite different from the simulations described above (not shown). Although there is some accumulation of phytoplankton and removal of nutrients, the

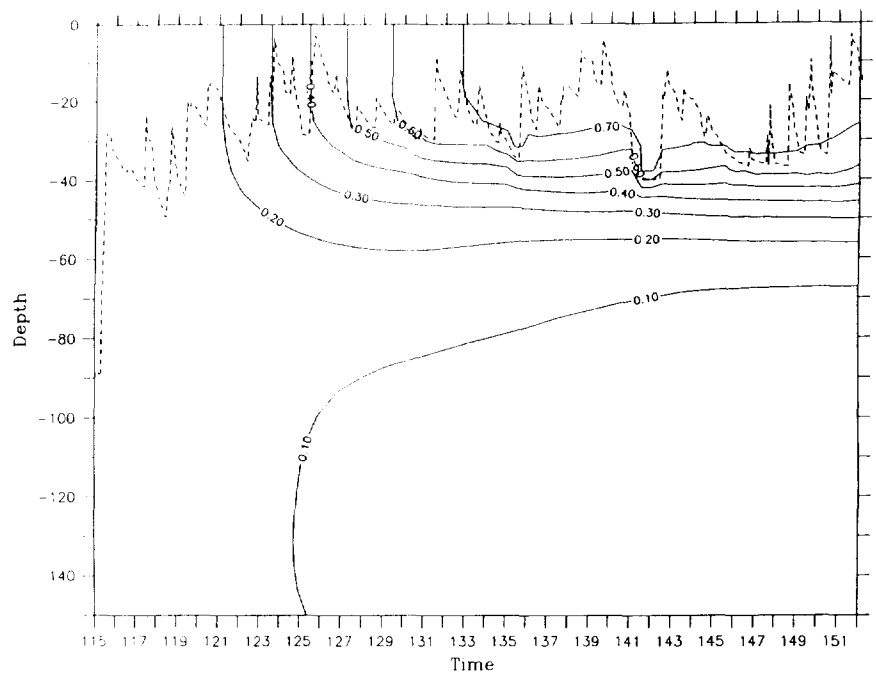


Fig. 22. The evolution of the heterotroph profile for the Late/Inside simulation. The dashed line indicates the location of the mixed layer depth during the time series.

magnitude of the bloom is greatly reduced as is the nutrient drawdown. Hence it can be concluded that the behavior of the Early/Outside and Late/Inside simulations is mostly a forced response rather than adjustment to disequilibrium in the initial conditions.

## 8. PARAMETER DEPENDENCE AND SENSITIVITY ANALYSIS

It is of interest to understand how the model solutions depend on the various parameters and how sensitive the solutions are to particular choices of those parameters. To accomplish this a set of numerical experiments were conducted in which the parameters were systematically varied about the central values used in the preceding section. These central values are considered to be the most realistic insofar as they produce a model trajectory that best represents the observations. Each of the experiments described below consists of two simulations, one in which a given parameter is increased and one in which it is decreased. The differences in the qualitative behavior between these simulations and the central run (inside the Small eddy) will elucidate the dependence of the solution on the

Fig. 23. (a) The evolution of the ammonium profile for the Late/Inside simulation. The dashed line indicates the location of the mixed layer depth during the time series. The dashed–dotted line denotes the extent of the data shown in (b).

(a)

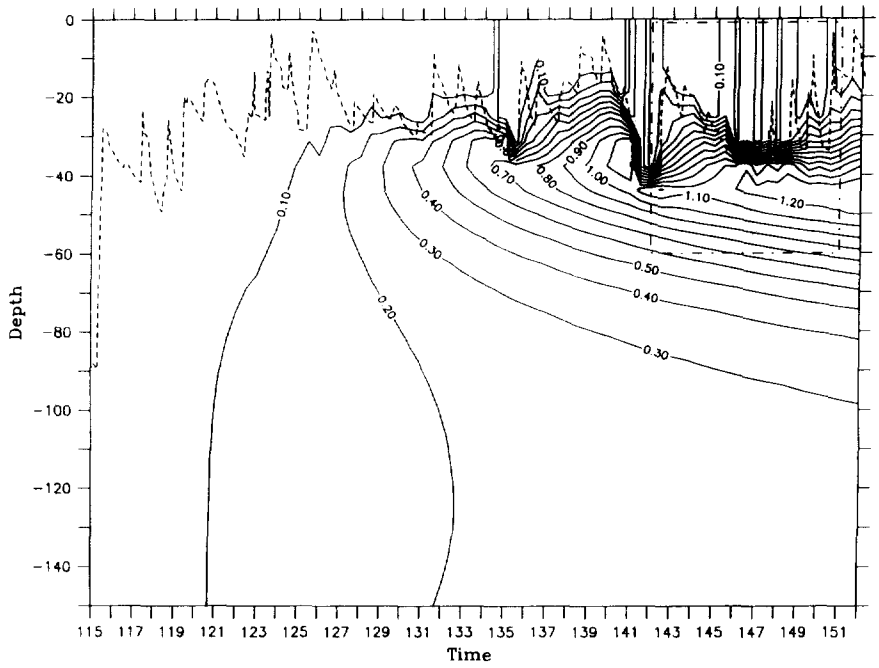
Depth
0
-20
-40
-60
-80
-100
-120
-140
115 117 119 121 123 125 127 129 131 133 135 137 139 141 143 145 147 149 151
Time
0.10
0.20
0.30
0.40
0.50
0.60
0.70
0.80
0.90
1.00
1.10
1.20

(b)

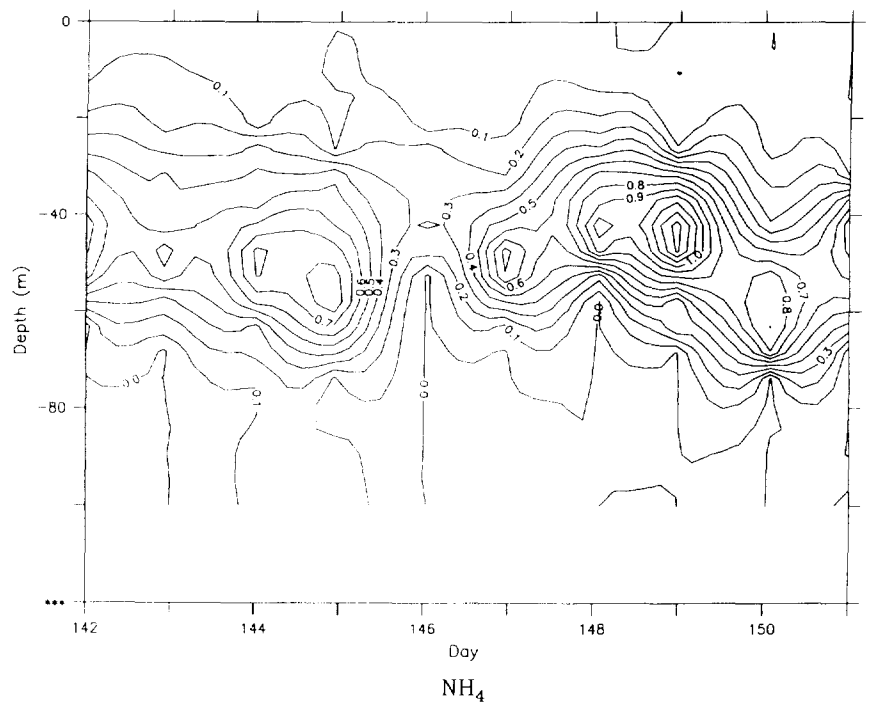
Depth (m)
0
-40
-80
142
144
146
148
150
Day

$NH_4$

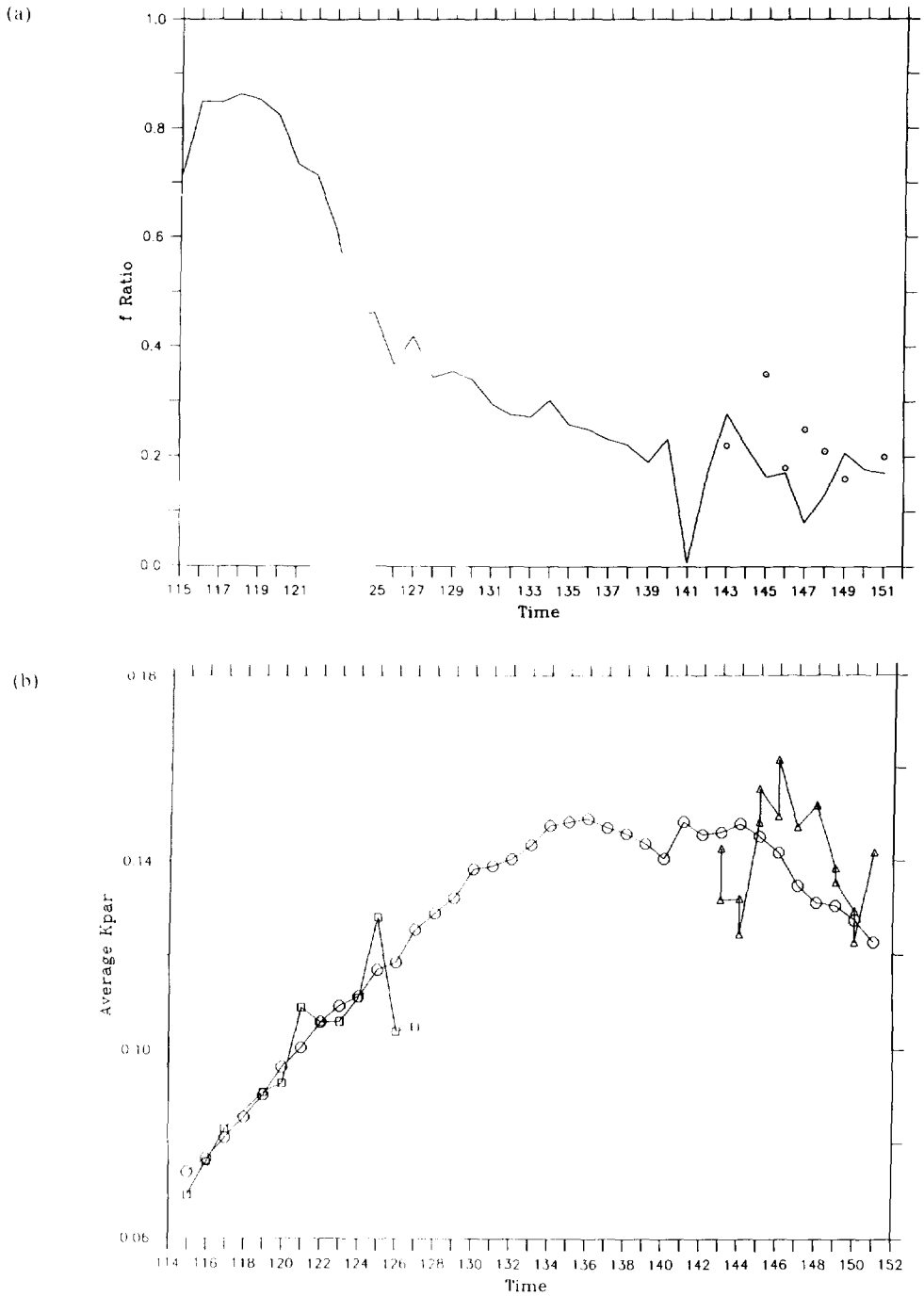


Fig. 24. (a) A time series of the integrated *f*-ratio for the Late/Inside simulation. Estimates based on data by McCarthy and Nevins (1993) are shown as open circles. (b) A time series of the simulated (circles) and measured (Leg 1: squares; Leg 2: triangles) diffuse attenuation coefficient for photosynthetically available radiation.

parameter. A quantitative estimate of normalized parameter sensitivity $S(P)$ is computed in a manner similar to Fasham *et al.* (1990):

$$S(P) = \frac{\dfrac{1}{t_2 - t_1} \displaystyle\int_{t_1}^{t_2} \frac{D(P) - D_c}{D_c}\, dt}{\left| \dfrac{P - P_c}{P_c} \right|}$$

The numerator is the temporally integrated normalized root mean square difference between a particular diagnostic quantity in a sensitivity run $D(P)$ and the value of that diagnostic for the central run $D_c$. This root mean square difference is normalized by the magnitude of the parameter perturbation from its value $P_c$ in the central run. The diagnostic quantities used in this analysis are time series of spatially integrated nitrate, phytoplankton, heterotrophs, ammonium, exported nitrogen, primary production and *f*-ratio. For brevity the time series of diagnostic quantities is shown for only one parameter sensitivity experiment ($P_{max}$). The results of the remaining experiments will be described and presented in summary form only (see below). The normalized sensitivites of the seven diagnostic quantities to each parameter are listed in Table 3 and displayed graphically in Fig. 25. The parameters $k_w$, $P_2$, $k_1$ and $k_2$ have been excluded from this analysis because they are well constrained by data, either from the NABE or the literature.

As an example, consider the maximum rate of photosynthesis $P_{max}$. This parameter sets the scale of the phytoplankton growth rate expression. Of the seven diagnostic quantities, this parameter affects phytoplankton and primary productivity the most, for obvious reasons (Fig. 25b). Increasing $P_{max}$ causes the bloom to occur earlier and much more phytoplankton nitrogen accumulates during its peak (Fig. 26). The change in the timing and magnitude of the bloom causes nitrate to be drawn down more rapidly. The integrated nitrate curve flattens out as the nitrate in the surface waters is depleted. Subsequent to the onset of oligotrophy, heterotrophs rapidly consume the excess phytoplankton nitrogen, so that after day 140 the integrated phytoplankton curve is nearly coincident with that of the central run. Nutrient recycling by the larger heterotrophic biomass causes increases in both the ammonium and exported nitrogen reservoirs, while leaving the *f*-ratio relatively unaffected.

When $P_{max}$ is decreased, there is hardly any bloom at all. Heterotrophs overtake the phytoplankton population before and significant bloom occurs. At this growth rate, phytoplankton simply cannot outpace the heterotrophic grazing pressure. There is a marked asymmetry in the model response to this parameter perturbation, owing to the fact that the most salient feature of the simulation has dramatically changed in character. Much less nitrate is removed from the water column than in the central run. Heterotrophs accumulate early in the simulation (albeit at a slower rate) but after day 135 they cannot meet their respiratory demands and therefore begin to die out. Much less ammonium is generated in this simulation, and nitrogen export is also reduced.

The normalized sensitivity of each of the seven diagnostics to the various parameters is summarized in Fig. 27. By far the two most sensitive parameters are the maximum growth rates for phytoplankton and heterotrophs (parameters 3 and 9). Unfortunately, these are parameters for which no direct measurements are available during NABE. Because these rates are so crucial to the functioning of the ecosystem, it would be advisable to make such observations in future experiments of this type. The model solutions are also quite

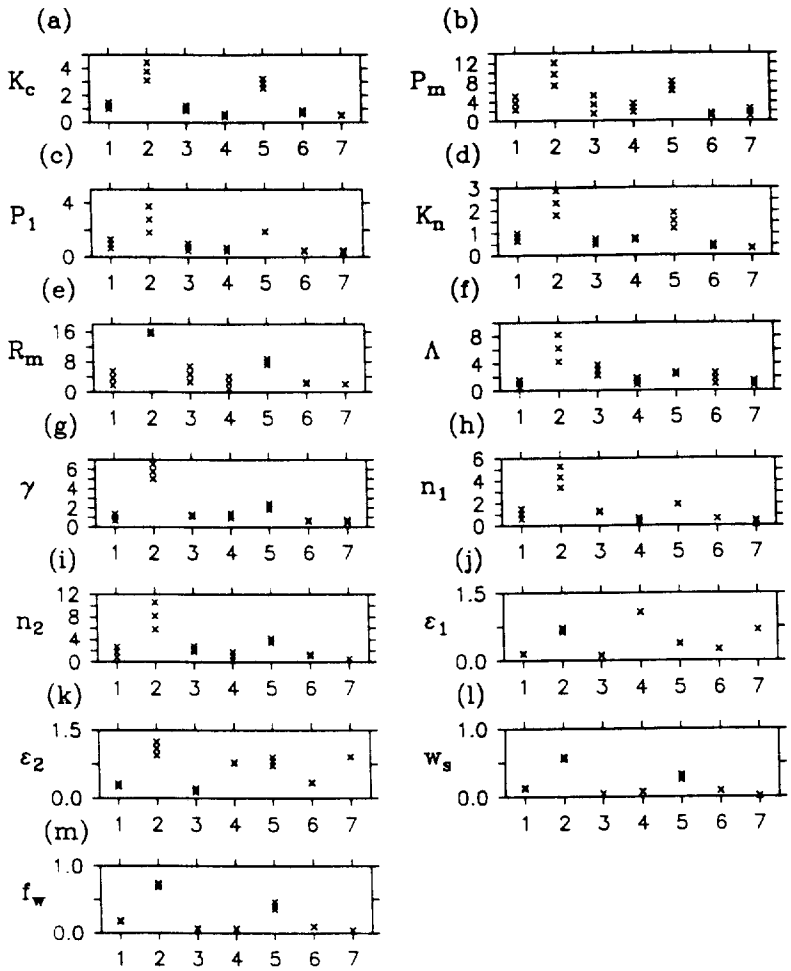


Fig. 25. Root mean square difference in the seven diagnostic quantities for the parameter sensitivity experiments. Numerals 1 through 7 correspond to (1) nitrate (2) phytoplankton (3) heterotrophs (4) ammonium (5) primary production (6) *f*-ratio (7) exported nitrogen. In each instance the values are shown for the high and low perturbations in addition to a mean value computed from the two cases.

sensitive to the quadratic heterotrophic loss rate (parameter 13), particularly as they relate to integrated nitrate, phytoplankton, heterotrophs, primary production and *f*-ratio. These sensitivities indicate that the balance between consumption and production is a critical factor in determining the character of the bloom.

## 9. SUMMARY AND CONCLUSIONS

A flexible three dimensional coupled physical and biological model has been introduced. It has been shown that a one dimensional implementation of this model is capable of capturing the general features of the spring bloom in the North Atlantic. However,

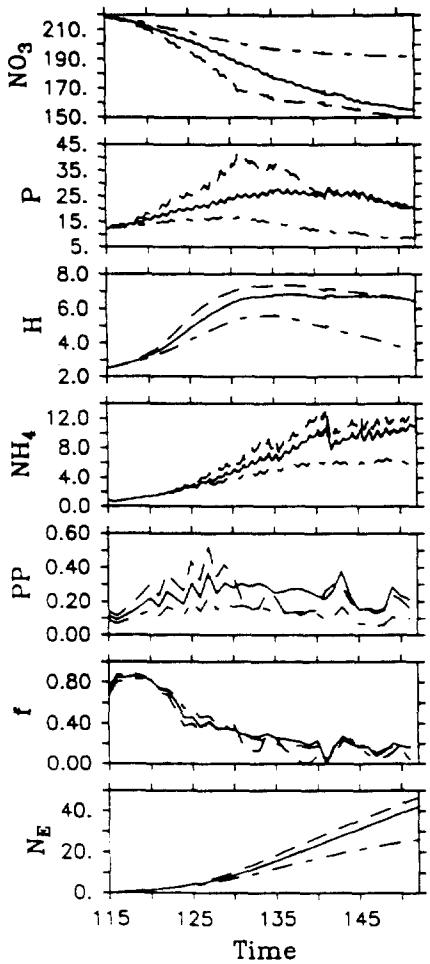


Fig. 26. Trajectories of integrated nitrate, phytoplankton, heterotrophs, ammonium, primary production, *f*-ratio and exported nitrogen for the central run (solid lines) and the simulations in which $P_{max}$ is higher (dashed lines) and lower (dashed–dotted lines) than the optimal value.

explicit treatment of the mesoscale variability within the one dimensional framework is critical to the success of the fit. The fact that the two main observational periods sampled different mesoscale water masses at different times (one early outside the Small eddy and one later inside the eddy) poses a problem because the initial "pre-bloom" nitrate profiles are quite different due to the mesoscale perturbation of the density surfaces. An assessment of this perturbation based on hydrographic and altimetric information (Robinson *et al.*, 1993) and a coherent nitrate–density relationship (Fig. 4) permit reasonable estimation of the pre-bloom nitrate profile inside the Small eddy. This provides the initial conditions required to run parallel simulations inside and outside the eddy that both start at the same time in the pre-bloom situation.

The simulation inside the eddy shows good agreement with the Late/Inside data set. The seasonal thermocline that forms in the model from an initially well mixed layer is

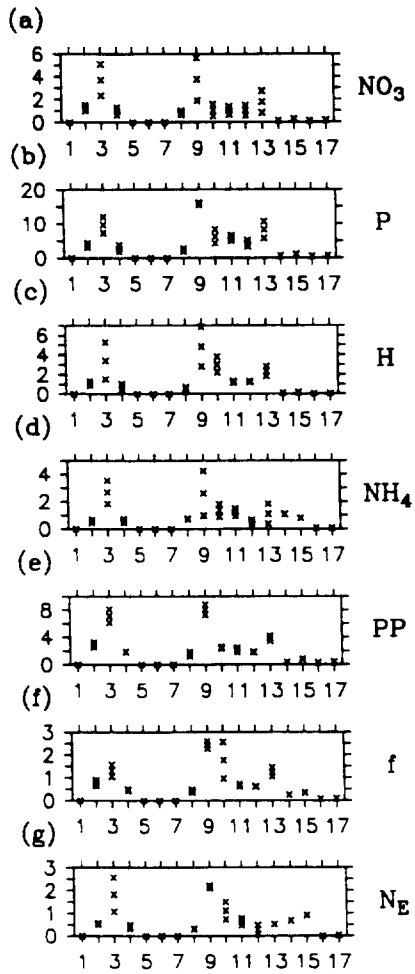


Fig. 27. Root mean square difference in the seven diagnostic quantities for the parameter variations in the sensitivity experiments. Numerals 1 through 17 correspond to the parameter numbers in Table 3. In each instance the values are shown for the high and low perturbations in addition to a mean value computed from the two cases.

consistent with the data in both strength and vertical extent. Sea surface temperatures also coincide. There is similar agreement between the model and data in the formation of the nitracline. The rate of removal during the observational period is consistent both in the mixed layer itself and in the deepening of the nitracline. Chlorophyll observations show more variability and vertical structure than model phytoplankton nitrogen during this period, but much of the discrepancy could be attributed to variations in the chlorophyll to nitrogen ratio in the phytoplankton population. Simulated primary productivity matches the data very well except for on the last day of the time series when the model began to show signs of nutrient limitation. The model forms a subsurface ammonium maximum from an initially homogeneous profile that compares well with the observations. Model generated *f*-ratio is in good agreement with independent estimates based on uptake

measurements. Finally, the simulated inherent optical properties conform with bio-optical measurements.

Comparison of the simulation outside the eddy with the early time series is not as satisfactory partially because of a bias in the observations. While the late observational period is confined to the interior of the Small eddy, the early time series is somewhat biased in that the first observations are taken from a warm feature exterior to the eddy and subsequent measurements are made in cold features (the frontal region between the warm feature and the eddy and an additional cold feature to the west of the warm feature). This movement from warm to cold features causes an apparent sink of heat in the data which results in the simulated temperature profiles heating up more quickly than observed. Conversely, the bias represents an apparent source of nitrate in the data, causing the nutrient removal to seem excessive in the model. This apparent supply of nitrate reduces the estimates of utilization used by Bender *et al.* (1992) in computing an *f*-ratio for the time series, and significantly depresses their estimated *f*-ratio (0.37). Simulated *f*-ratios average almost a factor of two higher during this period (0.64). Thus, neglecting mesoscale structures in the context of the distribution of observations can significantly bias estimates of changes in water column properties with time. Put differently, spatial variability can be mistaken for temporal variability if care is not taken to separate the two. MRM95 demonstrates that the apparent discrepancy in nitrate drawdown can be reconciled with proper treatment of the space–time variability in the full three dimensional implementation of this model.

Discrepancies in phytoplankton and primary production are not as easy to understand. Phytoplankton populations are presumably light limited in the early phase of the bloom so the bias in the measurements should have less of an effect on these variables. However, primary production is systematically underestimated in the near surface region early in the time series. Agreement with observations at the end of the period is much better, but the reason for the early differences are not known. Phytoplankton nitrogen appears to build up slightly faster than chlorophyll based estimates would suggest. The degree to which phytoplankton chlorophyll to nitrogen ratios may have changed, which cannot be determined from the data, is relevant to this issue.

The two parallel simulations and sensitivity analyses corroborate early conclusions about ecosystem functioning during the bloom. There is a tight coupling between phytoplankton production and heterotrophic consumption as evidenced by the large differences in model results caused by perturbations to the phytoplankton and heterotroph growth rate parameters. In fact, grazing by heterotrophs is a major factor in regulating the phytoplankton population even early in the bloom. Not only does the heterotrophic activity decrease the amplitude of the phytoplankton biomass maximum at the peak of the bloom, it also delays the transition to oligotrophy by providing a substantial source of regenerated nutrients.

*Acknowledgements*—D.J.M. and A.R.R. were supported by ONR N00014-84-C-0461, N00014-90-J-1593 and N00014-93-1-0577. D.J.M. was also supported by an Office of Naval Research Graduate Fellowship and a VCAR Postdoctoral Modeling Fellowship. J.J.M. was supported by NSF OCE88-17830. The biological and chemical data sets used in this study were provided by numerous investigators both directly and via the JGOFS database. The help of George Heimerdinger, the manager of the U.S. JGOFS Data Management office is gratefully appreciated. His meticulous superintendence and expedient distribution of the data sets contributed a great deal to this effort. The following investigators are acknowledged for their various data sets: R. T. Williams, hydrography and nutrients; C. Knudson, W. S. Chamberlin and J. Marra, primary production and diffuse

attenuation; C. O. Davis and W. J. Rhea, bio-optical chlorophyll measurements; C. Garside, nutrients; S. Fitzwater and J. Martin, primary productivity and chlorophyll; W. Broenkow, irradiance; C. Trees, diffuse attenuation. The helpful comments of four anonymous reviewers are greatly appreciated.

## REFERENCES

Alldredge A. and C. C. Gotschalk (1989) Direct observations of mass flocculation of diatom blooms: characteristics, settling velocities and formation of diatom aggregates. *Deep-Sea Research*, **36**, 159–171.

Bender M., H. Ducklow, J. Kiddon, J. Marra and J. Martin (1992) The carbon balance during the 1989 spring bloom in the North Atlantic Ocean, 47N, 20W. *Deep-Sea Research*, **39**, 1707–1725.

Bienfang P. (1981) Sinking rates of heterogeneous, temperate phytoplankton populations. *Journal of Plankton Research*, **3**, 235–253.

Broenkow W., R. E. Reaves and M. A. Yarbrough (1990) JGOFS North Atlantic Bloom long track and vertical profiling results. Technical Report MLML 90-1, Moss Landing Marine Laboratory, Moss Landing, CA.

Capriulo G. (1990) *Ecology of marine protozoa*. Oxford University Press, New York.

Dam H., C. A. Miller and S. H. Jonasdottir (1993) The tropic role of mesozooplankton at 47N, 20W during the North Atlantic Bloom Experiment. *Deep-Sea Research II*, **40**, 197–212.

Ducklow H. and R. P. Harris (1993) Introduction to the JGOFS North Atlantic Bloom Experiment. *Deep-Sea Research II*, **40**, 1–8.

Fasham M., P. M. Holligan and P. R. Pugh (1983) The spatial and temporal development of the spring phytoplankton bloom in the Celtic Sea, April 1979. *Progress in Oceanography*, **12**, 87–145.

Fasham M., H. W. Ducklow and S. M. KcKelvie (1990) A nitrogen-based model of plankton dynamics in the oceanic mixed layer. *Journal of Marine Research*, **48**, 591–639.

Garside C. and J. C. Garside (1993) The "f-ratio" on 20°W during the North Atlantic Bloom Experiment. *Deep-Sea Research II*, **40**, 75–90.

Garwood R. (1977) An oceanic mixed layer model capable of simulating cyclic states. *Journal of Physical Oceanography*, **7**, 455–468.

Gill A. E. (1982) *Atmosphere–ocean dynamics*. Academic Press, New York.

Glover D. and P. G. Brewer (1988) Estimates of wintertime mixed layer nutrient concentrations in the North Atlantic. *Deep-Sea Research*, **35**, 1525–1546.

Goldman J. and P. M. Glibert (1983) Kinetics of inorganic nitrogen uptake by phytoplankton. In *Nitrogen in the marine environment*, E. Carpenter and D. G. Capone, editors, chapter 14, Academic Press, New York, pp. 487–512.

Kirk J. (1983) *Light and photosynthesis in aquatic ecosystems*. Cambridge University Press, Cambridge.

Klein P. and B. L. Hua (1988) Mesoscale heterogeneity of the wind-driven mixed layer: influence of a quasigeostrophic flow. *Journal of Marine Research*, **46**, 495–525.

Knudson C., W. S. Chamberlain and J. Marra (1989) Primary production and irradiance data for the U.S. JGOFS (leg 2) *Atlantis II* (Cruise 112.4). Technical Report LDGO-89.4, Lamont-Doherty Geological Observatory, Palisades, NY.

Lorenzen C. (1972) The extinction of light in the ocean by phytoplankton. *J. Cons. Int. Explor. Mer*. **34**, 262–267.

Marra J. and C. Ho (1993) Initiation of the spring bloom in the northeast Atlantic (47N, 20W): a numerical simulation. *Deep-Sea Research II*, **40**, 55–74.

Martin J., S. E. Fitzwater, R. M. Gordon, C. N. Hunter and S. J. Tanner (1993) Iron, primary production and carbon–nitrogen flux studies during the JGOFS North Atlantic Bloom Experiment. *Deep-Sea Research II*, **40**, 115–134.

McCarthy J. (1981) The kinetics of nutrient utilization. In *The physiological bases of phytoplankton ecology*, T. Platt, editor, pp. 211–233. *Canadian Bulletin of Fish and Aquatic Science*.

McCarthy J. and J. L. Nevins (1986) Utilization of nitrogen and phosphorous by primary producers in warm core ring 82-B following deep convective mixing. *Deep-Sea Research*, **33**, 1773–1788.

McGillicuddy D. (1993) *Mesoscale ocean dynamics and biological productivity*. PhD thesis, Harvard University, Cambridge, MA 02138.

McGillicuddy D., A. R. Robinson and J. J. McCarthy (1995) Coupled physical and biological modeling of the spring bloom in the North Atlantic (II): three dimensional bloom and post-bloom effects. *Deep-Sea Research*, this issue.

Mullin M. M., E. F. Stewart and F. J. Fuglister (1975) Ingestion by planktonic grazers as a function of concentration of food. *Limmology and Oceanography*, **20**, 259–262.

Parsons T., M. Takahashi and B. Hargrave (1984) *Biological oceanographic processes*. Pergammon Press, New York.

Platt T., C. L. Gallegos and W. G. Harrison (1980) Photoinhibition of photosynthesis in natural assemblages of marine phytoplankton. *Journal of Marine Research*, **38**, 687–701.

Press W., B. P. Flannery, S. A. Teukolsky and W. T. Vetterling (1986) *Numerical recipes*. Cambridge University Press, Cambridge.

Rhea W. and C. O. Davis (1990) Bio-Optical Profile Data Report: Joint Global Ocean Flux Study North Atlantic Bloom Experiment R.V. *Atlantis II* Leg 2 (25 April–10 May 1989). Technical report, Jet Propulsion Laboratory, Pasadena, CA.

Riley G. (1942) The relationship of vertical turbulence and spring diatom flowerings. *Journal of Marine Research*, **5**, 67–87.

Robinson A. (1993) *Physical processes, field estimation and interdisciplinary ocean modeling*. Reports in Meteorology and Oceanography. Harvard University, Cambridge, MA.

Robinson A., D. J. McGillicuddy, J. Calman, H. W. Ducklow, M. J. R. Fasham, F. E. Hoge, W. G. Leslie, J. J. McCarthy, S. Podewski, D. L. Porter, G. Saure and J. A. Yoder (1993) Mesoscale and upper ocean variabilities during the 1989 JGOFS bloom study. *Deep-Sea Research II*, **40**, 9–35.

Slagle R. and G. Heimerdinger (1991) U.S. Joint Global Ocean Flux Study North Atlantic Bloom Experiment Data Report, April–July 1989. WHOI/JGOFS Process Study Data Report P-1.

Steele J. (1974) Spatial heterogeneity and population stability. *Nature*, **248**, 83.

Steele J. and E. W. Henderson (1981) A simple plankton model. *The American Naturalist*, **117**, 676–691.

Steele J. and M. M. Mullin (1977) Zooplankton dynamics. In *The sea*, E. Goldberg, editor, John Wiley and Sons, New York, pp. 857–890.

Stevenson J. (1983) The seasonal variation of the surface mixed layer response to the vertical motions of linear Rossby waves. *Journal of Physical Oceanography*, **13**, 1255–1268.

Sverdrup H. (1953) On conditions for the vernal blooming of phytoplankton. *J. Cons. Explor. Mer*. **18**, 287–295.

Syrett P. (1981) Nitrogen metabolism of microalgae. In *The physiological bases of phytoplankton ecology*, T. Platt, editor, pp. 182–210. *Canadian Bulletin of Fish and Aquatic Science*.

Wada E. and A. Hittori (1971) Nitrate metabolism on the euphotic layer of the central North Pacific Ocean. *Limnology and Oceanography*, **16**, 766–772.

Walstad L. and A. R. Robinson (1993) A coupled Surface Boundary Layer–Quasigeostrophic Model. *Dynamics of Atmospheres and Oceans*, **18**, 151–207.

Ward B. (1987) Nitrogen transformations in the Southern California Bight. *Deep-Sea Research*, **34**, 785–805.

Ward B. and O. C. Zafiriou (1988) Nitrification and nitric oxide in the oxygen minimum of the eastern tropical North Pacific. *Deep-Sea Research*, **35**, 1127–1142.

Ward B., K. A. Kilpatrick, E. H. Renger and R. W. Eppley (1989) Biological nitrogen cycling in the nitracline. *Limnology and Oceanography*, **34**, 493–513.

Wheeler P. and S. A. Kokkinakis (1990) Ammonium recycling limits nitrate use in the oceanic subarctic Pacific. *Limnology and Oceanography*, **35**, 1267–1278.

Woods J. (1988) Mesoscale upwelling and primary production. In *Toward a theory on biological–physical interactions in the world ocean*, B. Rothschild, editor, D. Reidel, Dordrecht.

Wroblewski J. (1977) A model of phytoplankton plume formation during variable Oregon upwelling. *Journal of Marine Research*, **35**, 357–394.

Pergamon

0967-0637(95)00035-6

*Deep-Sea Research I*, Vol. 42, No. 8, pp. 1359–1398, 1995

0967-0637/95 $9.50 + 0.00

# Coupled physical and biological modelling of the spring bloom in the North Atlantic (II): three dimensional bloom and post-bloom processes

D. J. McGILLICUDDY Jr,* A. R. ROBINSON* and J. J. McCARTHY*

(*Received* 31 *March* 1994, *in revised form* 9 *September* 1994, *accepted* 12 *January* 1995)

**Abstract**—A set of three dimensional coupled physical and biological models is used to ascertain the importance of mesoscale dynamical activity during the 1989 JGOFS North Atlantic Bloom Experiment. First, various physical processes causing nutrient flux are studied with a simplified one compartment "nutrient model" utilized in an isolated vortex. A hierarchy of vertical transport processes is described for this case, ranging from the relatively minor fluxes caused by vortex stretching in the interior to the moderate transport resulting from the interaction of the interior and wind driven motions to the rather vigorous (3 m per day) effective transport caused by the propagation of the vortex. With these flux mechanisms in hand, the tuned four compartment biological model described in Part 1 is used to simulate the Small eddy in isolation. Together the propagation flux and the lifting of density surfaces caused by vortex evolution result in a twofold increase in mixed layer nitrate over that predicted by a one dimensional model. Enhanced phytoplankton and heterotroph production is associated with the elevated nutrient concentrations. Finally the three eddy configuration observed during the experiment is simulated. While all the previous vertical transports are active in this case, they are overshadowed by intense vertical motions associated with eddy–eddy interactions. Nutrient enhancements of up to an order of magnitude occur in the simulations that substantially increase both plant and animal production in localized regions for periods of weeks.

## 1. INTRODUCTION

Physical, biological and chemical properties of the open ocean vary a great deal on many spatial and temporal scales. In order to understand the observed distributions it is necessary to deal realistically and explicitly with the mechanisms responsible for this variability. In general this requires that the dynamical evolution of four dimensional oceanic fields be understood; it is essential to view observations in their spatial and temporal context. Interdisciplinary model systems are a natural media for such analysis. The assimilation of data forces the model to agree with observations to within prescribed error bounds, while providing space–time continuous fields consistent with the model dynamics. The resulting optimal field estimates serve as an ideal framework for process investigations. This approach has been used in the present study and a companion paper (McGillicuddy *et al.*, 1995) (hereafter MMR95) to examine the 1989 JGOFS North Atlantic Bloom data set.

*Department of Earth and Planetary Sciences, Harvard University, Cambridge, MA 02138, U.S.A.; present address: Woods Hole Oceanographic Institution, Woods Hole, MA 02543, U.S.A.

The fact that open ocean phytoplankton live in a highly dynamic environment shapes their ecology in two basic ways. First, ocean circulation can affect primary productivity by modulating *in situ* growth rates. Second, the distribution of biogenic material is continually deformed and rearranged through transport and advective processes. Let us begin with the rates of local production. In the open ocean, the growth of phytoplankton is limited primarily by either light or the availability of inorganic nutrients (most notably nitrogen). Thus, any physical process that affects the concentration of nutrient in or the solar radiation incident upon a water parcel can potentially influence the rate of photosynthesis within it.

In general, the fluid medium in which open ocean phytoplankton are immersed can be broken down into two distinct, yet interconnected, physical regimes. Typically there is a vertically well mixed surface layer of tens to sometimes hundreds of meters where the physical, biological and chemical constituents are homogeneously distributed by turbulent processes. Below this layer lie deep oceanic flow fields that are dominated by mesoscale motions with characteristic lateral extents of tens to hundreds of kilometers and time scales of several days to months. The currents, fronts and eddies that make up these deep fields are approximately in geostrophic balance and their dynamics are governed by the conservation of potential vorticity.

Both of these regimes contain a variety of mechanisms capable of regulating growth rates. In the surface boundary layer, vertical mixing from either direct wind forcing or buoyant convection can act to entrain nutrients from below into the often nutrient depleted near surface region. The extent of vertical mixing also influences the amount of the light that phytoplankton are exposed to. Sverdrup's (1953) conceptual model of a light limited phytoplankton population is useful in understanding some aspects of this issue. He noted the existence of a critical mixing depth at which the average light intensity was just sufficient to compensate for integrated respiratory losses. Only when the depth of mixing is shallower than the critical depth can the population sustain net growth. Thus, the vertical extent of the mixed layer in relation to the ambient light field is of crucial importance.

Mesoscale flows influence primary productivity primarily through their effect on nutrient availability. Vertical perturbations of the density surfaces in the main thermocline associated with mesoscale currents often extend into the upper ocean and increase or decrease nutrient concentrations accordingly. The dynamics of these features can produce vertical motions that transport nutrients into the euphotic zone. For example, it has been shown that the relaxation of the depressed density surfaces of an anticyclonic vortex during frictional decay can cause upwelling sufficient to produce a measurable increase in plant biomass in the interior of the feature (Nelson *et al.*, 1989; Franks *et al.*, 1986). The vorticity dynamics of mesoscale flows can also induce significant vertical velocity through the process of vortex stretching. Woods (1988) has proposed this as the main mechanism by which ocean eddies influence primary productivity. Conservation of potential vorticity demands that local changes in relative vorticity be balanced by adjustment of the depth of a fluid layer, therefore resulting in either upwelling or downwelling. Mesoscale dynamical processes, such as the meandering of a thin jet, produce submesoscale "hotspots" of locally intense vertical motion. Strass (1992) has analyzed high resolution vertical sections of density and chlorophyll in the North Atlantic and identified a peak in the variance spectrum of chlorophyll at approximately 10 km which appears consistent with biomass accumulations caused by submesoscale upwelling at fronts. These spatially and temporally intermittent events are phenomenologically distinct from submesoscale lenses. Results

from numerical models indicate rates of vertical motions ranging from several to tens of meters per day. A combination of observations and analysis in frontal regions has suggested vertical velocities as high as 40 m per day (Pollard and Regier, 1992) arise from ageostrophic advections of the vorticity field.

Surface boundary layer and interior processes are not only relevant to primary production in their own right; the interaction between the two can also play an important role in determining the growth rate of phytoplankton. Klein and Hua (1988) showed how the combination of the wind driven and mesoscale flows can result in significant heterogeneity in the mixing layer depth field. The interaction between the deep ocean and the surface boundary layer can also induce significant vertical transport. Stevenson (1980) showed how the advection of the interior vorticity field by the wind driven surface current can result in vortex stretching comparable in magnitude to that caused by the interior dynamics alone.

Clearly, then, there is a wealth of physical processes that can strongly influence local rates of primary production. However, in order to understand fully the spatial and temporal variability of observed biological parameters, it is necessary to consider these processes as occurring within a dynamic fluid medium. Ocean currents continually rearrange biological fields of interest by advection, often resulting in complex and convoluted structures. The flow can transport biogenic material over considerable distances to regions quite different in nature from their area of formation (Angel and Fasham, 1983).

Coupled three dimensional physical and biological models have thus become an important tool in the analysis of biogeochemical variability. Sarmiento *et al.* (1993) have embedded Fasham *et al.*'s (1990) upper ocean ecosystem into a model of the North Atlantic general circulation. This approach facilitates the study of basin scale patterns of nitrogen cycling and plankton dynamics, but leaves mesoscale variability unresolved. Flierl and Davis (1993) have developed process oriented models capable of simulating the effects of mesoscale motions on biological and chemical distributions and have applied them in the Gulf Stream region. Using a contour dynamics method to simulate a quasigeostrophic thin jet with a simple mixed layer model attached at the surface, the authors examine the effects of Gulf Stream meandering on a nutrient–phytoplankton–zooplankton ecosystem. Such an approach is quite useful for examining the basic processes by which the physics of the system affects biological distributions. However, direct comparisons with observations are made difficult by the idealized nature of the physical and biological formulation of the problem.

The main focus of the present effort is to make direct contact between models and data in the study of how mesoscale and upper ocean dynamics affect primary productivity and its variability. The approach is to incorporate biological components into regional numerical models of open ocean physics that are capable of producing realistic representations of oceanic flow fields. The ability to handle open boundary conditions in these physical models has made it possible to represent adequately very energetic mesoscale phenomena on the appropriate space and time scales (Robinson and Walstad, 1987; Robinson, 1993). Such models can be initialized with real ocean data and periodically updated via data assimilation to produce optimal four dimensional field estimates that are consistent with the available data and dynamically interpolated across data sparse regions. The resulting fields provide an ideal setting for the simulation of biogeochemical and ecosystem dynamics in that the structures and variabilities are representative of the real

ocean. This provides a framework for the investigation of coupled physical–biological processes that is firmly grounded in data.

In MMR95 such an interdisciplinary model system was introduced. It consists of a coupled quasigeostrophic and surface boundary layer physical model together with a four compartment (nitrate, phytoplankton, heterotroph and ammonium) nitrogen based biological model. A one dimensional implementation of the system was used to examine some aspects of the 1989 JGOFS North Atlantic Bloom data set. Two parallel simulations carried out inside and outside the Small eddy were shown to represent the general features of the two time series taken in these locations reasonably well. Thus, the model system has been tuned to the bloom data in one dimension. Although mesoscale *heterogeneity* was treated within the one dimensional framework, mesoscale *dynamical processes* were not. In this sense the tuning of the model is potentially incomplete; sources and sinks arising from mesoscale dynamical processes were not treated in the MMR95 one dimensional analysis. In this paper the full three dimensional physical–biological model will be used to study how mesoscale and upper ocean dynamical processes affect biological and chemical fields.

Because so many physical–biological processes are simultaneously active in complex models such as these, the behavior of the model can often be difficult to diagnose and understand. This analysis will therefore begin with the study of physical transport processes in a simplified "nutrient model". Nitrate is treated as a passive tracer in the three dimensional physical model and the net effect of biological processes is parameterized as instantaneous export of all nitrate that makes its way into the mixed layer. This exercise is useful in contrasting and quantifying the various physical mechanisms responsible for nutrient flux.

With these processes in hand the full biological model is then used to study mesoscale dynamical effects during and after the bloom. Surface fluxes derived from an operational atmospheric model are used to force the interdisciplinary model when shipboard observations are not available. This allows the simulations to be extended well into the "post-bloom" period. First, the Small eddy is studied in isolation and then the three eddy case is examined. Comparison with the one dimensional results is used to quantify the three dimensional effects.

## 2. THE INTERDISCIPLINARY MODEL SYSTEM

The coupled physical and biological models are described in detail in MMR95. The biological model is based on nitrogen and includes nitrate, phytoplankton, heterotroph and ammonium constituents. Phytoplankton growth is both light and nutrient limited, with ammonium being taken up preferentially. Heterotrophic consumption is based on the Ivlev grazing formulation. Nutrient regeneration to ammonium and export by heterotrophs includes both linear and quadratic terms to parameterize loss to higher trophic levels.

The biological quantities are incorporated as passive tracers in a coupled quasigeostrophic and surface boundary layer model. The evolution of a given scalar is given by the following equation for its interior and boundary layer components $\Phi$ and $\phi$, respectively:

$$\phi_t + \alpha(J(\psi^*, \phi) + \mu(\Phi_x + \phi_x) + \nu(\Phi_y + \phi_y) + (w^{QG} + \omega)\phi_z) - \omega\Phi_z + w_\phi(\phi_z + \Phi_z) = (M_\phi)_z + S_\phi$$

*Table 1. Run table for the nutrient model experiments*

| Run | Figure | MLD | $w$ | $\beta$ |
|---|---|---|---|---|
| 1 | 1a | P | I | 0 |
| 2 | 1b | P | F | 0 |
| 3 | 1c | B | F | 0 |
| 4 | 1d | P | F | 0.1244 |
| 5 | 1e | B | F | 0.1244 |
| 6 | 6a | R | 0 | 0 |
| 7 | 6b | R | F | 0 |
| 8 | 6c | R | F | 0.1244 |

The figure in which the horizontal maps of each simulation are displayed is indicated. In these runs the mixed layer depth (MLD) is either persisted (P), balanced (B), or varies in time with realistic forcing (R). The vertical velocity ($w$) is either zero (0), interior (I), or full (F). The meridional gradient of the Coriolis parameter is either zero (0) or its proper value for this latitude (0.1244).

Here $J(\psi^*,\phi)$ represents the advection of $\phi$ by the quasigeostrophic streamfunction $\psi^*$ and $\alpha$ is a nondimensional parameter. The wind driven velocity components $\mu$ and $\nu$ advect both interior and boundary layer quantities. Interior and boundary layer vertical velocities $w^{QG}$ and $\omega$ advect material vertically. Passive tracers can be assigned arbitrary sinking velocity $w_\varphi$. The right hand side of the above equation includes mixing terms $(M_\phi)_z$ and biological forcing functions $S_\varphi$ that represent the transfers between nitrogen constituents.

## 3. THE NUTRIENT MODEL

In order to examine in detail the physical processes of nutrient flux into the mixed layer, an idealized "nutrient model" was constructed. In this model, nutrients that are transported into the mixed layer are instantaneously exported. In a sense, this model parameterizes an upper ocean biological system that operates at infinite speed. This configuration maintains the maximum possible gradient between the mixed and remnant layers thus providing an upper boundary for the nutrient fluxes caused by transport processes that act on this gradient.

In this set of numerical experiments, various transport mechanisms are examined separately and then combined in a logical manner, building toward the most realistic case in which all of the processes are active. A summary of the simulations described below is shown in Table 1. Transports of three basic types are investigated: (1) those arising from vertical motions due to mesoscale flows and their interaction with the surface layer; (2) those due to $\beta$-induced propagation of features; and (3) those due to excursions of the mixed layer primarily caused by atmospheric forcing. First the mixed layer is persisted (held at a constant depth) in order to examine the relative efficacy of transports caused by interior vertical velocities and those generated by wind interactions (runs 1 and 2). Then the partitioning of the upward flux between that which is entrained into the mixed layer and that which is not is quantified by specifying a "balanced" mixed layer situation in which

a constant wind and compensating heat flux cause a constant mixed layer depth in the absence of eddy motions (run 3). In run 4, feature propagation is induced by turning on $\beta$ with a persisted mixed layer. The relative magnitude of the mesoscale dynamical vertical velocities and the propagation flux is quantified by comparison with run 2. The entrainment partitioning of the propagation flux is examined in run 5, which is the most realistic of the constant forcing experiments in that all eddy related transports are active. Runs 6–8 are used to compare the eddy transports to the nutrient flux due to excursions of the mixed layer caused by realistic atmospheric forcing.

The initial condition used in these experiments is a feature model representation of an isolated eddy characteristic of the Small eddy described in Robinson *et al.* (1993). The use of feature models facilitates the generation of full water column fields from limited data sets by using assumptions about the velocity structure of the features of interest. Estimates of the feature model parameters (eddy radii, swirl speeds and vertical shears) obtained by altimetric and *in situ* observations can therefore be used to analytically compute the streamfunction and vorticity fields required for initialization of the quasigeostrophic model. In the axisymmetric feature model employed here, the velocity increases linearly from the center out to a radius of maximum velocity, beyond which it decays exponentially. There is a linear shear in the vertical down to an assumed level of no motion at 2500 m. This vortex model was chosen to be consistent with both the present data and deeper historical data available in the region.

Horizontal boundary conditions in these and all other simulations discussed in this work are persisted. Each simulation is integrated for 37 days between day 115 and day 152.

### 3.1. *Run* 1: *persisted MLD, interior* w, $\beta = 0$

In the first experiment, the mixed layer is persisted at a constant depth and only the vertical velocity generated by the evolution of the interior is used to advect nitrate across the mixed layer depth interface. Figure 1a shows the alternating upwelling and downwelling regions that develop around the perimeter of the eddy as it evolves. This pattern of vertical velocity rotates cyclonically and is associated with the interior dynamics of the eddy as it develops slight asymmetries during the course of its evolution. The upwelling patches transport nitrate into the mixed layer which results in the export of nitrogen in a ring around the perimeter of the eddy. The width of the band is set by the radial extent of the upwelling patches. There is also noticeable deposition of nitrogen in the center of the eddy that results from a decrease in surface density caused by adjustment of the interior. A time series of the spatially averaged nitrogen export is shown in Fig. 2, curve (a).

### 3.2. *Run* 2: *persisted MLD, full* w, $\beta = 0$

Next the effect of a wind generated surface vertical velocity is examined. The mixed layer is still persisted, but the vertical velocity is now made up of two contributions: one from the eddy interior dynamics described above, and one that arises from the interaction of the wind driven and interior flows. In this run a westerly wind causes Ekman transport toward the south. This flow redistributes the vorticity field through advection of the interior vorticity by the boundary layer velocity. Conservation of potential vorticity requires that the water column stretch (causing upwelling) in areas where vorticity is

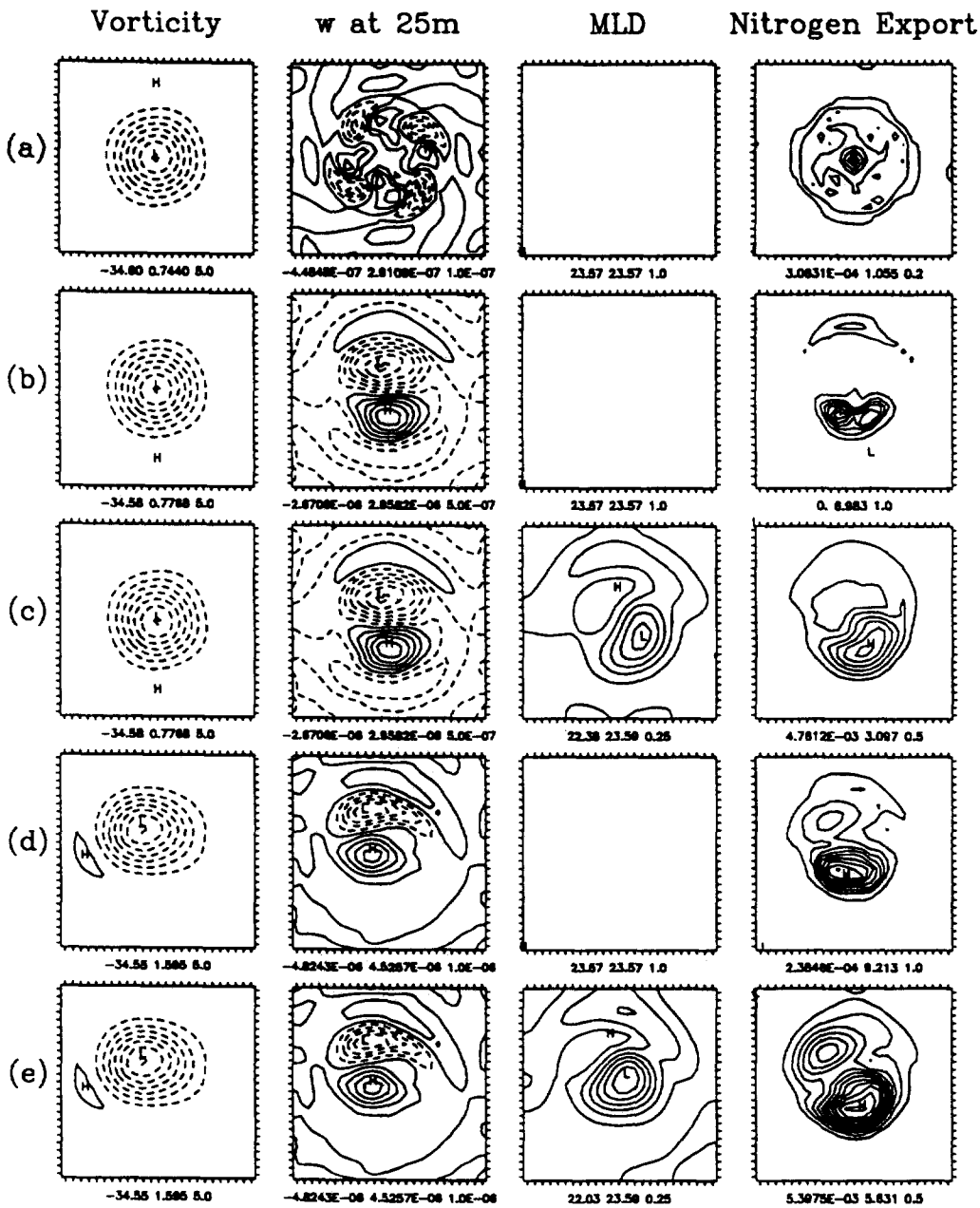


Fig. 1. Maps of vorticity at 50 m (nondimensional), vertical velocity at 25 m (m/s), mixed layer depth (m) and integrated nitrogen export ($[g/cm^2]/8.4 \times 10^{-2}$) after 37 days of integration for runs 1–5 (A–E) listed in Table 1. The locations of the highest and lowest values in each field are denoted by H and L respectively. Positive contours are solid and negative contours are dashed. The minimum, maximum and contour interval are indicated below the map from left to right. These conventions are used in all the following contour maps except where noted.

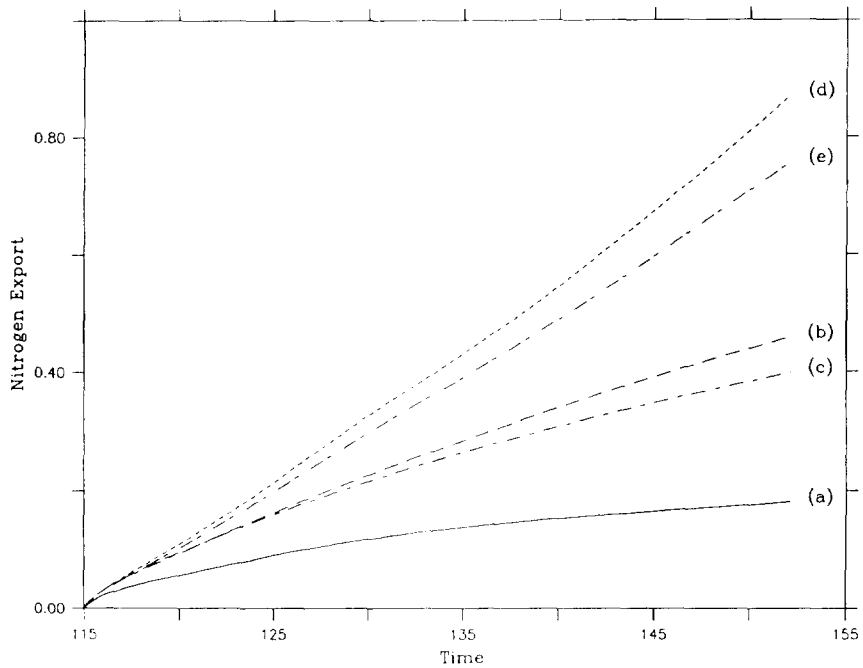


Fig. 2. Spatially averaged nitrogen export ($[g/cm^2]/8.4 \times 10^{-2}$) for the five simulations shown in Fig. 1.

decreasing (the southern flank of the eddy), and compress (causing downwelling) where vorticity is increasing (the northern flank of the eddy). Viewed differently, the advection of the interior velocity by the Ekman velocity causes convergence in the northern part of the eddy and divergence in the southern part. The vertical motions due to this interaction are much larger than those caused by the eddy interior dynamics alone and therefore overshadow the structure of vertical velocity seen in the previous run (Fig. 1b). The more vigorous vertical transport significantly increases the flux of nitrate into the mixed layer, resulting in a much larger accumulation of exported nitrogen (Fig. 2, curve (b)). As expected the region of largest nitrogen export occurs directly underneath the region of upwelling (Fig. 1b).

### 3.3. *Run* 3: *balanced MLD, full* w, $\beta = 0$

In the next simulation the assumption of a constant mixed layer depth is relaxed. We now use the full mixed layer equation in which there is a three way balance between horizontal advection, vertical advection and entrainment. For comparison with the previous case, the model is forced with the same wind as before, but now positive surface heat flux has been added in order to maintain a finite mixed layer depth. The momentum and heat fluxes balance each other so that the basic state mixed layer is constant. That is, in the absence of any eddy motions the mixed layer depth is uniform and stationary. The surface fluxes were chosen so that the basic state mixed layer resides at the same depth as in

the previous simulations. After 37 days of integration, the mixed layer depth field has stayed approximately constant at the basic state depth over most of the domain except for an area in the southeastern section of the eddy in which it has shoaled (Fig. 1c). The shoaling of the mixed layer in this region is caused by the combination of the upwelling in the southern flank of the eddy pushing the mixed layer toward the surface and the advection of this disturbance by the cyclonic flow of the interior. This behavior reveals a very clear asymmetry in the mixed layer response to vertical motions. In the case of upwelling, there is a partitioning of the upward flux between that which pushes the mixed layer depth upwards and that which is actually entrained into the mixed layer. In the case of downwelling (as occurs in the northern half of the eddy), the vertical velocity causes detrainment of mixed layer fluid. The mixed layer does not descend because the balancing heat and momentum fluxes set the depth of the maximum mixed layer depth, which is coincident with the basic state mixed layer depth. The increase in mixed layer buoyancy with time stratifies the water column, so that the detrained fluid is of lesser buoyancy than the mixed layer, thus preventing deepening of the mixed layer.

The nitrate flux into the mixed layer is decreased with respect to the previous case in which the vertical velocity was used to advect material across an artificially persisted mixed layer depth (Fig. 2, curve (c)). In this simulation, the upward motion pushes the mixed layer toward the surface, and only a portion of the total flux is entrained into the mixed layer. While the bulk of the exported nitrogen accumulates directly below the region of upwelling, there is a significant displacement of the northeastern boundary of the high export region in the direction of the interior flow (Fig. 1c). This results from the entrainment of fluid in the area of shoaled mixed layer depth which has been cyclonically advected by the interior flow. The entrainment occurs where the mixed layer descends toward the basic state depth once it has been advected away from the upwelling region.

It is important to note here that the asymmetry in the mixed layer depth response to vertical motions of opposite sign in this experiment is not common to all types of mixed layer models. For example, simulations carried out with the model of Price *et al.* (1986) show that under similar forcing conditions, the mixed layer depth response is more symmetric. That is, upwelling causes the mixed layer to shoal (as in the present model) and downwelling causes it to deepen (unlike the present model). This symmetry is a result of the different mixing parameterization used in this so called "dynamic instability model" in which mixing is dependent on Richardson number criteria instead of the turbulent kinetic energy budget used in the present model. Therefore the results presented here are to some extent dependent on the particular type of mixed layer model that is being used. However, the primary focus of these experiments is to understand the mechanisms of nutrient injection into the mixed layer (i.e. the upwelling case). In this regime, the response of the two types of mixed layer models is quite similar.

### 3.4. *Run* 4: *persisted MLD, full* w, $\beta \neq 0$

In all of the previous experiments the parameter $\beta$ was set to zero so that vertical transport processes could be studied in a stationary eddy. Setting the meridional gradient of the Coriolis parameter to its proper value for this latitude causes the eddy to propagate to the northwest. The pattern of exported nitrogen is similar to the corresponding $\beta = 0$ case (run 2) in that there is accumulation underneath the upwelling region (Fig. 1d). However, in this simulation there is significant export along the northwestern border of the

eddy. Figure 3 shows the instantaneous nitrate flux into the mixed layer on day 151 overlaid on the vorticity field. The transport taking place on the leading edge (with respect to the direction of propagation) of the eddy overshadows the flux caused by the wind driven upwelling. In fact, the integrated nitrogen export on day 151 is approximately twice that of the nonpropagating case (Fig. 2, curve (d)).

This is a simple transport mechanism that can be interpreted as the "propagation flux". Consider the propagating disturbance schematized in Fig. 4. At time $t_1$ a given nutrient surface is domed upward in a cyclonic vortex so that it penetrates the mixed layer. Biological processes remove this excess nitrate and if the eddy remains at rest there will be no further nutrient supply. This is not necessarily the case when the feature is moving. If the propagation is purely linear, a point (a) at time $t_1$ will rise to point (c) at time $t_2$ resulting in an injection of nutrient along the leading edge of the disturbance. If the propagation is purely nonlinear and the vortex moves along as a coherent structure, a point (a) at time $t_1$ will simply translate to point (b) at time $t_2$; in this case there is no flux into the mixed layer. The efficacy of this mechanism therefore lies in the level of nonlinearity in the oceanic flow of interest. In the linear case, analytic estimation of the flux is straightforward. The slope of the nitrate surfaces at the base of the mixed layer is approximately 1 part in 500 (Fig. 5). Multiplying this slope by the observed propagation speed of 1.5 km per day gives an effective vertical velocity of 3 m per day. The flux is simply the product of the vertical velocity and the nitrate gradient at the base of the mixed layer. The maximum instantaneous nitrate flux in the simulation (Fig. 4) is nearly identical to this flux estimate, indicating the propagation of the vortex is mostly linear.

### 3.5. *Run* 5: *balanced MLD, full* w, $\beta \neq 0$

In this most realistic of all of the constant forcing experiments all of the previously mentioned transport mechanisms are active in the balanced mixed layer configuration. The resulting nitrogen export (Fig. 1e) is made up of patterns observed in the preceding runs. The integrated export (Fig. 2, curve (e)) is somewhat less than in run 4 because of the partitioning of the upward flux. This causes a relative decrease in the export due to wind driven upwelling, accentuating the propagation flux on the leading edge of the vortex.

### 3.6. *Run* 6: *realistic forcing*, $w = 0, \beta = 0$

In the remaining three runs the model is forced with time varying atmospheric fluxes derived from shipboard meteorological observations. In the first case (run 6) both the vertical velocity and $\beta$ are artificially set to zero in order to provide a benchmark for the flux that results from large scale excursions of the mixed layer. The pattern of exported nitrogen (Fig. 6a) is an image of the initial nitrate distribution as the mixed layer has captured material from the uplifted density surfaces inside the vortex in its numerous descents into the remnant layer. The time series of nitrogen export (Fig. 7, curve (a)) reveals that the largest flux of nitrate occurs right in the beginning of the simulation as the mixed layer deepens from its initial depth of 23 m to nearly 60 m. The next largest flux happens just a few days later as the mixed layer reaches its deepest point of the simulation, just below 60 m. Because the nutrient model removes all of the nitrate from this depth interval at this time, subsequent nutrient fluxes are much smaller. In fact, the only avenue for further nutrient capture is for the mixed layer to shoal, allowing nitrate to diffuse

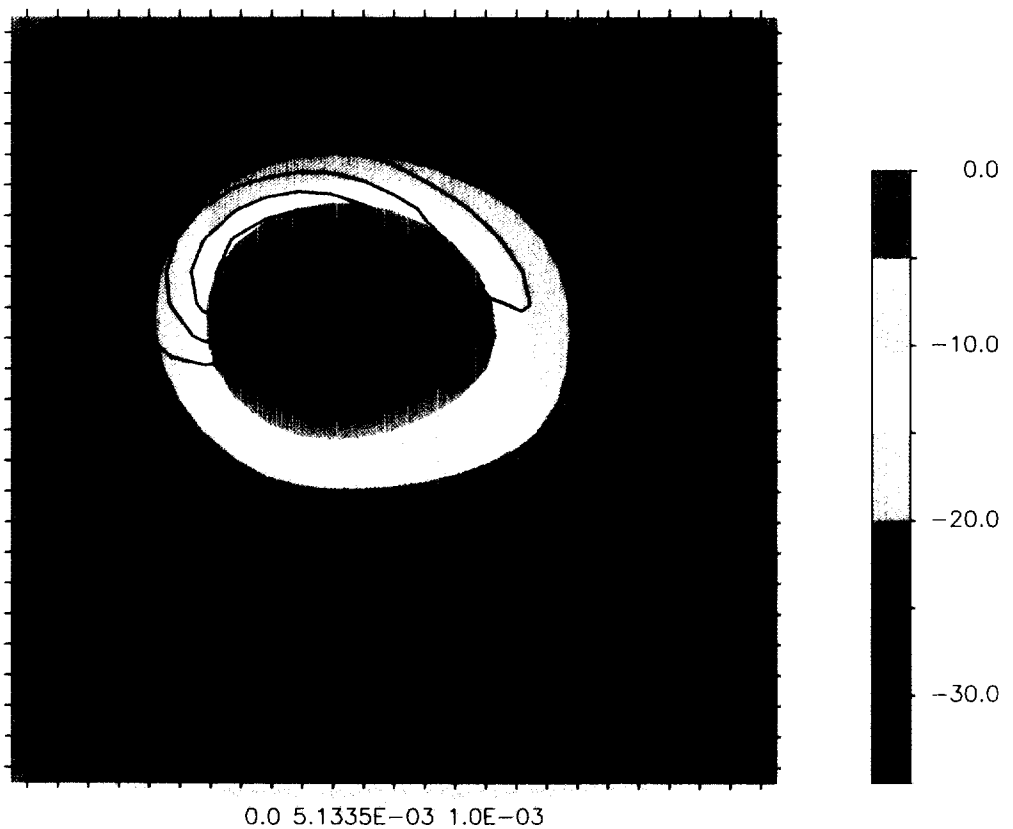


Fig. 3. Instantaneous nitrate flux into the mixed layer (units of 5.3 g/m$^2$/d) contoured over the 50 m vorticity field. The color bar shows the shading of the vorticity field in nondimensional units.

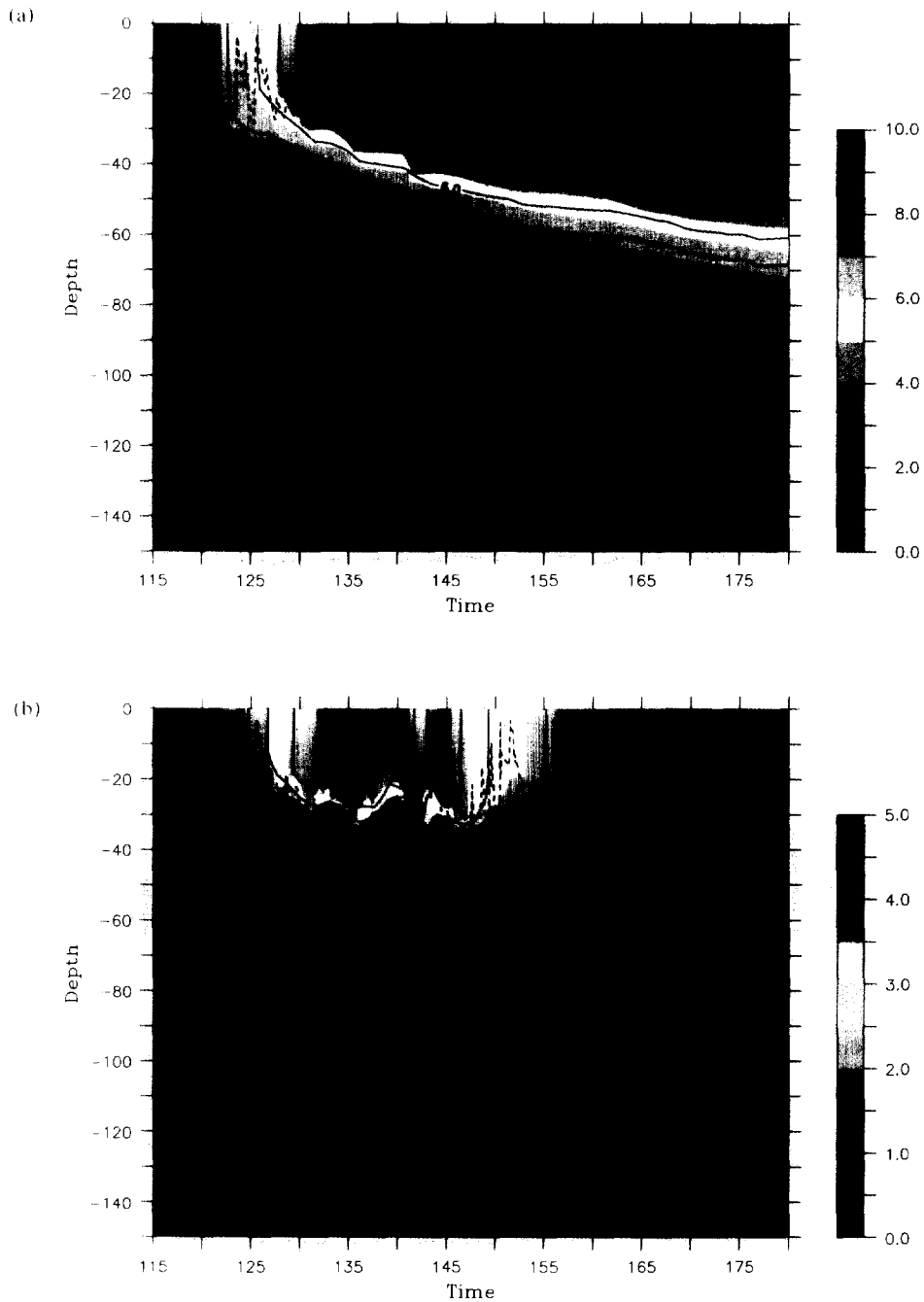


Fig. 18. Comparison of time series of the one dimensional model solution (shaded) with the three dimensional model solution (overlaid contours) inside the Small eddy: (a) nitrate, (b) phytoplankton, (c) heterotrophs and (d) ammonium. The one dimensional simulation shows more structure in time as the temporal resolution of the one dimensional record is 0.5 days, while that of the three dimensional record is 1.5 days. The dashed line shows the mixed layer depth.

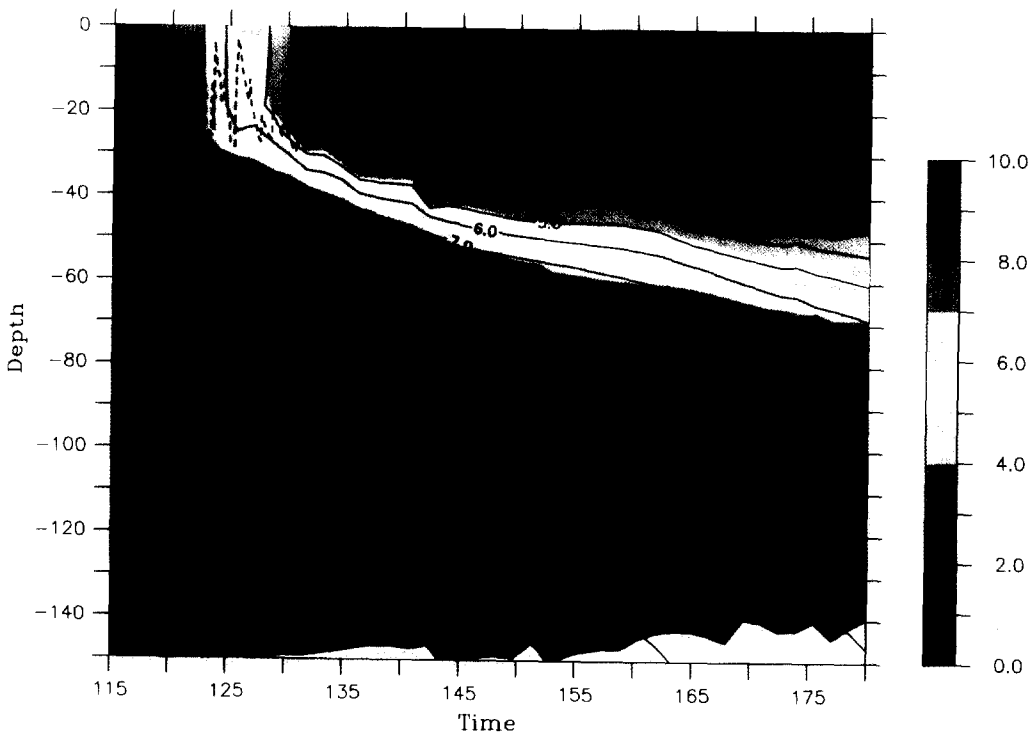


Fig. 25. Comparison of time series of the mixed layer nitrate concentration inside the Small eddy in the isolated case (shaded) and the three eddy case (overlaid contours). The dashed line shows the mixed layer depth.

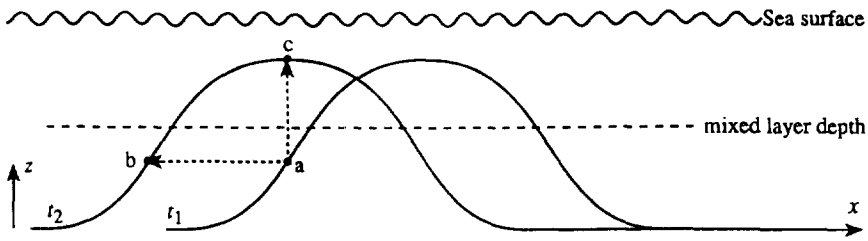


Fig. 4. A schematic representation of the propagation flux mechanism, showing an uplifted nitrate surface in a cyclonic vortex at times $t_1$ and $t_2$.

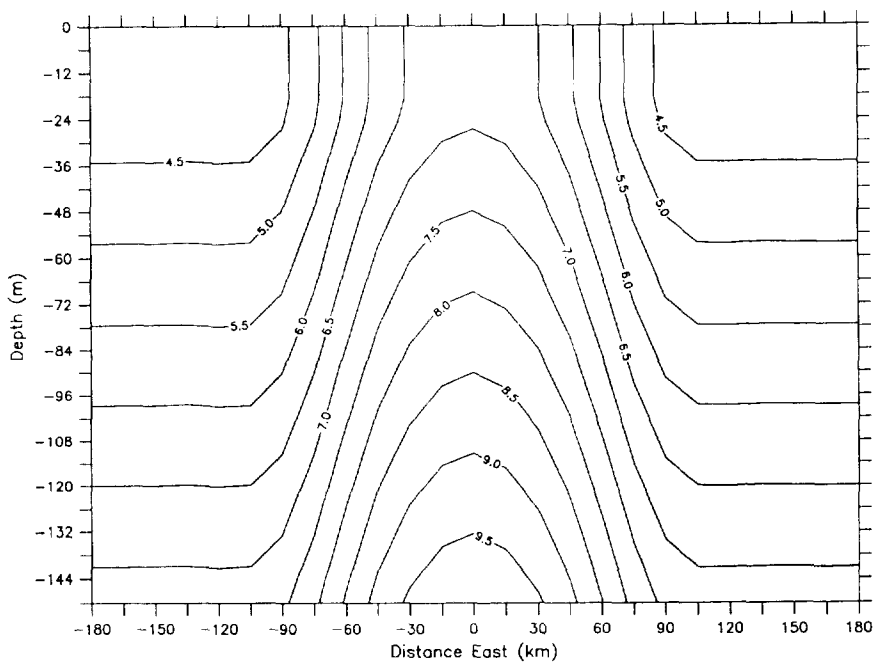


Fig. 5. A vertical section of the initial nitrate distribution across the Small eddy ($\mu$M).

upward in the remnant layer. Only then can the mixed layer scavenge additional nutrient from the remnant layer as it deepens.

This behavior demonstrates how the nutrient model exaggerates the nitrate flux in the realistic forcing experiments much more than in the constant forcing cases. Rapid deepening of the mixed layer in convective or wind driven events does create effective vertical velocities much larger than those generated by eddy effects, causing substantial flux into the mixed layer. However, these deepening events are followed by shoaling events in which large detrainment fluxes occur. In the nutrient model, the flux of nitrate from the mixed layer to the remnant layer is identically zero as the mixed layer shoals because nitrate is *instantaneously* removed from the mixed layer. This is of course not the case in the real ocean because biological removal processes take time. When the mixed

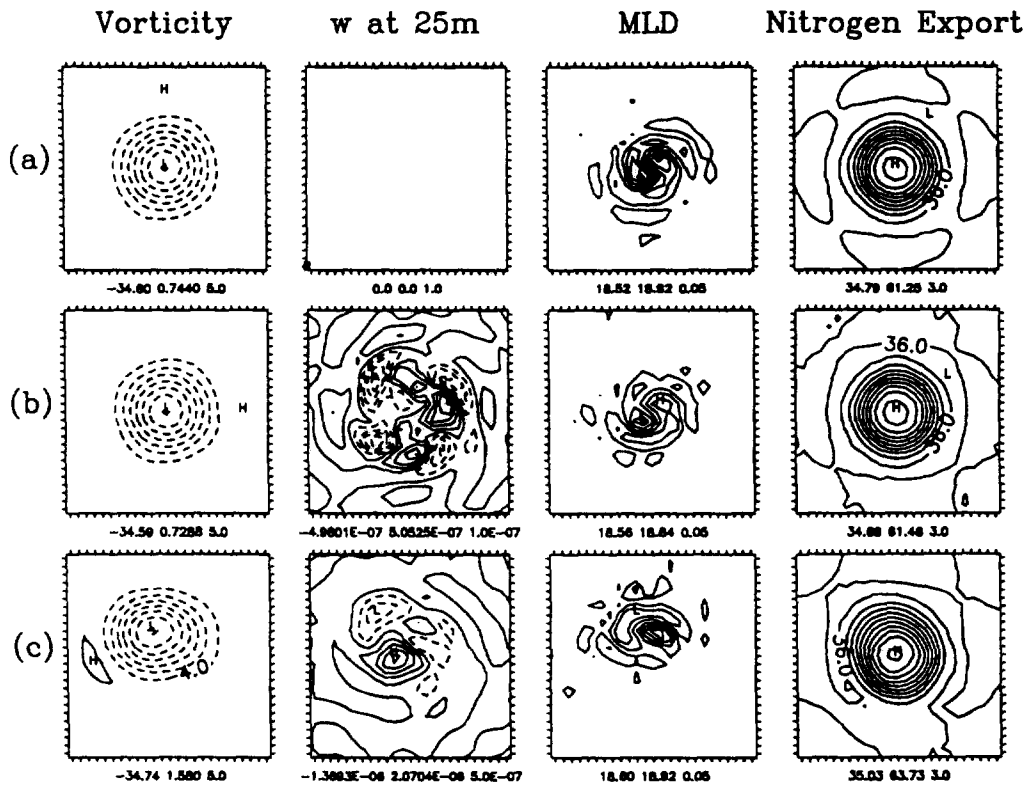


Fig. 6. Vorticity at 50 m (nondimensional), vertical velocity at 25 m (m/s), mixed layer depth (m) and integrated nitrogen export ([g/cm$^2$]/8.4 × 10$^{-2}$) on day 152 for runs 6–8 (a–c) listed in Table 1.

layer shoals after a deepening event, the unused nitrate is detrained and remains available for entrainment during subsequent deepening events. This process is not represented in the nutrient model.

### 3.7. *Run* 7: *realistic forcing*, $w \neq 0, \beta = 0$

Activating the full vertical velocity changes the overall solution very little, as the problem is dominated by the one dimensional transport processes. Figure 6b shows that the pattern of nitrogen export is nearly identical to the previous case. The amount of export is only slightly enhanced by the wind driven and eddy induced upwelling; the integrated export curve in Fig. 7, curve (b), is almost coincident with that of run 6.

### 3.8. *Run* 8: *realistic forcing*, $w \neq 0, \beta \neq 0$

Allowing the vortex to propagate also makes little difference in the solution (Fig. 6c). The propagation flux makes the integrated export distinguishably larger than the previous two cases, but the difference is quite small (Fig. 7, curve (c)).

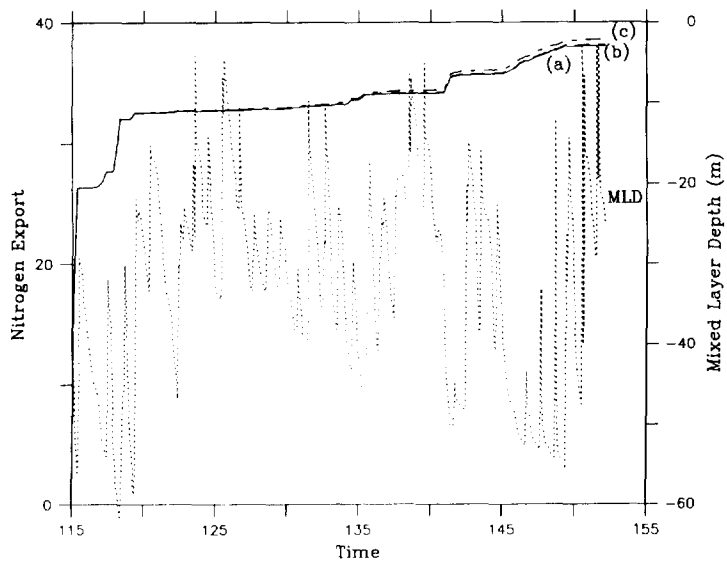


Fig. 7. Spatially averaged nitrogen export ([g/cm$^2$]/8.4 × 10$^{-2}$) for the three simulations shown in Fig. 6. Run 6 (curve a) is the solid line, run 7 (curve b) is a dashed line that is nearly coincident with (a), and run 8 (curve c) is the variable dashed line. The mixed layer depth is shown as a dotted line.

## 4. THREE DIMENSIONAL BLOOM SIMULATION: FORCING

Having examined nutrient flux processes in idealized numerical experiments, we now move on to more realistic simulations using the full interdisciplinary model. The physical model is forced with the observed winds and heat fluxes inferred from shipboard meteorological measurements during the time period in which they are available. It is of interest here to carry the simulations out further in time as the eddy effects become more pronounced after the transition to oligotrophy which takes place at the very end of the data set. For this purpose meteorological quantities for the region are extracted from the twice daily output from the European Center for Medium Range Weather Forecasting (ECMWF) atmospheric general circulation model. To verify the accuracy of the ECMWF fields for this region, model output was compared to the shipboard measurements for the period between days 115–151 (Fig. 8). Note that the temporal coverage of the shipboard records has been expanded beyond that reported in Robinson *et al.* (1993) with the recovery of additional data originally thought to have been lost. The wind speed records (Fig. 8a) agree extremely well except for three periods on or around days 121, 124 and 134 in which the ECMWF wind is significantly stronger than that observed. The wind direction is also represented quite well by the ECMWF model (Fig. 8b). Of course the observations show much more variability than the GCM can resolve, but the main features of the record are well reproduced. The surface heat flux inferred from the ECMWF fields also compares well (Fig. 8c). Except for during the storm on day 142 the heat fluxes computed from the two sources are quite similar. These heat flux calculations depend very much on the air–sea temperature gradient. During the period in which the ships were at sea, observed sea surface temperature is used in the heat flux computation. Beyond day 151 no sea surface temperature measurements are available so the model temperature is used.

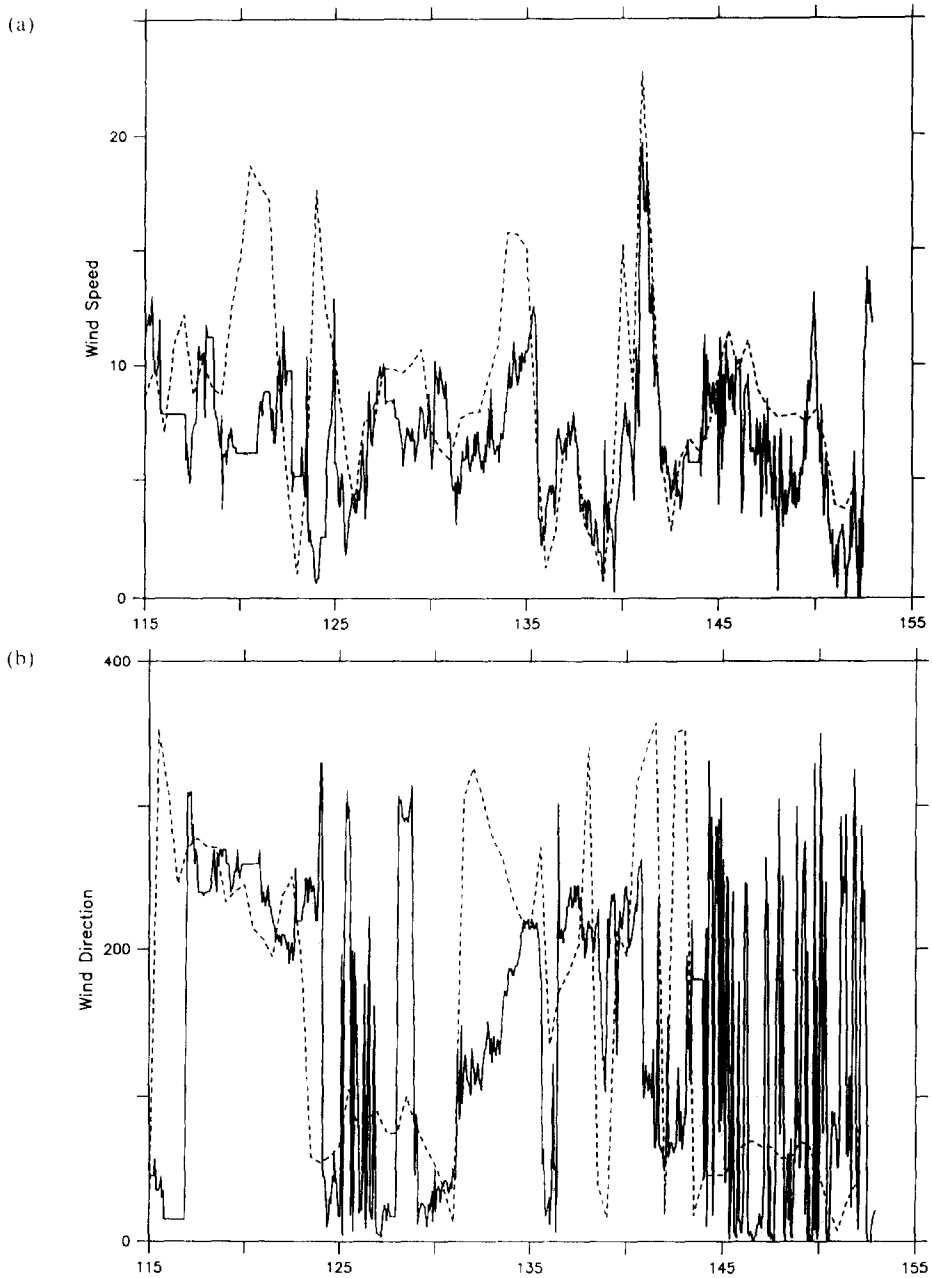


Fig. 8.

The flux of shortwave solar radiation is also needed for the later period for which there is no data. The radiation incident on the sea surface for a clear sky is directly calculable using standard algorithms (List, 1951). Because no observations of cloud cover are available after the ships left the area, their attenuation of the short wave flux must be estimated.

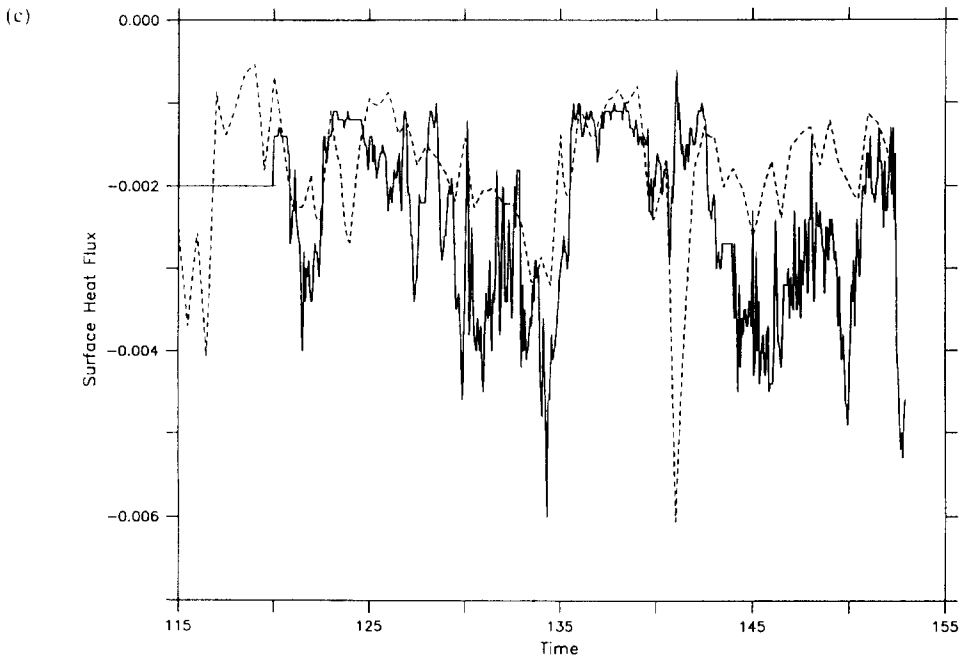


Fig. 8. Comparison of observations (solid line) with twice daily predictions from the ECMWF model (dashed line) for (a) wind speed (m/s) and (b) wind direction (degrees true). Panel (c) shows a comparison of the surface heat flux (cal/cm$^2$) estimated from shipboard meteorological observations (solid line) with those estimated from twice daily predictions of atmospheric conditions from the ECMWF model and sea surface temperature from the coupled quasigeostrophic and surface boundary layer model (dashed line). The heat flux estimated from the shipboard measurements is constant for the first five days because of missing values.

Historical data on cloud cover for the region indicate that cloud cover changes little over the two month period between days 115–180 (Miller, 1971). It is therefore reasonable to use the same effective cloud cover for days 151–180 as was present during days 115–151. To estimate the effective attenuation a simple ratio between the mean observed irradiance at the sea surface and the clear sky model prediction is computed for the period.

The combined records of observed and computed fluxes used to force the model in these simulations is shown in Fig. 9.

## 5. THREE DIMENSIONAL BLOOM SIMULATION: THE SMALL EDDY

In this experiment the bloom is simulated in a 360 km$^2$ domain with the Small eddy in isolation. The central biological parameter set described in the one dimensional model tuning experiments in MMR95 is used. The model is initialized on Day 115 with an axisymmetric feature model representation of the Small eddy (Fig. 10). The surface geostrophic velocity in the eddy increases linearly to 25 cm/s at a radius of 70 km beyond which it decays exponentially. There is linear shear in the vertical down to a level of no motion at 2500 m. The vorticity distribution shown in Fig. 10 consists of contributions from both the relative and thermal vorticity of the eddy. In this situation the thermal vorticity

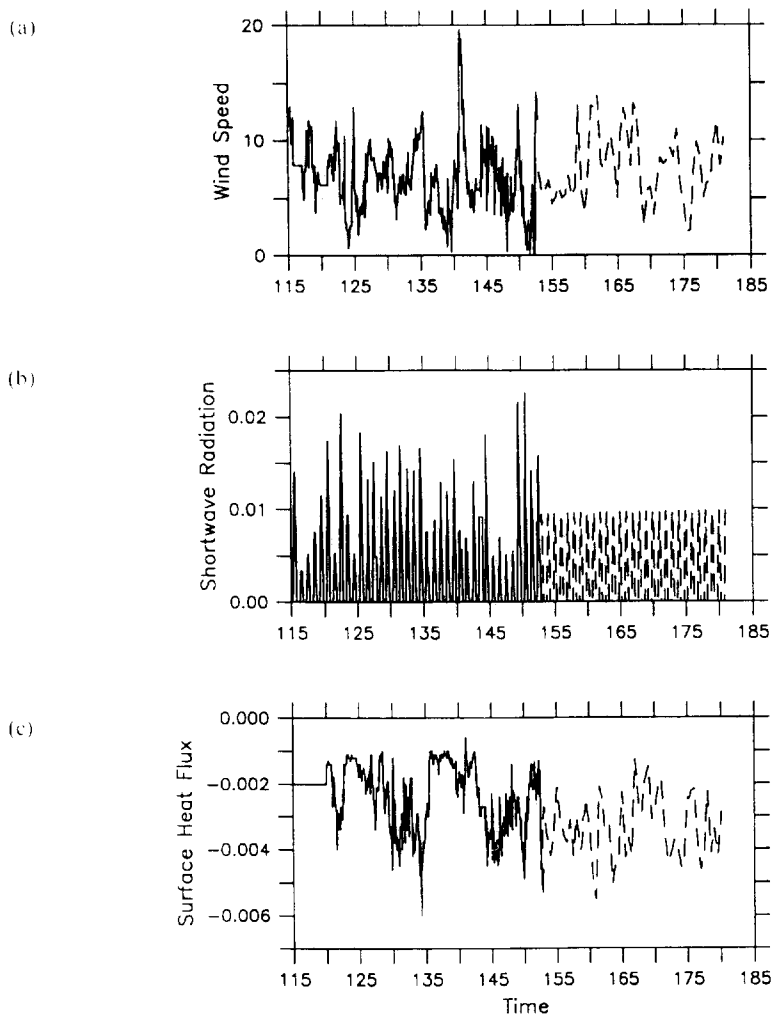


Fig. 9. Time series of surface fluxes used to force the physical model: (a) wind speed (m/s), (b) shortwave radiation (cal/cm$^2$) and (c) surface heat flux (cal/cm$^2$). Solid lines are used where shipboard meteorological observations are available and dashed lines are used where the quantities are estimated from model output (see text).

signal overshadows the relative vorticity so that the total vorticity inside this cyclonic feature is negative. This initialization is a result of careful tuning of the model to the available data and thus represents an improvement to the initial conditions used in Robinson *et al.* (1993) in which the sign of the vorticity perturbations caused by the three eddies was positive. The vertical velocity is identically zero in the initial condition, and the top density pattern mimics the vorticity distribution. The biological model initial conditions (Fig. 11) consist of constant values for phytoplankton, heterotrophs and ammonium. Nitrate is initialized from the observed nitrate versus sigma–*t* relationship. See MMR95 for a more detailed description of the biological initial conditions.

After 36 days of integration (Day 151), the eddy has propagated approximately 54 km to

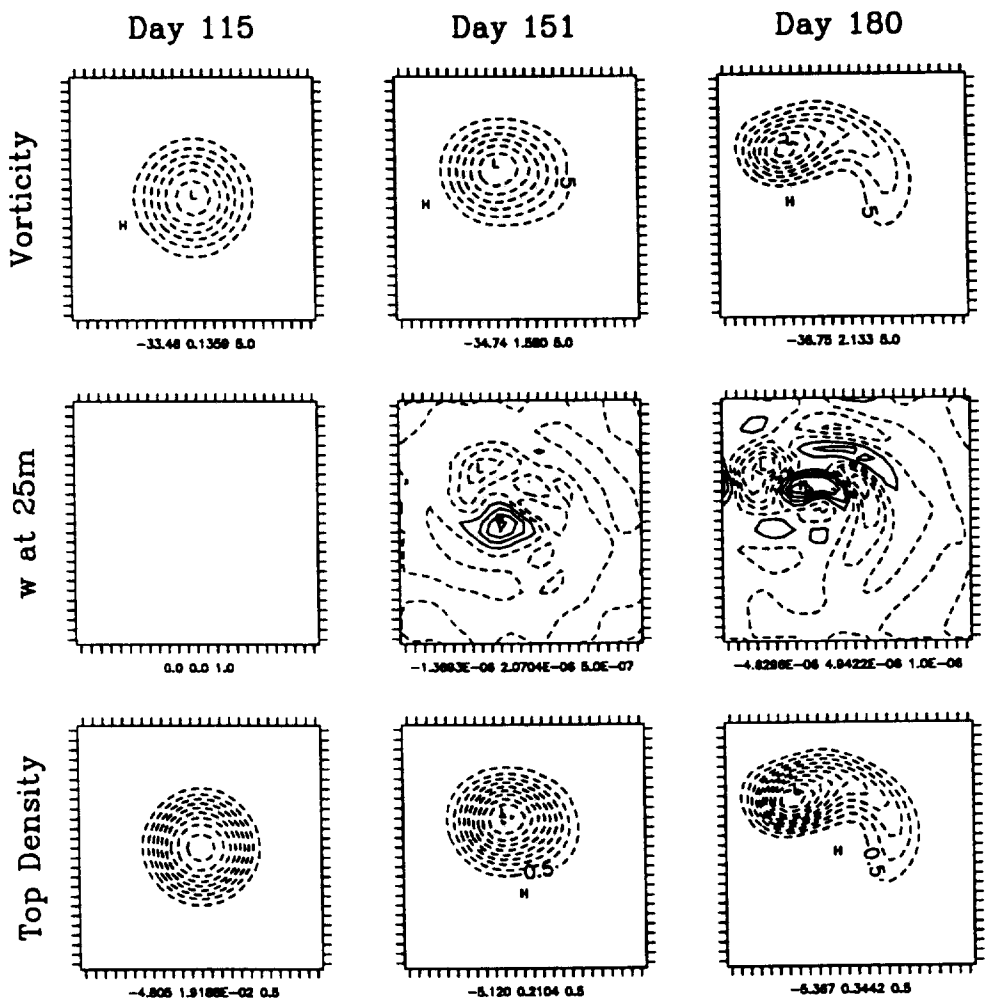


Fig. 10. Maps of vorticity at 50 m (nondimensional), vertical velocity at 25 m (m/s) and top density $\Gamma^2 \sigma \psi_{z|z=0}$ (nondimensional) in the initial condition (day 115) and after 36 and 65 days of integration.

the north–northwest and has become noticeably asymmetric. This behavior is characteristic of that observed in other numerical simulations of isolated vortices (e.g. McWilliams and Flierl, 1979). Submesoscale patches of vertical velocity have developed as a result of both the internal dynamics of the eddy and the interaction with the wind driven surface current. The evolution of the top density field is quite similar to that of the vorticity, and the maximum perturbation has increased by approximately 7%.

By Day 151, most of the nitrate has been removed from the mixed layer (Fig. 11) in a pronounced bloom event. Phytoplankton and heterotrophic biomass distributions reflect the pattern of the initial nitrate field, as the increased availability of nitrate inside the eddy has allowed the bloom to proceed much further in its interior. Mixed layer ammonium concentrations are quite low due to phytoplankton uptake, but show the same pattern of

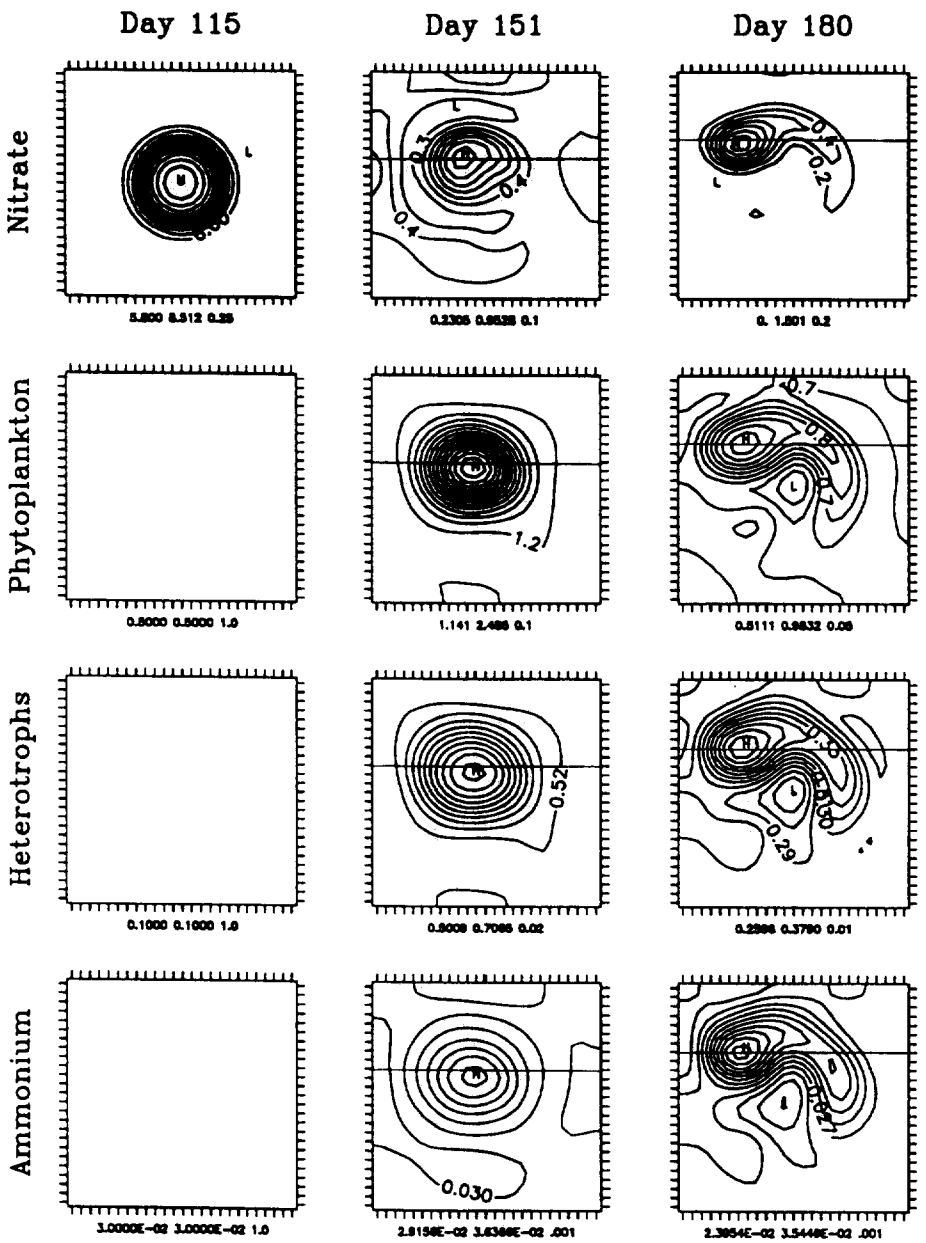


Fig. 11. Maps of mixed layer nitrate, phytoplankton, heterotrophs and ammonium ($\mu$M) in the initial condition (day 115) and after 36 and 65 days of integration.

enhancement inside the eddy because more nitrogen is being cycled through the phytoplankton–heterotroph–ammonium loop due to the initially higher nitrate concentration.

Vertical sections of the model solutions on day 151 from west to east along the line

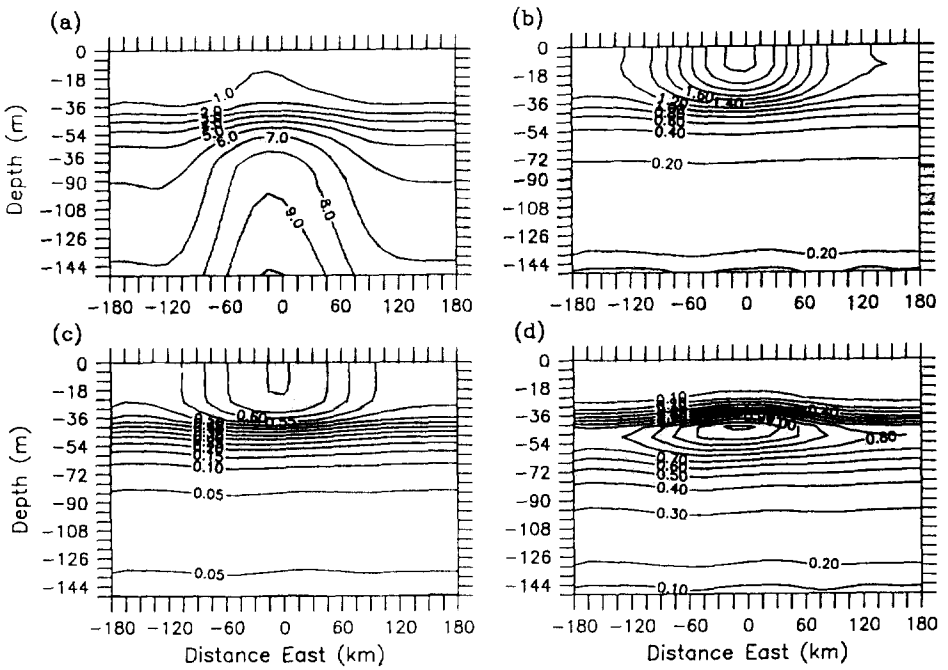


Fig. 12. Vertical sections of (a) nitrate, (b) phytoplankton, (c) heterotrophs and (d) ammonium ($\mu$M) taken from west to east across the Small eddy along the line indicated in Fig. 11 on day 151.

indicated in Fig. 11 are shown in Fig. 12. The removal of nitrate from the near surface region has produced a strong nitracline centered at approximately 45 m (Fig. 12a). The nitracline is slightly shallower in the eddy interior, where the doming of the nitrate surfaces is still quite evident in the deeper layers. Phytoplankton (Fig. 12b) and heterotrophic (Fig. 12c) biomass sections show enhancement in the eddy interior in the surface layers with strong gradients in approximately the same location as the nitracline. The gradients have a pattern opposite to the nitracline in that they are slightly deeper in the interior of the eddy. The ammonium distribution (Fig. 12d) has a pronounced subsurface maximum at around 45 m which is consistent with observations (MMR95). The subsurface maximum is significantly enhanced by the increased recycling inside the eddy. Vertical sections of some biological diagnostic quantities are shown in Fig. 13. Primary production (Fig. 13a) is enhanced in the surface layers inside the eddy mostly because of the increased biomass. At depth the surfaces of constant primary production are domed because self shading by the enhanced phytoplankton biomass has noticeably altered the light field (Fig. 13d). There is a sharp vertical gradient in the $f$-ratio at around 25 m where significant concentrations of ammonium exist (Fig. 13b). The highest $f$-ratio values are in the interior of the eddy where the enhancement of nitrate overshadows that of ammonium. The nutrient limitation factor $Q$ in the phytoplankton growth equation is shown in Fig. 13c. See MMR95 for more details concerning $Q$; phytoplankton growth is limited by nutrients as $Q$ approaches 0 and unlimited by nutrients as $Q$ approaches 1. Figure 13c reveals that on day 151 sufficient concentrations of nutrient remain to preclude any strong nutrient limitation, even in the mixed layer. The nutricline is located at the shallowest depth at which either nutrient is

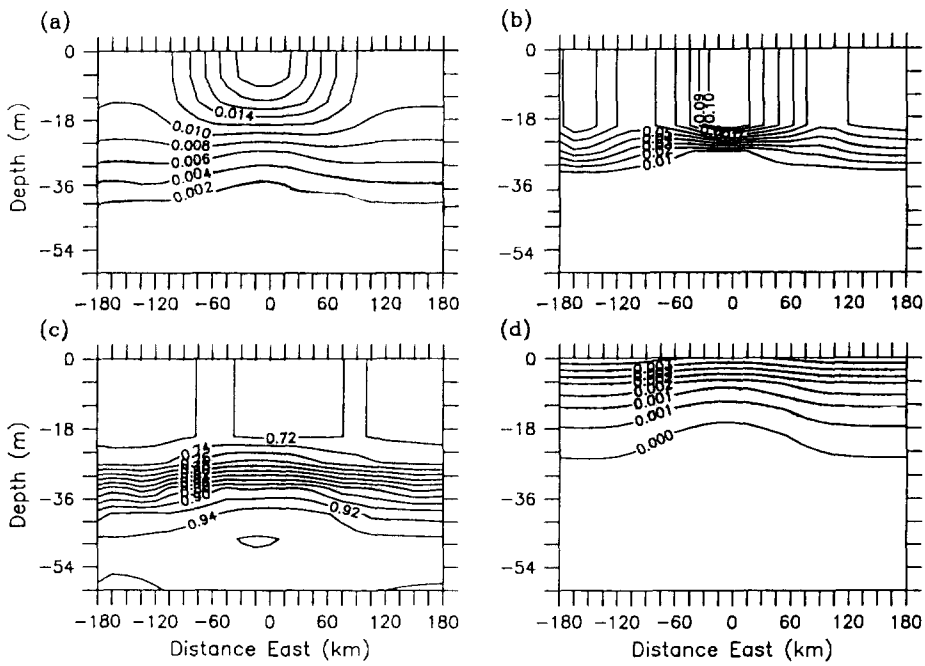


Fig. 13. Vertical sections of (a) primary production ($gNO_3/m^3/day$), (b) *f*-ratio (nondimensional), (c) nutrient limitation factor $Q$ (nondimensional) and (d) photosynthetically available radiation ($cal/cm^2/s$) from west to east across the Small eddy along the line indicated in Fig. 11 on day 151.

available in a concentration sufficient to allow phytoplankton uptake. This occurs at the ammonium gradient (30 m), which is much shallower than the nitracline (45 m). The enhanced surface nutrient concentrations inside the eddy slightly increase $Q$ in that region.

Between days 151 and 180 the core of the vorticity depression propagates at approximately the same speed but in a more westerly direction (Fig. 10). The asymmetry of the vorticity distribution has become much more exaggerated, as the eddy has evolved into an ellipsoid with a long vortex "tail" on its eastern flank. The vertical velocity has increased by a factor of 2–3, with patches of upwelling in the northern and southern portions of the eddy, and downwelling to the east and west. The top density perturbation has continued to deepen and its pattern reflects the distortion of the vorticity field.

By day 180 nearly all of the nitrate has been removed from the mixed layer in the waters surrounding the small eddy, reflecting a post-bloom situation (Fig. 11). More than half of the phytoplankton biomass produced during the bloom has been consumed by heterotrophs. Inside the eddy the situation is quite different. The mixed layer nitrate concentration has actually *increased* to values in excess of (1 $\mu$M) in the central core. Nitrate enhancement is evident from the eddy core out to the vortex tail. The increased nitrate supply has sustained post-bloom phytoplankton growth, but heterotrophic consumption limits phytoplankton accumulation. The phytoplankton, heterotroph and ammonium distribution patterns are quite similar to that of nitrate, except for an area of significantly lower concentration just to the south of the vortex tail. Close examination of a time series of the nitrate and phytoplankton fields (Fig. 14) reveals the origin of this feature. On day 160 the central core of high nitrate in the small eddy has an area of low concentration

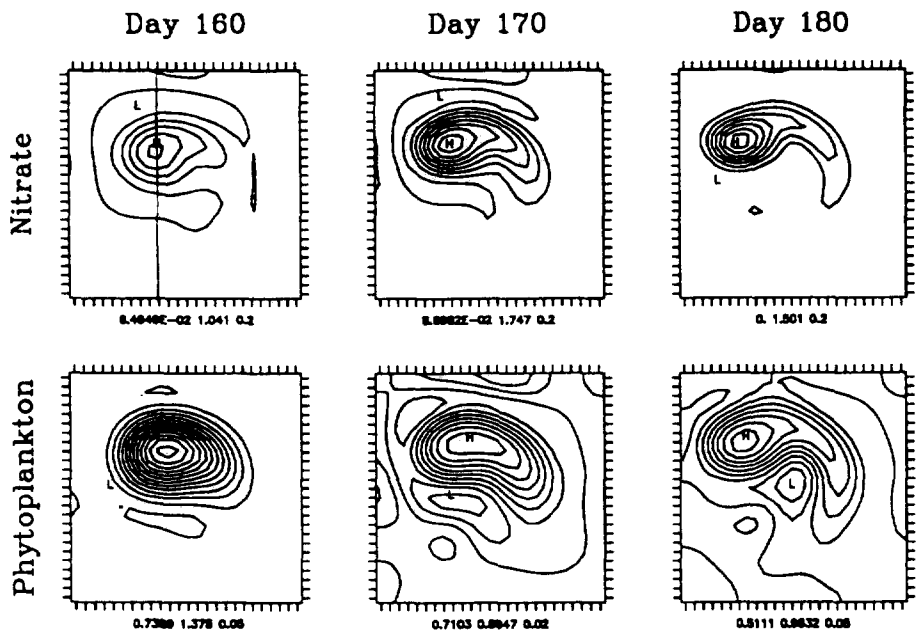


Fig. 14. A time series of mixed layer nitrate and phytoplankton fields from day 160 to 180.

surrounding it. A vertical section of nitrate on this day shows that the nutrient surfaces dip downward slightly on the borders of the eddy and then rise again to the background level (Fig. 15). This structure can be interpreted as the disturbance caused by wave radiation as the vortex decays. The low nutrient band around the eddy results in the development of phytoplankton biomass minima in this region by day 160 (Fig. 14). By day 170, the biomass minimum to the south of the eddy has become more pronounced while the anomaly in other quadrants surrounding the eddy is masked by the propagation of the vortex. The strong minimum to the south of the eddy on day 170 is subsequently advected eastward during the vortex tail formation and by day 180 it is tucked tightly against the southern flank of the eddy as the tail begins to wrap around it.

Vertical sections of the model solutions on day 180 from west to east along the line indicated in Fig. 11 are shown in Fig. 16. Outside the eddy the nitracline has deepened due to removal by phytoplankton and broadened somewhat via diffusive processes (Fig. 16a). In the interior of the eddy the nitracline is closer to the surface and the outcropping of the (1 $\mu$M) isocline of nitrate is evident. At depth the doming of the nutrient surfaces has spread eastward with the formation of the vortex tail. The phytoplankton, heterotroph and ammonium (Fig. 16b–d) distributions are similar in pattern to those on day 151 with the exception that the eddy anomalies extend further to the east in the vortex tail. In general the concentrations of the material are lower because of consumption and export. The subsurface ammonium maximum has descended due to heterotrophic grazing on sinking phytoplankton. Biological diagnostic quantities along the same section are shown in Fig. 17. The rate of primary production (Fig. 17a) has decreased considerably with the reduction in phytoplankton biomass. The $f$-ratio (Fig. 17b) has risen in the interior of the

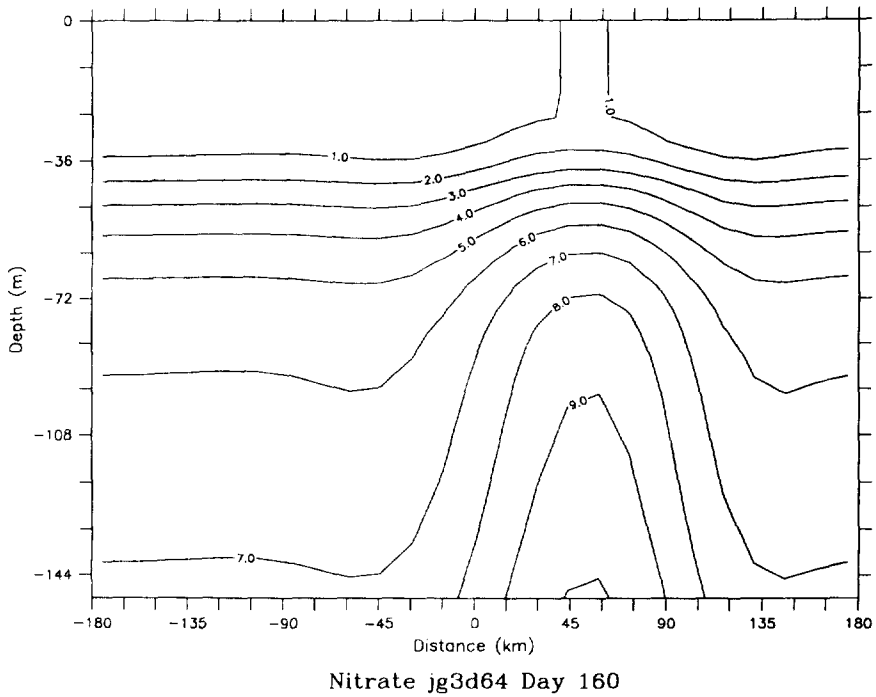


Fig. 15. A vertical section of nitrate from south to north across the Small eddy along the line indicated in Fig. 14 on day 160.

eddy due to the greater availability of nitrate. Areas of nutrient depletion on the borders of the eddy are visible as minima in the nutrient limitation factor $Q$ (Fig. 17c). Ammonium concentrations in these regions are slightly higher than nitrate (taking the ammonium preference into account) so the $f$-ratio is lower in these areas. The mesoscale signal in the light field is smaller in magnitude as compared to day 151 as the lower phytoplankton biomass reduces self shading (Fig. 17d).

Comparison of the three dimensional model solutions with the one dimensional results is facilitated by extracting a time series of profiles from the three dimensional fields. Far from the eddy, the three dimensional results are nearly identical to the one dimensional solutions and therefore are not shown here. Inside the eddy there are noticeable differences (Fig. 18). At depth the nitrate contours of the three dimensional solution rise in time while those in the one dimensional case do not, indicating that upwelling is occurring in the interior of the eddy (Fig. 18a). This supply of nutrient effectively slows the descent of the nitrate surfaces in the euphotic zone in the three dimensional simulation. Thus the upwelled flux serves to partially offset the nutrient removal by phytoplankton so that nitrate concentrations are generally higher in the three dimensional case. A striking aspect of this behavior is that the increase in available nutrient results in little additional phytoplankton biomass accumulation as compared with the one dimensional simulation inside the eddy (Fig. 18b). This is a result of the tight coupling between the phytoplankton and heterotrophic populations, which is quite evident in the time series of the integrated nitrogen reservoirs (Fig. 19). During the phytoplankton bloom there is a corresponding

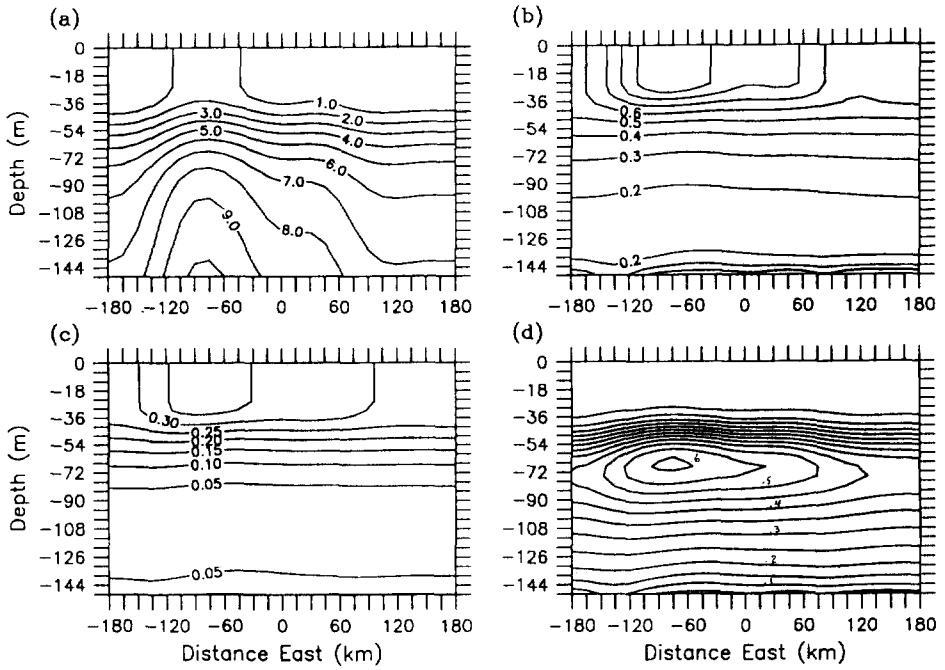


Fig. 16. Vertical sections of (a) nitrate, (b) phytoplankton, (c) heterotrophs and (d) ammonium ($\mu$M) taken from west to east across the Small eddy along the line indicated in Fig. 11 on day 180.

increase in heterotrophic biomass that lags by only a few days. As soon as the phytoplankton become nutrient stressed, the heterotrophs overtake them and phytoplankton biomass begins to decline. Heterotrophic biomass also declines as the bulk of the material fixed during the bloom is exported to depth. Even subsequent to the bloom most of the nitrate that is removed is exported on a fairly short time scale; that is, late in the simulation (days 165–180) the rate of nitrate removal and the rate of nitrogen export are roughly equivalent, resulting in fairly stable biomass distribution.

Figure 20 compares time series of mixed layer nitrate for the one dimensional and three dimensional simulations inside and outside the small eddy. During the first part of the simulation the one dimensional and three dimensional solutions in the two locations are quite similar, as the main signal is a one dimensional bloom process in which the evolution is, to a large extent, determined by the initial nitrate distribution. Because the initial condition is mixed beyond the euphotic zone, no significant gradients exist in the region in which physical transports can effectively supply nutrient to the surface layers. However, during the bloom phytoplankton uptake creates a sharp nitracline on which physical transport processes operate. After about day 145 three dimensional mesoscale transport processes significantly enhance the mixed layer nitrate concentration inside the small eddy. Toward the end of the simulation the concentration predicted by the three dimensional model is more than twice that of the one dimensional case. This enhancement is attributable to a combination of the propagation flux mechanism discussed in section 3 and the lifting of the nitrate surfaces in the interior of the eddy due to the dynamics of the vortex evolution.

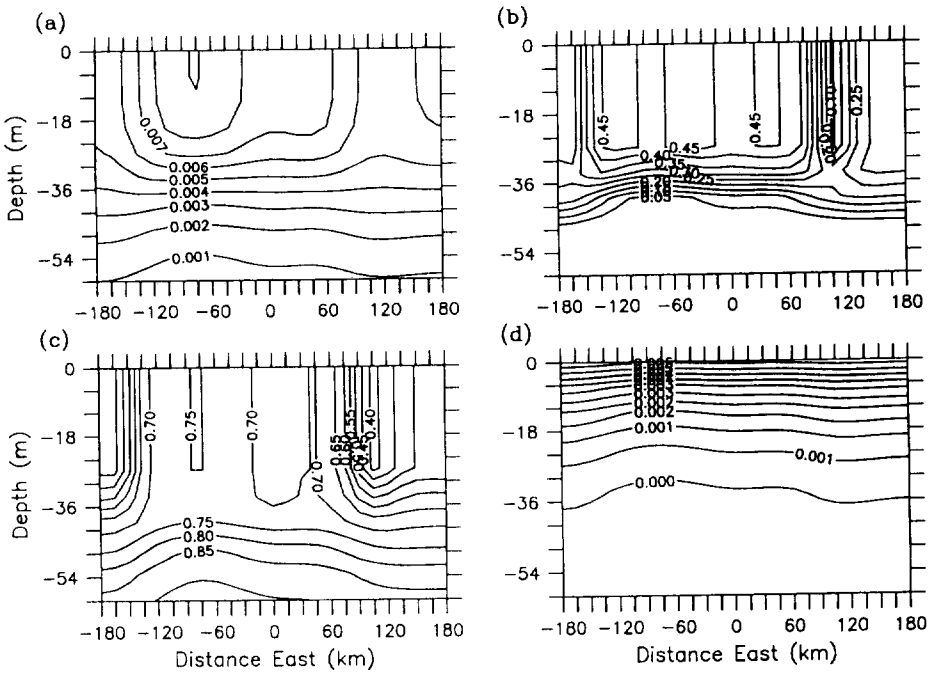


Fig. 17. Vertical sections of (a) primary production ($gNO_3/m^2/day$), (b) *f*-ratio (nondimensional), (c) nutrient limitation factor $Q$ (nondimensional) and (d) photosynthetically available radiation ($cal/cm^2/s$) from west to east across the Small eddy along the line indicated in Fig. 11 on day 180.

It is important to note that this nutrient enhancement causes the three dimensional simulation to appear less consistent with the data inside the eddy on days 142–151 than the one dimensional simulation. There are two possible explanations for this discrepancy. If three dimensional eddy processes were actively transporting nutrients toward the surface in the real ocean during this time, the biological model may have been improperly tuned in MMR95 to counterbalance the absence of these processes in the one dimensional model. Alternatively, it may be that eddy upwelling was not actually taking place inside the eddy on days 142–151 in the real ocean. These mesoscale dynamical events are spatially and temporally intermittent, and the physical oceanographic data available for this experiment are insufficient to determine whether or not upwelling was taking place during this particular time at this location. Therefore it is not possible to ascertain which of these two explanations is more likely.

The time series in Fig. 20 is useful for interpretation of some aspects of the spatial and temporal variability of the data. Previously it has been argued (MMR95) that the drawdown of nitrate in the first time series outside the small eddy was biased by the sampling pattern which covered some cold submesoscale features and then moved toward the interior of the small eddy later in the record. The fact that the data are bracketed by the model solutions inside versus outside the eddy lends plausibility to this argument that spatial variability can be misinterpreted as temporal variability if time series sampling is not conducted in a single water mass. Further analysis of this issue follows in section 7.

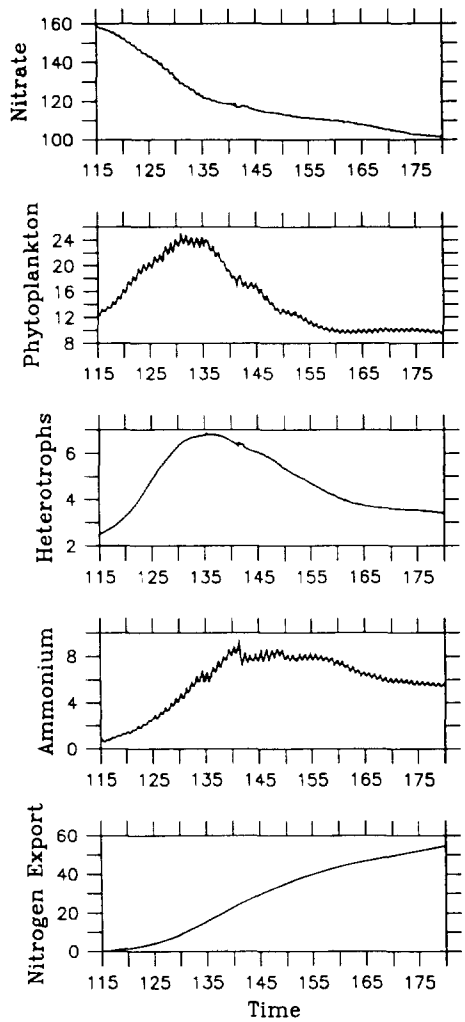


Fig. 19. Time series of the spatially integrated nitrogen reservoirs.

## 6. THREE DIMENSIONAL SIMULATION: BIG, STANDARD AND SMALL EDDIES

In this simulation the physical field is initialized with the best estimate of the three eddy configuration observed during the beginning of the 1989 North Atlantic Bloom Experiment. Between days 115 and 151 the three eddies evolve and interact (Fig. 21). The Small eddy has become elliptical in shape, with its semimajor axis oriented northwest–southeast. The northwest corner of the small eddy is interacting strongly with the Standard eddy and some deformation of the Standard eddy vorticity distribution is evident in this region. The Standard eddy is also interacting with the Big eddy. A pronounced vortex filament extends eastward from the northeast quadrant of the Standard eddy toward a lobe that has formed in the southern portion of the Big eddy. The southern lobe of the Big eddy extends far enough south so that it appears to be weakly interacting with the Small eddy. A

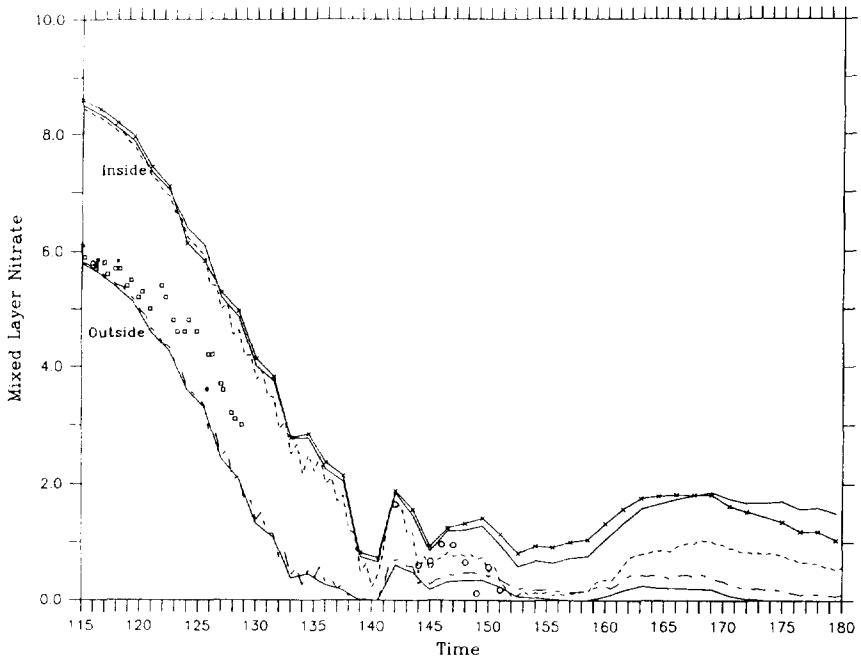


Fig. 20. Time series of mixed layer nitrate concentration ($\mu$M) extracted from three dimensional model solutions of the Small eddy in isolation (solid lines) and one dimensional model solutions (dashed lines) inside and outside the small eddy. The solid line connecting crosses corresponds to the time series inside the Small eddy in the three eddy case. Observations are indicated by squares and circles.

submesoscale circulation cell has formed in the center of the three way interaction region (area C on day 151 in Fig. 21). The variations in vertical velocity are associated with the major eddy interactions. The strongest patches of $w$ on day 151 are alternating areas of upwelling and downwelling arranged in east–west streaks in the Standard–Big eddy interaction region. North–south streaks of $w$ are located where the Standard and Small eddies are interacting. Weak patches of $w$ oriented east–west are visible where the southern lobe of the Big eddy meets the Small eddy. The top density pattern is very similar to the vorticity distribution.

By day 151, most of the nitrate has been removed from the mixed layer (Fig. 22). Phytoplankton and heterotrophic biomass distributions reflect the pattern of the initial nitrate field, as the increased availability of nitrate inside the eddies has allowed the bloom to proceed much further there. Advection by the eddy velocities has caused the evolution of asymmetries in the biological fields that are very similar to the patterns in the vorticity field. Mixed layer ammonium concentrations are quite low due to phytoplankton uptake, but show the same pattern on enhancement inside the eddy because the increased biomass has resulted in more nutrient recycling.

One interesting aspect of the biological model solutions on day 151 is the significant enhancement of surface nitrate in the core of the Small eddy. This increase in nitrate appears to be associated with the interaction of the Small and Standard eddies. On day 139, the Small eddy is still mostly circular in shape (Fig. 23a). At this time the maximum

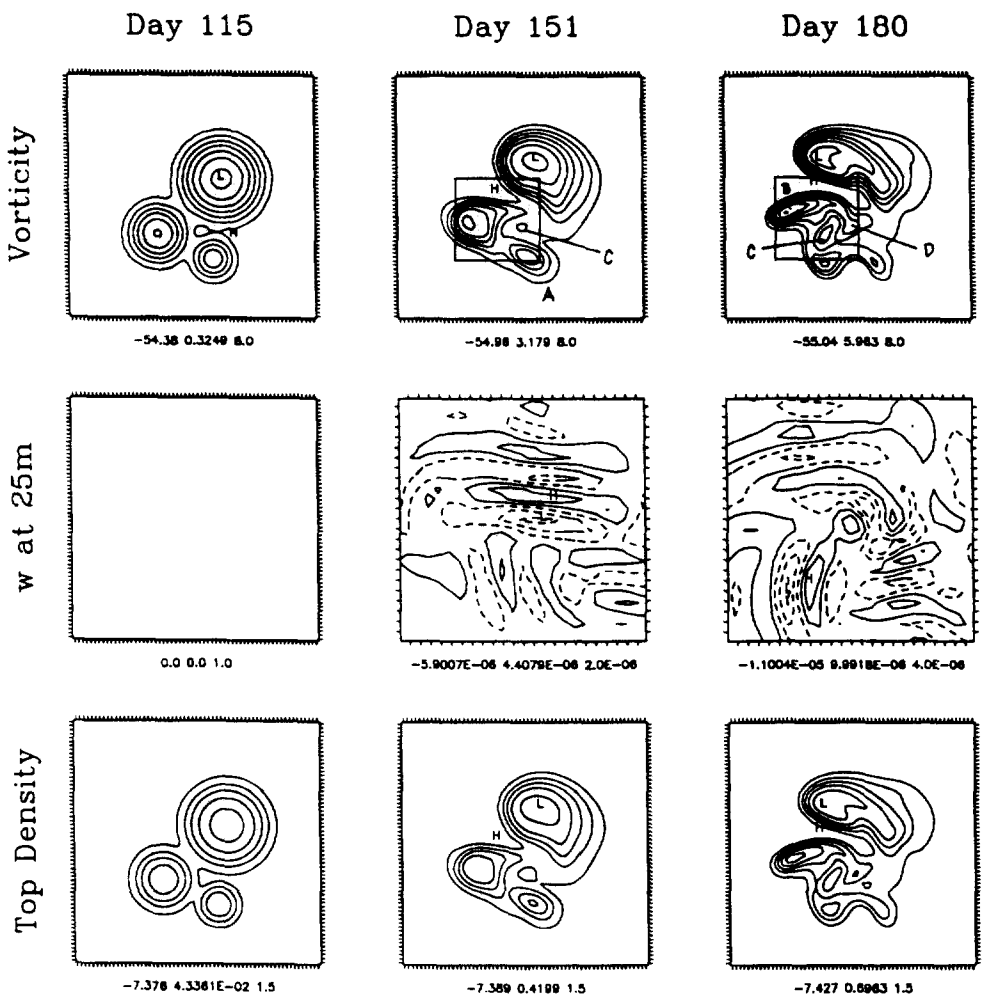


Fig. 21. Maps of vorticity at 50 m (nondimensional), vertical velocity at 25 m (m/s) and top density $\Gamma^2 \sigma_{\psi^*|z=0}$ (nondimensional) in the initial condition (day 115) and after 36 and 65 days of integration. Vertical velocity is shown for the inset area indicated on the vorticity maps. Note that the contours on the vorticity and top density maps are negative; the usual convention of using dashed contours for negative values has been omitted in these cases for clarity of presentation.

mixed layer nitrate value is located in the core of the Big eddy (not shown), reflecting the initial nitrate distribution. Between days 139 and 151 the Small eddy becomes demonstrably more elliptic (Fig. 23b). This change in the eddy configuration is accompanied by significant upward displacement of the nitrate surfaces (Fig. 23c). The upwelling of the nutrient surfaces is quite evident in the deeper portions of the vertical section, as displacements as large as 18 m occur along the southeastern edge of the eddy during the 12 day period. Changes in the nutrient surfaces over time are more difficult to diagnose in the euphotic zone for a variety of reasons. First, phytoplankton uptake tends to displace the surfaces downward, countering the upwelling. Further, nitrate removal varies rapidly with

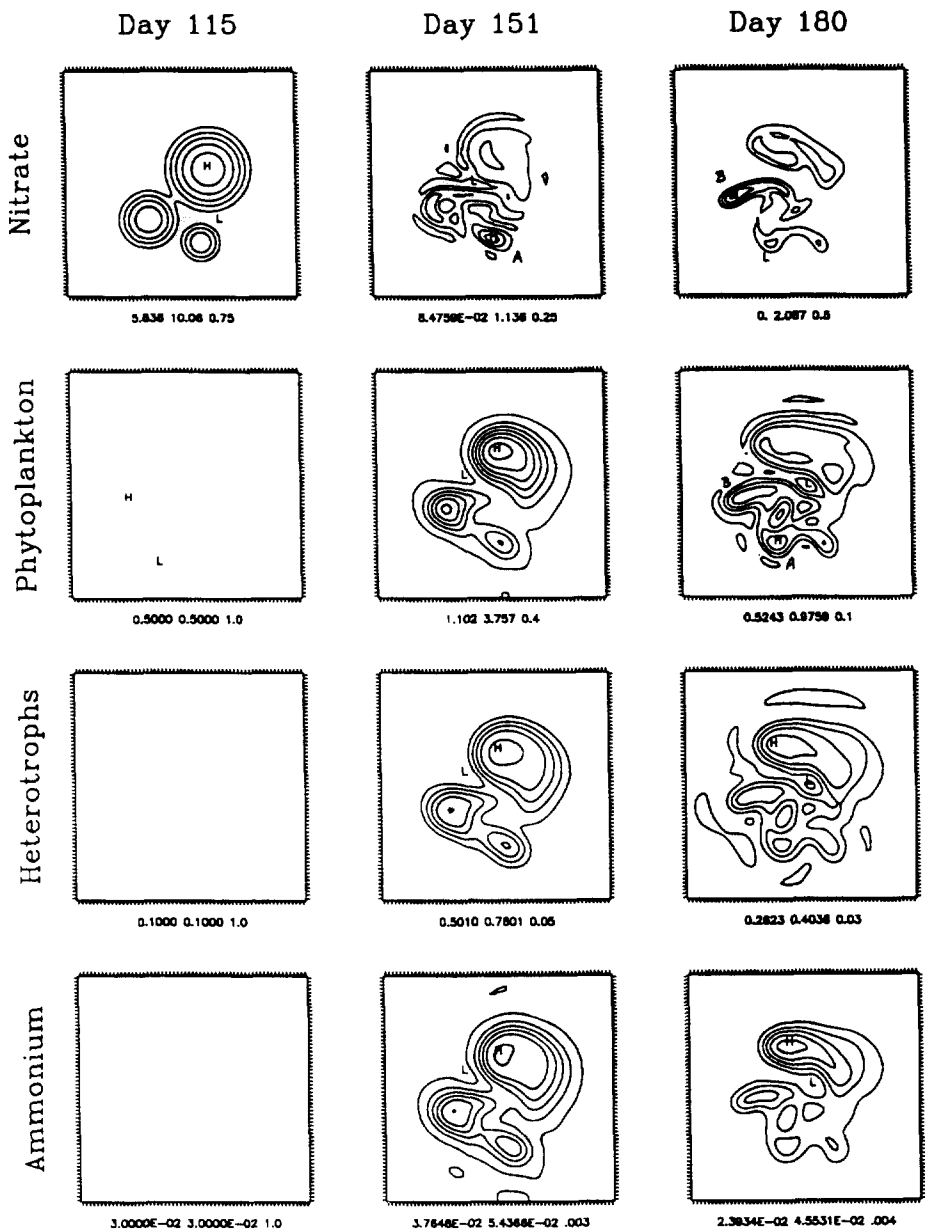


Fig. 22. Maps of mixed layer nitrate, phytoplankton, heterotrophs and ammonium ($\mu$M) in the initial condition (day 115) and after 36 and 65 days of integration.

depth because of the exponential extinction of light. Thus the relative strength of the supply and demand processes changes with depth. This is further complicated by the existence of a mixed layer at the surface, in which changes over time reflect the balance between the two processes integrated over the layer depth. Quantitative diagnosis of the model solutions in such circumstances requires a consistent analysis scheme in which the

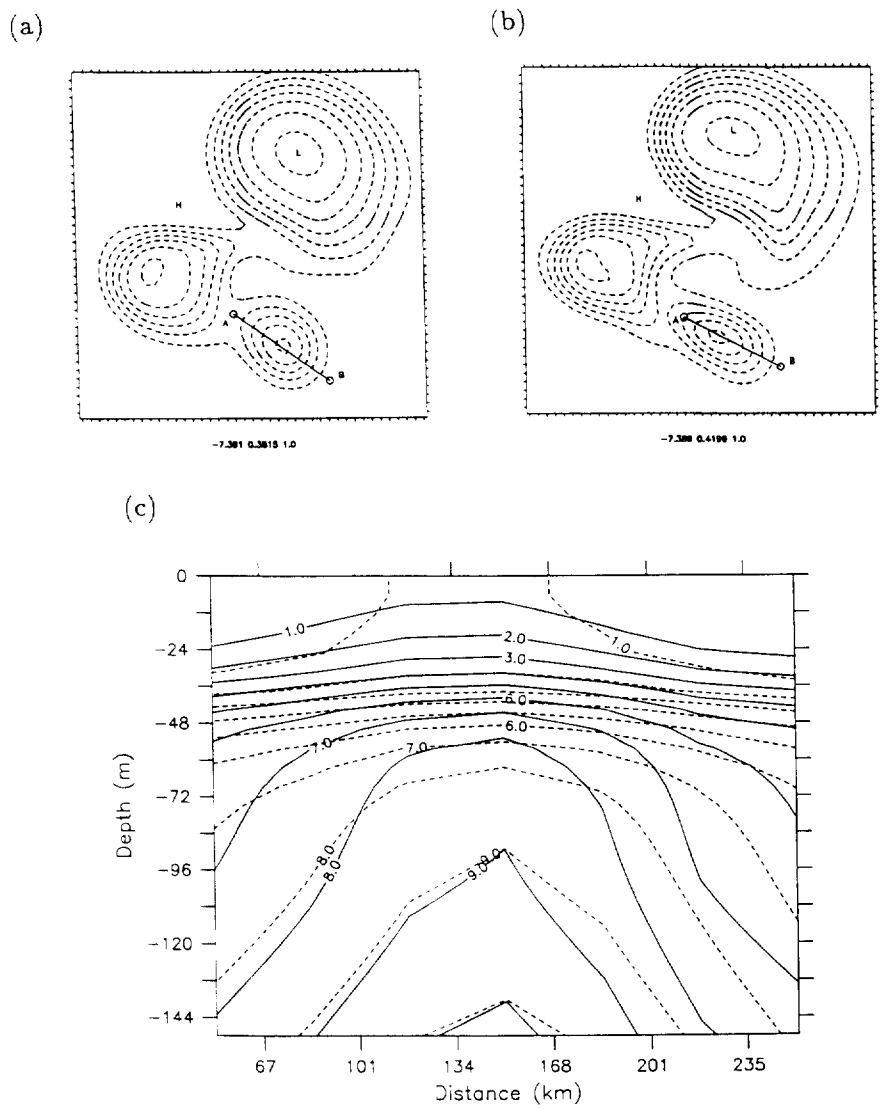


Fig. 23. Maps of nondimensional top density $\sigma\eta_{z=0}$ on (a) day 139 and (b) day 151. Panel (c) shows a vertical section of nitrate taken from A to B on day 151 (dashed contours) overlaid on the section taken on day 139 (solid contours).

balance of terms can be examined. However, it is qualitatively clear that the net supply of nitrate from below is responsible for the enhancement of mixed layer nitrate inside the eddy as the 1 $\mu$M nitrate surface outcrops on day 151 where it previously did not.

Between days 151 and 180 further evolution and interaction of the three eddies occurs (Fig. 21). The Small eddy separates into two distinct lobes oriented east–west. This configuration is consistent with the eddy structure indicated in the second eddy report documented in Robinson *et al.* (1993). The Standard eddy has become much more elliptical and is interacting very strongly with the western lobe of the Small eddy. The Big

eddy has also become more elliptical and propagated to the west–northwest. Its southern lobe has developed and rotated counter clockwise around the center of the eddy and lies northeast of its previous position on day 151. The interaction feature located at C on day 151 has been swept into the region between the Standard eddy and the western lobe of the Small eddy. An additional interaction feature is now located at D on day 180 that formed as the easternmost filament of the Standard eddy (located just to the north of C on day 151) snapped off. The vertical velocity field is similar in character to that of day 151. The most intense vertical motion is occurring in north–south streaks in the region where the Small and Standard eddies are interacting. East–west streaks are also visible in the neck region between the two lobes of the Small eddy. Alternating patches of upwelling and downwelling also occur in the regions of the strongest vorticity gradients between the Standard and Big eddies.

In general the simulated behavior of the three eddy configuration beyond the time period analyzed in Robinson *et al.* (1993) is consistent with Geosat observations. Analysis of the 14 altimetric tracks that cross the eddy features during the two subsequent repeat cycles (days 145–161 and 162–178) reveals that the features persist and interact during this time period. There is evidence of a deepening of the Standard eddy's sea surface depression associated with its evolution and interaction with nearby features. Although the detailed interaction of the eddies is difficult to ascertain from a subjective analysis of the Geosat tracks alone, the simulated evolution appears consistent with the available data.

In general it is of considerable interest to assimilate the altimetric, hydrographic and biogeochemical data directly into the numerical model to produce optimal estimates of the four dimensional fields as they evolve. This is accomplished by first tuning and validating the model with the data as done here and then directly assimilating it. Such representations will agree with observations where they are available and be dynamically consistent across data sparse regions. Existing methodologies are capable of achieving such a goal and will be used in the near future.

The eddy dynamics has had a remarkable impact on the chemical and biological fields during this period (Fig. 22). Nitrate concentrations inside the Standard eddy on day 180 (location B) have been enhanced to over 2 $\mu$M, representing a 10-*fold increase over the background concentration*. This nutrient injection occurs during the period in which the Standard eddy undergoes rapid and dramatic evolution. On day 153, the top density perturbation of the Standard eddy is fairly circular, although its northeast and southeast corners are distorted due to interactions with the Big and Small eddies, respectively (Fig. 24a). The density perturbation at the core is notably diffuse. By day 180, the eddy has become quite elliptical (Fig. 24b). The gradients around its borders have tightened, and the peak perturbation in the eddy core has deepened and become quite sharp. This has a major effect on the nitrate field. Comparing the vertical sections across the Standard eddy on days 153 and 180 shows that the eddy interactions have lifted the deeper nitrate surfaces in excess of 20 m in some locations during this seven day period (Fig. 24c). As before, biological removal damps the effect in the euphotic zone. However, both the 1 $\mu$M and 2 $\mu$M nutrient surfaces outcrop in an area where mixed layer nitrate concentrations were approximately 0.2 $\mu$M before. This flux of nitrate has stimulated phytoplankton growth and resulted in some accumulation in region B in Fig. 22. The maximum phytoplankton concentration is actually located at A, which is the result of the dynamically induced nutrient enhancement in the Small eddy shown at location A on day 151. As with the single

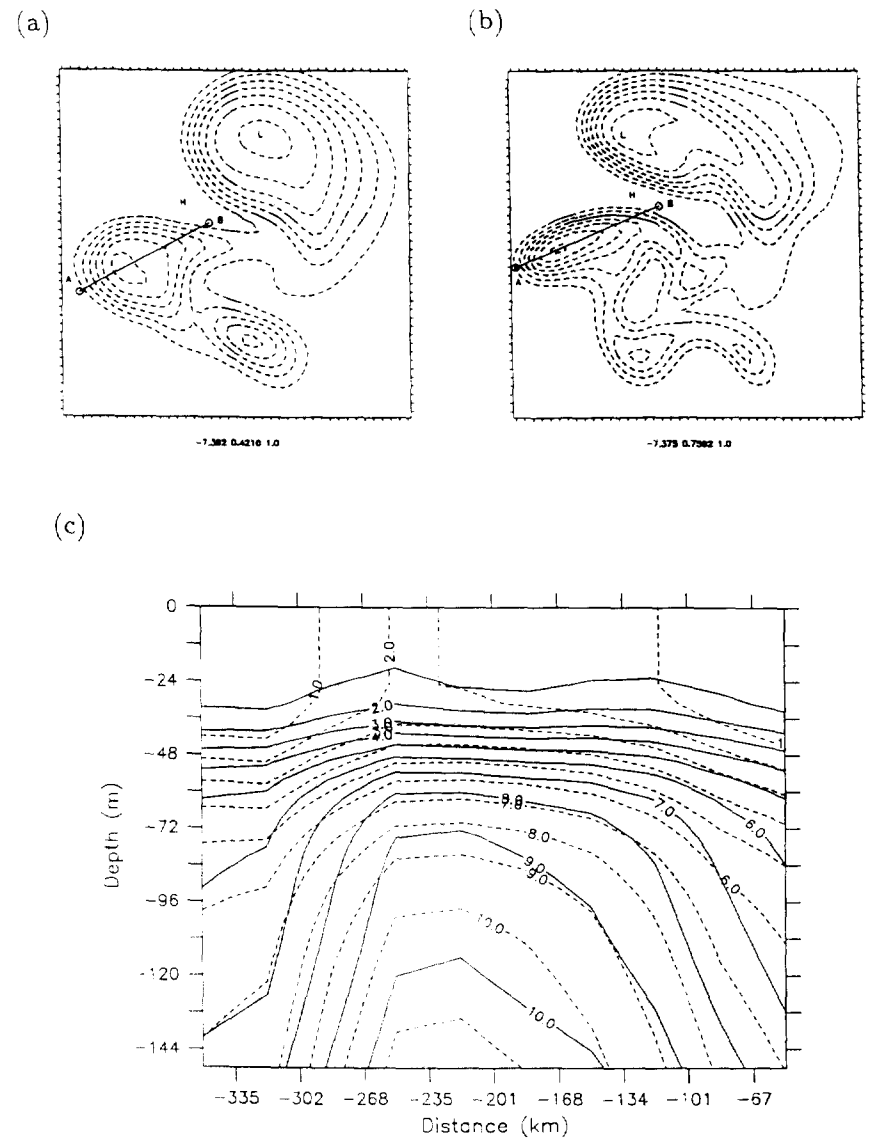


Fig. 24. Maps of nondimensional top density $\sigma_{t=0}$ on (a) day 173 and (b) day 180. Panel (c) shows a vertical section of nitrate taken from A to B on day 180 (dashed contours) overlaid on the section taken on day 173 (solid contours).

eddy case phytoplankton accumulation is not a strong indicator of primary productivity because the tightly coupled heterotrophic community rapidly consumes excess phytoplankton biomass.

Comparing the Small eddy behavior to the previous case in which it evolved in isolation is instructive. The evolution of the nitrate profile in the core of the eddy is quite different in the two cases (Fig. 25). In the three eddy case the Small eddy begins to separate into the two lobe feature by about day 160. This causes a significant weakening of the eddy pertur-

bation, and the deep nitrate surfaces in the three eddy case take a dramatic turn downward. This behavior is of course not observed in the isolated eddy case as the deep nitrate surfaces continue to rise throughout the simulation. In the mixed layer, nitrate concentrations are quite similar in the two cases until about day 148 when the interaction with the Standard eddy enhances nitrate in the three eddy case (Fig. 20). On day 169 mixed layer nitrate in the three eddy case drops below that of the one eddy case. This is most likely due to two contributing factors. First, the tendency of the Small eddy to propagate to the northwest is not encumbered by the presence of the other eddies in the isolated case. Thus the propagation flux in the isolated case is higher and this enriches mixed layer nitrate concentrations. Second, as the Small eddy separates into two lobes the eddy perturbation decreases, lowering nitrate concentrations.

In general the patterns simulated in the three eddy case are consistent with what few measurements are available concerning the spatial variability of the biological and chemical fields. Airborne Oceanographic Lida (AOL) was used on board the NASA P-3 aircraft during the NABE to observe laser induced chlorophyll fluorescence as a proxy for phytoplankton biomass (Yoder *et al.*, 1993). Structure–function analysis of several overflights of the experimental area revealed alongtrack chlorophyll length scales ranging from 10 km to 290 km. These smallest length scales could be associated with submesoscale features, while the largest scales are consistent with the simulated mesoscale pigment variations. Similar length scales are evident in structure function analysis of Coastal Zone Color Scanner imagery for the region (Robinson *et al.*, 1993). An AOL flight track across the Standard eddy showed enhanced pigment concentrations in the interior of the feature (Robinson *et al.*, 1993). This chlorophyll enhancement was also observed in a SeaSoar survey (Lochte *et al.*, 1993). Chlorophyll concentration inside the eddy was nearly a factor of two higher inside versus outside the eddy, which is consistent with the simulations.

## 7. A RETROSPECTIVE ANALYSIS OF THE BLOOM DATA WITH THE THREE DIMENSIONAL MODEL

In MMR95 it was argued that the sampling pattern of the early bloom experiment biased the time series by moving from warm features to cold ones. The results of the three eddy simulation lend further support to this claim. Figure 26a shows the cruise track overlayed on a map of mixed layer nitrate concentration extracted from the model on day 128. Sampling began in the interfacial region between the Standard and Small eddies, moved southeast into the swirl of the Small eddy, then southwest away from both eddies, then north toward the swirl of the Standard eddy, and finally a nearly 100 km transit was made back into the swirl of the Small eddy. Recall how the observations are bounded by simulated time series extracted from the model in single water masses inside and outside the Small eddy (Fig. 20). Comparison of early bloom mixed layer nitrate observations with a simulated time series extracted from the evolving model fields along the cruise track shows good agreement (Fig. 26b). The model nitrate drawdown is quite consistent between days 115 and 121 when the observations move from outside the Small eddy into its swirl and back out again. Agreement is also satisfactory from days 127–129 when stations are again located in the swirl of the Small eddy. However, from days 121 to 127 the observations suggest less nitrate removal (more apparent supply) than does the model. While the possibility that the discrepancy is of biological or chemical origin cannot be ruled out, apparent supply from the aliasing of spatial variability is likely. Figure 1 of

(MMR95) shows that the observations during days 121–127 were taken in a distinctively cold water mass to the west of the Small eddy. It may be that this cold feature is a submesoscale flow not represented in the present simulation. Alternatively, the observations could be located in the southeastern flank of the Standard eddy, as Fig. 26a would indicate. If this were the case, a mere 50 km deformation of the Standard eddy in this area (which is well within the error bars of the available data) would provide enough apparent nitrate supply to account for the difference. To demonstrate this, the cruise track is hypothetically extended into the swirl of the Standard eddy (Fig. 26a, dashed line). This brings the resulting time series of mixed layer nitrate into full agreement with the data (Fig. 26b).

In this case it was possible to reconcile the observations with time series extracted from the model simulation. Much more powerful contact between models and data can in general be achieved through the process of data assimilation. Such techniques are routinely used in meteorology and physical oceanography to maintain optimal agreement between observations and models. In fact, data assimilation yields field estimates that agree with the data to within prescribed error bounds and are consistent with model dynamics. Data assimilation schemes will be extremely useful for interdisciplinary applications to maximize the utility of sparse observations in creating dynamically consistent fields that agree with all available data.

## 8. SUMMARY AND CONCLUSIONS

This study and its companion paper (MMR95) have introduced a mesoscale eddy resolving coupled physical and biological model. The interdisciplinary model system has been tuned to the NABE data in Part 1, and it was shown that the general features of the early phase of the bloom can be represented in a one dimensional framework when the mesoscale spatial variability in the pre-bloom nutrient distribution is treated explicitly. Results from the full three dimensional model indicate that physical structures and transports significantly influence biogeochemical fluxes and ecosystem dynamics. Mesoscale dynamical processes dominate late-bloom and post-bloom biological fields.

The preceding simulations have demonstrated a diversity of mesoscale processes that can transport nutrients into the euphotic zone. Using the nutrient model in an isolated eddy it was possible to isolate and quantify the flux caused by vertical motions arising from various sources. In this case the vertical velocity associated with the internal dynamics of an eddy evolving in isolation is fairly weak, as the flow remains relatively stable and quiescent. The addition of moderate wind forcing more than doubles the nutrient flux through vortex stretching that arises from the advection of the interior vorticity by the Ekman velocity. The effect of these two processes combined accounts for less than half of the total nutrient transport observed when the eddy is allowed to propagate freely. This "propagation flux" causes an effective vertical velocity of approximately 3 m per day in this case. It is the kinematic result of the linear propagation of the domed nitrate surfaces inside the cyclonic eddy. This process is not necessarily limited to vortex propagation. Theoretically this effective upward transport will occur along the leading edge of any moving feature consisting of raised density surfaces. In fact this kinematic mechanism of vertical transport has been identified in the eastward propagation of Gulf Stream meanders and is consistent with RAFOS float observations (Bower, 1991).

Numerical experiments with the full four component biological model provide a more

(a)

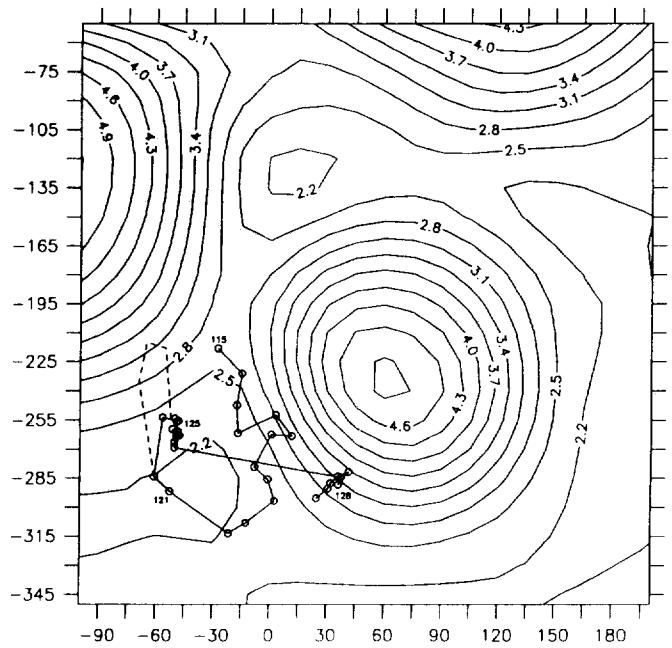
-75
-105
-135
-165
-195
-225
-255
-285
-315
-345
-90 -60 -30 0 30 60 90 120 150 180
115
125
121
128
2.2
2.5
2.8
3.1
3.4
3.7
4.0
4.3
4.6

Day 128.5

(b)

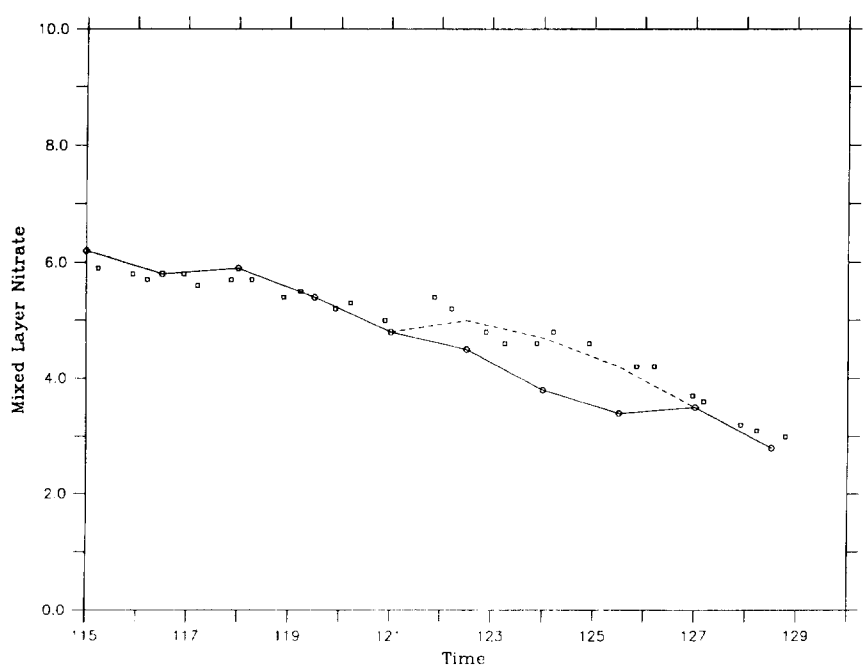
Mixed Layer Nitrate
10.0
8.0
6.0
4.0
2.0
0.0
115 117 119 121 123 125 127 129
Time

realistic context in which the effects of these and other transport processes can be studied. Early in the spring bloom the evolution of the chemical and biological properties of the interior of the Small eddy in isolation is quite similar to that predicted by a one dimensional model. Because the initial condition is well mixed to substantial depth, gradients on which physical transport processes operate are absent in the early part of the simulation. Later in the bloom, after a strong nitracline has been established by phytoplankton uptake, the efficacy of the mesoscale transports begins to emerge. Significant nutrient enhancement is observed in the interior of the vortex which is consistent with the propagation flux. Post-bloom mixed layer nitrate concentrations are more than double those of the one dimensional case. The tightly coupled heterotrophic population damps the phytoplankton biomass response.

In the three eddy case the propagation of the Small eddy is inhibited by the presence of the neighboring vortices. However, the eddy interaction processes in this case turn out to provide a more dramatic nutrient supply to the upper ocean. The Standard–Small eddy interaction pumps even more nitrate into the mixed layer than the free propagation of the Small eddy. This supply of nitrate is converted into phytoplankton biomass and the interior of the Small eddy becomes the biomass maximum in the overall eddy field. A stronger eddy interaction between Standard and Big occurs later in the simulation that results in an order of magnitude enhancement of mixed layer nutrient concentration inside the Standard eddy. This nutrient flux associated with eddy interactions appears to be a general process that occurs over much larger spatial scales (the scales of the eddies themselves) than the submesoscale hotspots predicted by Woods (1988) to be the primary effect of mesoscale dynamics on biological productivity.

Of course the main challenge in fully understanding and unequivocally demonstrating the importance of mesoscale dynamics on biological productivity still remains: that of actually observing intense dynamical events and their biological and chemical ramifications. Recent advances in both remote sensing and *in situ* techniques have made it feasible to sample the relevant variables on appropriate space and time scales. To exploit this observational capability, an interdisciplinary model system such as the one used here can serve as a framework for the synthesis of the extensive and diverse data sets required for capturing coupled physical–biological processes. Assimilation schemes force the model system to stay in agreement with available data and provide dynamically consistent fields across data sparse regions. The availability of these space–time continuous fields facilitates process studies of complex phenomena for which all necessary fields cannot practically be measured. In this regard a synergy is created in the combination of models and data that will greatly accelerate progress toward understanding physical–biological interactions in the world ocean.

Fig. 26. (a) The cruise track (open circles connected by a solid line) overlayed on a map of mixed layer nitrate concentration ($\mu$M) extracted from the three eddy simulation on day 128. The year days of selected stations are indicated. The Small eddy is approximately in the center of the domain. Signatures of the Standard and Big eddies appear to the northwest and north of the Small eddy, respectively. The dashed line indicates a hypothetical cruise track (see text). (b) Mixed layer nitrate concentration ($\mu$M) observations (squares) and values extracted from the model along the cruise track (open circles connected by a solid line). The dashed line represents the concentration extracted from the model along the hypothetical track shown in panel (a).

*Acknowledgements*—D.J.M. and A.R.R. were supported by ONR N00014-84-C-0461, N00014-90-J-1593 and N00014-93-1-0577. D.J.M. was also supported by an Office of Naval Research Graduate Fellowship and a VCAR Postdoctoral Modeling Fellowship. J.J.M. was supported by NSF OCE88-17830. Many of the simulations in this study were carried out at the San Diego Supercomputer Center under grants HVD200 and HVD204. The helpful comments of four anonymous reviewers are greatly appreciated.

## REFERENCES

Angel M. and M. J. R. Fasham (1983) Eddies and biological processes. In: *Eddies in Marine Science*, A. Robinson, editor, Springer, Berlin, Chapter 22.

Bower A. (1991) A simple kinematic mechanism for mixing fluid parcels across a meandering jet. *Journal of Physical Oceanography*, **21**, 173–180.

Fasham M., H. W. Ducklow and S. M. McKelvie (1990) A nitrogen-based model of plankton dynamics in the oceanic mixed layer. *Journal of Marine Research*, **48**, 591–639.

Flierl G. and C. S. Davis (1993) Biological effects of Gulf Stream meandering. *Journal of Marine Research*, **51**, 529–560.

Franks P., J. S. Wroblewski and G. R. Flierl (1986) Prediction of phytoplankton growth in response to the frictional decay of a warm-core ring. *Journal of Geophysical Research*, **91**, 7603–7610.

Klein P. and B. L. Hua (1988) Mesoscale heterogeneity of the wind-driven mixed layer: influence of a quasigeostrophic flow. *Journal of Marine Research*, **46**, 495–525.

List R., editor (1951) *Smithsonian Meteorological Tables*. Smithsonian Institution, Washington.

Lochte K., H. W. Ducklow, M. J. R. Fasham and C. Stienen (1993) Plankton succession and carbon cycling at 47N, 20W during the JGOFS North Atlantic Bloom Experiment. *Deep-Sea Research II*, **40**, 91–114.

McGillicuddy D., J. J. McCarthy and A. R. Robinson (1995) Coupled physical and biological modeling of the spring bloom in the North Atlantic (I): model formulation and one dimensional bloom processes. *Deep-Sea Research I*, this issue.

McWilliams J. and G. R. Flierl (1979) On the evolution of isolated, nonlinear vortices. *Journal of Physical Oceanography*, **9**, 1155–1182.

Miller D. (1971) Global Atlas of Cloud Cover 1967–1970. Technical report, U.S. Department of Commerce and United States Air Force.

Nelson D., J. J. McCarthy, T. M. Joyce, and H. W. Ducklow (1989) Enhanced near-surface nutrient availability and new production resulting from the frictional decay of a Gulf Stream warm-core ring. *Deep-Sea Research*, **36**, 705–714.

Pollard R. and L. A. Regier (1992) Vorticity and vertical circulation at an ocean front. *Journal of Physical Oceanography*, **22**, 609–625.

Robinson A. (1993) Physical processes, field estimation and interdisciplinary ocean modeling. Reports in Meteorology and Oceanography. Harvard University, Cambridge, MA.

Robinson A. and L. J. Walstad (1987) The Harvard Open Ocean Model: calibration and application to dynamical process, forecasting, and data assimilation studies. *Applied Numerical Mathematics*, **3**(1-2), 89–131.

Robinson A., D. J. McGillicuddy, J. Calman, H. W. Ducklow, M. J. R. Fasham, F. E. Hoge, W. G. Leslie, J. J. McCarthy, S. Podewski, D. L. Porter, G. Saure and J. A. Yoder (1993) Mesoscale and upper ocean variabilities during the 1989 JGOFS bloom study. *Deep-Sea Research II*, **40**, 9–35.

Sarmiento J., R. D. Slater, M. J. R. Fasham, H. W. Ducklow, J. R. Toggweiler and G. T. Evans (1995) A seasonal three dimensional ecosystem model of nitrogen cycling in the North Atlantic euphotic zone. In press.

Strass V. (1992) Chlorophyll patchiness caused by mesoscale upwelling at fronts. *Deep-Sea Research*, **39**, 75–96.

Sverdrup H. (1953) On conditions for the vernal blooming of phytoplankton. *J. Cons. Explor. Mer.*, **18**, 287–295.

Woods J. (1988) Mesoscale upwelling and primary production. In: *Toward a theory on biological–physical interactions in the world ocean*, B. Rothschild, editor, Dordrecht.